INFORMATION TO USERS

This manuscript has been reproduced from the microfilm master. UMI films the text directly from the original or copy submitted. Thus, some thesis and dissertation copies are in typewriter face, while others may be from any type of computer printer.

The quality of this reproduction is dependent upon the quality of the copy submitted. Broken or indistinct print, colored or poor quality illustrations and photographs, print bleedthrough, substandard margins, and improper alignment can adversely affect reproduction.

In the unlikely event that the author did not send UMI a complete manuscript and there are missing pages, these will be noted. Also, if unauthorized copyright material had to be removed, a note will indicate the deletion.

Oversize materials (e.g., maps, drawings, charts) are reproduced by sectioning the original, beginning at the upper left-hand corner and continuing from left to right in equal sections with small overlaps. Each original is also photographed in one exposure and is included in reduced form at the back of the book.

Photographs included in the original manuscript have been reproduced xerographically in this copy. Higher quality 6" x 9" black and white photographic prints are available for any photographs or illustrations appearing in this copy for an additional charge. Contact UMI directly to order.

UMI

A Bell & Howell Information Company
300 North Zeeb Road, Ann Arbor MI 48106-1346 USA
313/761-4700 800/521-0600

Interaction of an Accelerated FRC
in a Transverse Magnetic Field

by

Peter A. Gurevich

A dissertation submitted in partial fulfillment
of the requirements for the degree of

Doctor of Philosophy

University of Washington

1998

Approved by 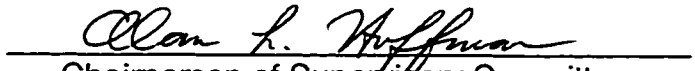
Chairperson of Supervisory Committee

Program Authorized
To Offer Degree Aeronautics and Astronautics

Date August 26, 1998

In presenting this dissertation in partial fulfillment of the requirements for the Doctoral degree at the University of Washington, I agree that the Library shall make its copies freely available for inspection. I further agree that extensive copying of this dissertation is allowable only for scholarly purposes, consistent with "fair use" as prescribed in the U.S. Copyright Law. Requests for copying or reproduction of this dissertation may be referred to University Microfilms, 1490 Eisenhower Place, P.O. Box 975, Ann Arbor, MI 48106, to whom this author has granted "the right to reproduce and sell (a) copies of the manuscript in microform and/or (b) printed copies of the manuscript made from microform."

Signature 

Date August 26, 1998

University of Washington

Abstract

Interaction of an Accelerated FRC in a Transverse Magnetic Field

by Peter A. Gurevich

Chairperson of the Supervisory Committee
Professor Alan H. Hoffman
Department of Aeronautics and Astronautics

The interaction and penetration of an accelerated FRC into a transverse magnetic field is studied for Tokamak refueling purposes. FRC penetration and interaction in the transverse magnetic field chamber is observed using visible light emission arrays, visible light imaging cameras, and several swept thermocouple probes. The FRC density and translation velocity are varied while monitoring the effect on penetration depth, deformation, tilt interaction and plasma deposition. The plasma penetration is observed using axial magnetic probes, while the plasma deformation is recorded with the visible light emission arrays and the swept thermocouple probes. 2 and 3-D magnetic field codes are used for field mapping for probe locations as well as translation and deformation simulations. Simple models are used to examine the effect that plasma deformation has on penetration as compared to the simple $\frac{1}{2}\rho U^2 = B^2/2\mu_0$ model.

TABLE OF CONTENTS

LIST OF FIGURES

Chapter 1

Purpose - Tokamak Refueling

The TRAP (Tokamak Refueling by Accelerated Plasmoids) facility was designed to develop a method of accelerating Field Reversed Configuration (FRC) plasmoids for Tokamak refueling purposes and to study their interaction with a simulated Tokamak transverse magnetic field. Presently, there is no working system that can be satisfactorily used for central refueling of a large, high temperature, high density, burning Tokamak plasma. The use of accelerated FRC's for this purpose is studied for their ability to meet the requirements for central refueling of large Tokamaks.

1.1 Present methods

The most commonly used conventional central refueling method for Tokamaks is based on the injection of small pellets of frozen hydrogen isotopes at high velocities. Currently, however, there exists no pellet injection system, nor is there one under developement, that can satisfy the immediate requirements for deep refueling of a large scale Tokamak experimental reactor. Additionally, it seem unlikely that any advanced pellet injection systems under study will be able to satisfy the requirements.

The primary reason for the expected inadequacies of projected injection systems comes from the difficulties in extrapolating the methods which are presently used on smaller scale devices to those methods to be used on larger scale Tokamak reactors. Presently, cylindrical pellets of up to 6 mm diameter (~ 10 mg) have been accelerated to 1.5 km/sec velocities, with their relatively large

mass allowing for increased penetration. However, the use of larger injection masses will increase the risk of a major plasma disruption.

The velocity requirement for pellet penetration to the core of a large, high temperature, high density fusion plasma is expected to exceed 100 km/sec[1]. Such velocity requirements are well outside the range of both present-day injection technologies (with maximum velocities of ~ 3 Km/sec) and advanced systems currently under study (i.e. rail guns or electron beam ablative accelerators, with maximum projected velocities of ~ 10 Km/sec). Additionally, because of the low inertial strength of frozen D-T ice, the pellet acceleration must be limited to a pressure equivalent of ~ 0.5 Mpa, or ~ 3 Mpa if bounded by a guide tube, otherwise pellet fracture will occur[1]. This will necessitate very long acceleration flight tubes for high velocity pellets (~3600 meters or 600 if bounded by a guide tube). Accelerated plasmoids, however, are extreamely robust bodies whose velocities are limited only by the energy delivery rates from the power supplies.

1.2 Current Plasma Research and new approach

The concept of using magnetized plasmoids (more commonly known as Compact toroids or CT's) for Tokamak fueling is not new. This application had been suggested as early as 1981 by Hammer and Hartman[2], and the concept has been further developed at Lawrence Livermore National Laboratory (LLNL) by conducting formation and acceleration experiments using a magnetized coaxial plasma gun to generate spheromak CT's.[3] Small scale spheromak injection experiments have also been conducted at Caltech on the ENCORE tokamak[4], and at Tokamak de Varennes. Although promising and scientifically interesting, these approaches encounter several limitations due to the type of CT used (spheromak), as well as the coaxial plasma gun source. These limitations

relate to the confinement geometry, plasma beta, and impurity content. The FRC type CT has advantages in each of these areas.

A more detailed description will follow, but briefly, an FRC is a magnetized plasmoid with a compact toroidal geometry where the induced toroidal diamagnetic currents provide a poloidal confinement field. The toroidal field inside an FRC is typically small, and the configuration has an intrinsically high beta. FRC's are robust plasmoids that have been efficiently compressed and translated.

Formation of an FRC in a Field Reversed Theta Pinch (FRTP) results in an elongated (prolate) CT with an elongation ratio, E, typically between 3 and 7. The constraints on axial equilibrium require that the average plasma beta of FRC's be high in order to balance the field line tension at the ends. For elongated FRC's it can be shown that the average beta $< \beta >$ is equal to $1\text{-}1/2\ x_s^2$, where $x_s = r_s/r_c$ is defined as the ratio of the FRC radius to the confinement coil radius. The average beta of an FRC is never less than 0.5 and is typically about 0.9 in most experiments. By contrast, spheromaks are CT's confined by both toroidal and poloidal fields of near equal magnitude. Their beta is usually between 0.01 and 0.1, and their elongation is typically oblate with $E \sim 0.7$.

Translation experiments on FRC's are conducted at the U. of Washington, and have been conducted at LANL[5] and at Osaka University in Japan[6] by either tapering the formation coil, or by using a small mirror coil at one end to initiate some axial motion. The early experiments were not aimed at maximizing the translation velocities, but rather at studying the lifetime of the translated FRC, and were carried out at a relatively low density compared to those desired for an ITER sized fueler. The typical 2-5 x 10^{15} cm^{-3} densities and 1-2 x10^5 m/sec translation velocities were increased in the TRAP experiment by increasing the FRTP fill pressure and field strength, and by utilizing separate compression and acceleration stages downstream from the formation chamber.

The research examined a practical technique for the central refueling of a large reactor grade Tokamak plasma by an FRC plasmoid driven by a coaxial accelerator. The approach is based upon the injection of dense, relatively cold magnetized plasmoids perpendicular to the toroidal field of a Tokamak. From the most simple momentum considerations, one can calculate the kinetic energy density required for plasmoid penetration into a Tokamak toroidal field.

$$\frac{1}{2}\rho \cdot v^2 = \frac{B_T^2}{2\mu_0} \qquad [1.1]$$

ρ and v are the plasmoid density and velocity and B_T is the Tokamak toroidal field. Higher temperature plasmoids are not an advantage here since, for a given density, higher fuel temperatures will require higher confinement fields during the FRC's formation and acceleration. Hotter plasmas will have lower densities and will require higher velocities and thus greater KE per fuel atom. The temperature need only be high enough to allow for preservation of the plasmoid configuration during the formation and acceleration.

From simple magnetics and energy considerations, it can be seen that for a given plasmoid magnetic field strength and temperature, an FRC will have a much higher density than a lower beta plasmoid such as a spheromak, and can thus penetrate a specified Tokamak field at a lower velocity and lower kinetic energy per particle. An FRC is a robust, long-lived magnetized plasmoid, and should prove to be an excellent Tokamak fueling source. The configuration lifetimes for translated FRC's have been observed to be up to several hundred μsec, which are many times the tens of μsec required to traverse the accelerator and transport sections and penetrate the Tokamak transverse field.

Chapter 2

Background

2.1 What is an FRC

An FRC is a prolate CT, which is normally confined inside a cylindrical flux conserver as shown in figure 1. The closed field line contours form surfaces of constant magnetic flux. Induced toroidal diamagnetic currents provide the poloidal confinement field. The radius to the field null is R, the separatrix radius and length are r_s and L_s, and the radius of the flux conserver is r_c. In an elongated FRC $r_s=\sqrt{2}\,R$. The toroidal field inside an FRC is typically small (usually assumed zero) which provides the configuration with an intrinsically high beta. Beta is defined as the ratio of plasma pressure P to magnetic field pressure $B^2/2\mu_o$. For an FRC the ratio $x_s \equiv r_s / r_c$ of the separatrix radius to the flux conserver coil radius is an important equilibrium quantity. x_s is determined almost entirely by the ratio of internal flux Φ_p to the external flux $\Phi_o = \pi r_c^2 B_o$. The length of the FRC, l_s, will vary dependent on the total thermal energy of the plasma. Thus, FRC's of a given flux will simply get longer as they become hotter, or gain more plasma. If they are magnetically compressed, by adding external flux, they will shrink, both radially and axially in a manner calculable from equilibrium considerations. FRC's are formed in a Field Reversed Theta Pinch (FRTP) which results in an elongated (prolate) CT with an elongation ratio, $E=l_s/2r_s$, typically between 3 and 7. The constraints on axial equilibrium require that the average plasma beta of FRC's be high in order to balance the field line tension at the ends.

What is a Field Reversed Configuration (FRC)

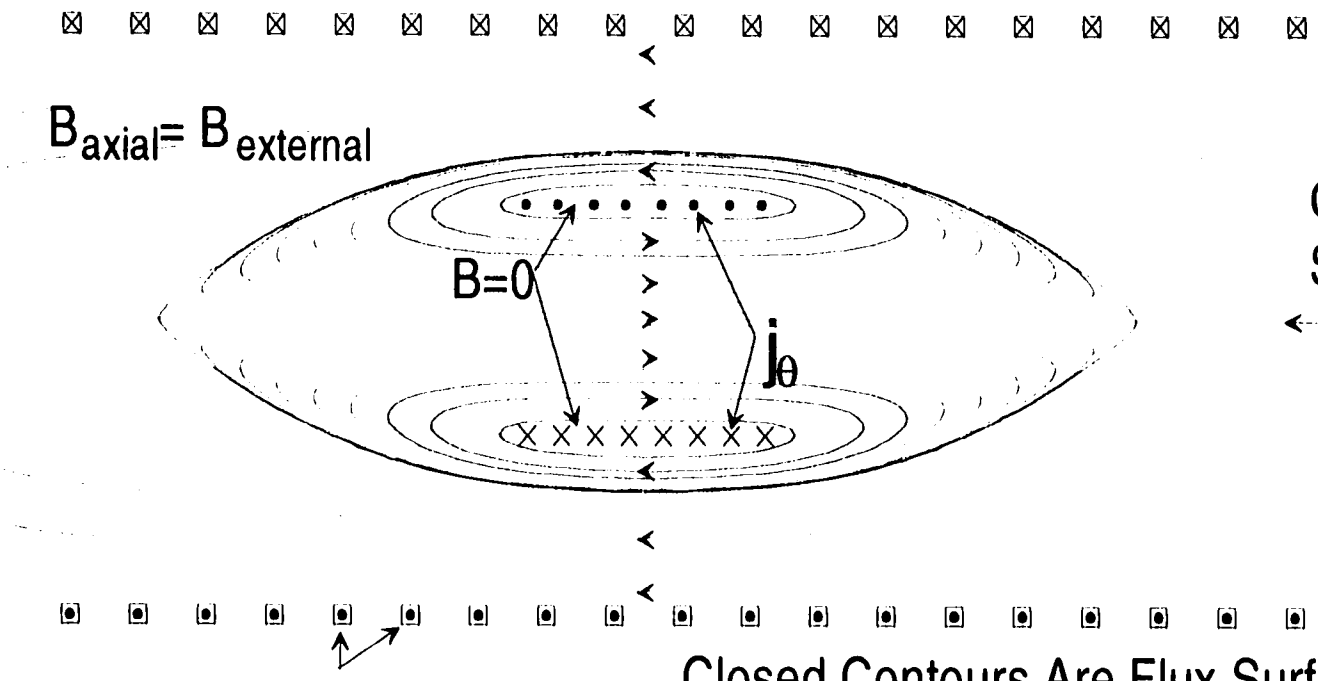

$$P_{interior(B=0)} \sim (B_{external})^2 / 2\mu_0 \qquad \beta \sim 1$$

Figure 1. What is an FRC

The average beta, <β>, inside the separatrix is determined from axial equilibrium considerations, for an elongated FRC, to be

$$\langle \beta \rangle = 1 - \frac{x_s^2}{2} \qquad [2.1]$$

The average beta of an FRC is never less than 0.5 and is typically about 0.9 in most experiments.

2.2 Conventional FRC formation

A detailed description of FRC formation can be found in the literature[7], but briefly Field Reversed Configurations are formed in field reversed theta pinches (FRTP) by a process illustrated in figure 2. Deuterium gas is preionized in the presence of a reverse bias field, and the axial magnetic field is then quickly reversed. A fraction of the reversed flux is trapped, which is called the lift off flux, $\Phi_{lo} = \pi r_w^2 B_{lo}$, where r_w is the radius of the FRTP formation chamber. The lift-off field B_{lo} is the value of the internal field remaining when the external field becomes of equal strength, and drives the plasma inward. Once the plasma is driven inward, external energy losses essentially cease, and any dissipated magnetic field energy is deposited in the plasma. Thus, Φ_{lo} (or B_{lo}) is an important quantity for determining the final FRC temperature. The reverse and forward flux are connected at the ends due to the initial field geometry (shown in figure 2), and the field line tension causes an axial contraction. The contraction continues until the average plasma beta becomes equal to $1 - x_s^2/2$.

Conventional FRC Startup

1) Start with uniform B in magnetized plasma.

2) Reverse B. Plasma driven up against wall. Induced currents flow due to gradient in B.

3) Radial Compression. Plasma pushed off wall.

4) Axial compression to equilibrium.

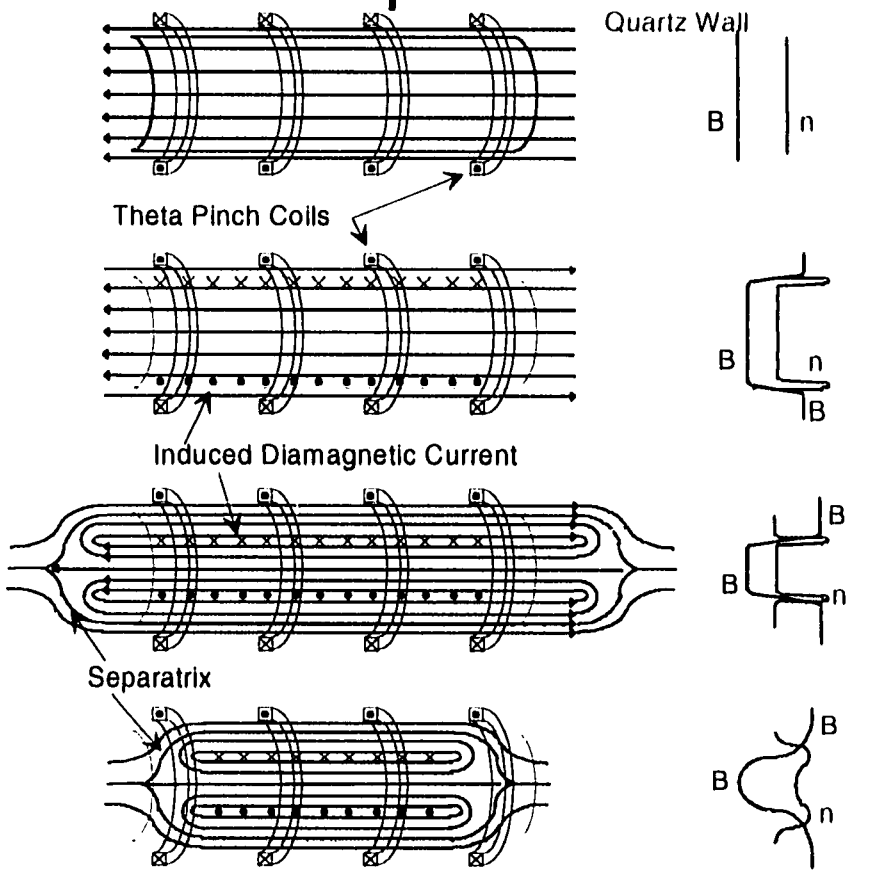

Generate a Field Gradient ΔB to Induce a Diamagnetic Current I_θ .

Figure 2. Conventional FRC Startup

The plasma is heated by both ohmic dissipation and the axial contraction. Simple energy conservation arguments show that the energy added to the FRC is related to the energy stored in the compressed lift-off flux by the relationship[7]

$$T_e + T_i = 600 f_p B_{lo}^{6/5}(KG) B_e^{4/5}(KG) / p_o(mTorr) \ \ eV \qquad [2.2]$$

where f_p is a factor which varies only slightly from unity, depending on how much of the lift-off flux is dissipated. The heating is governed by energy conservation, so the final temperature is not strongly dependent on the flux loss. Lesser amounts of ohmic dissipation and flux loss will result in a stronger axial contraction and cause non-adiabatic axial implosion heating.

The final plasma temperature is inversely proportional to the deuterium fill pressure, since the available energy is distributed among more particles. Full gas sweep up in the FRC is assumed, which agrees with experimental observations. Conventional FRC reactor development would tend toward the use of low density, high temperature plasmas. For refueling purposes, a high density, low temperature plasmas is desired. Use of FRC plasmoids as a fueler will be limited only by the ability to form FRC's at high densities and by their resultant lifetimes.

2.3 Velocity requirements

Conventionally, an accelerated CT is analyzed as a solid incompressible conductor, encountering a step function transverse magnetic field. The CT experiences a resisting pressure on the order of $B_T^2/2\mu_o$, and would need a kinetic energy density of $1/2\ \rho v^2$ to overcome this pressure. This is the origin of equation [1.1]. For a solid conductor of finite length, once it fully penetrates, it will experience the same pressure on its rear, and will keep moving at a constant

velocity unless the field increases further. This is different from the standard considerations used in the design of armor piercing projectiles, since there is no equivalent pressure on the rear of the projectile, and the penetrability is related to the total projectile length.

For a compressible, conducting fluid projectile, the situation is more complicated. Approximately, the fluid kinetic energy density must be sufficient to generate field pressures equal to the Tokamak magnetic field pressure. The situation is even more complex when the fluid contains its own magnetic field but, at least for an FRC, this internal field component is weak.

The effects of plasma compression will be examined in more detail in a later section; but from these simple momentum considerations it can be shown that neglecting compression, the requirement for a magnetized plasma to penetrate a given perpendicular field strength is that the kinetic energy density of the plasma exceed the magnetic pressure of the perpendicular field (equation [1.1]). This can be expressed as

$$v(m/\sec) = \frac{2.2\times10^5}{\sqrt{A_i}} \frac{B_T(T)}{n^{1/2}(10^{16}cm^{-3})} \qquad [2.3]$$

with A_i being the atomic mass number (2.0 for D). This is just the Alfven velocity of the FRC related to the transverse Tokamak field. High plasmoid mass densities are desirable to minimize the injection velocity required to penetrate a given Tokamak toroidal field. For a given total mass, this also minimizes the required acceleration energy. Densities of 10^{16} cm^{-3} are easily achievable for TRAP FRC's formed at high fill pressures and high formation fields. At such densities, a velocity of about 1.50 x 10^5 m/sec would be required for penetration through a target 1 Tesla transverse field. This transverse field was simulated in the experiment which will be described in chapter 4. At our masses of about 0.6 mg (~2x10^{20} ions), the FRC has a volume of about 0.02 m^3 and a kinetic energy

of about 6.75 KJ. By compressing the plasma to a 4 x 10^{16} cm^{-3} density, the required velocity could be lowered to 0.75 x 10^5 m/sec, and the kinetic energy to 1.68 KJ.

2.4 Acceleration Mechanism

An FRC can be accelerated by increasing the magnetic field behind it, and decreasing the field ahead. The accelerating force will be $F = f(\pi r_s^2)(B^2/2\mu_o)$ where f is a factor of order unity representing how the axial magnetic field difference produces an axial force. The energy imparted to the FRC in a distance d is then

$$\Delta(KE) = Fd = f(\pi r_s^2)\frac{B^2}{2\mu_0}d. \qquad [2.4]$$

For the case where the FRC is translated from one flux conserver to another, the factor f can be derived from simple energy considerations.

It can be shown from equilibrium considerations that the total energy of an FRC and the magnetic field inside a flux conserver is equal to

$$E_{tot} = \frac{5}{2}\langle\beta\rangle\frac{B_e^2}{2\mu_o}V_s + \frac{B_o^2}{2\mu_o}V_c = \frac{5}{2}NkT_t + \frac{B_o^2}{2\mu_o}V_c \qquad [2.5]$$

where $N = \langle n\rangle V_s$ is the total number of ions, T_t is the sum of the electron and Ion temperatures, $V_s = \pi r_s^2 l_s$ is the FRC volume, $V_c = \pi r_c^2 l_c$ is the flux conserver volume, B_o is the vacuum field, and $B_e = B_o/(1-x_s^2)$ is the field adjacent to the FRC. Assuming that flux is conserved when the FRC is ejected from one flux conserver into another, the gain in Kinetic energy will be

$$\Delta(KE) = \frac{5}{2}Nk\Delta T_t. \qquad [2.6]$$

The principal is similar to coaxial accelerators, except that the energy gain for a gas or plasma is higher due to the (3/2)NkT$_t$ thermal energy content. Using $\langle n \rangle kT_t = \langle \beta \rangle B_e^2/2\mu_o$, the change in kinetic energy can be written as[7]

$$\Delta(KE) = \frac{5}{2}\left(\frac{\Delta T_t}{T_t}\right)\langle\beta\rangle(\pi r_s^2)\left(\frac{B_e^2}{2\mu_0}\right)l_s \qquad [2.7]$$

The factor f in equation [2.4] can be written as

$$f = \frac{5}{2}\left(\frac{\Delta T_t}{T_t}\right)\langle\beta\rangle\frac{l_s}{l_c}, \qquad [2.8]$$

where d = l_c is the length of the flux conserver. For typical expansion into a magnetic field of half the strength of the initial field, when the expansion is assumed to be adiabatic ($T \sim B^{4/5}$), the ($\Delta T_t/T_t$) will be about 0.43.

The acceleration section uses a series of initially low field flux conserving coils, with the field in each coil increased after the FRC enters it, in order to give the FRC a 'kick' as the FRC exits to the next coil. For this simple ejection process from a flux conserver, the $\Delta(KE) = 1/2\,\rho V_s \Delta v_e^2$ and Eq. [2.7] can be written as

$$\frac{1}{2}\rho \cdot \Delta v_e^2 = \frac{5}{2}\left(\frac{\Delta T_t}{T_t}\right)\langle\beta\rangle\frac{B_e^2}{2\mu_o} \qquad [2.9]$$

where ρ is the density before the FRC has expanded into the new flux conserver.

This is similar to equation [2.2] and can be written in the same units as

$$v_e(m/\sec) = \sqrt{\frac{5}{2}\left(\frac{\Delta T_t}{T_t}\right)\langle\beta\rangle}\,\frac{2.2\times10^5}{\sqrt{A_i}}\,\frac{B_e(T)}{n^{1/2}(10^{16}cm^{-3})}. \qquad [2.10]$$

FRC's have been ejected from the experiment's field reversed theta pinch formation chamber by using a stronger magnetic mirror at one end, and the measured velocities agree quite closely with equation [2.10].

FRC's are typically formed at fields of around 1 Tesla. The plasma temperature is related to the average density through the pressure balance relationship

$$T_t(keV) = 0.25\langle\beta\rangle B^2(T)/n\left(10^{16}cm^{-3}\right) \qquad [2.11]$$

The total temperature must be at least 100 eV for reasonable FRC lifetimes, so, the maximum density in the formation chamber is about 2 x 10^{16} cm^{-3} (for $<\beta>$ = 0.8). Ejection from the formation chamber without additional acceleration, would only allow penetration of a 1 Tesla transverse field. Higher non assisted injection velocities could be achieved by raising the formation field, but this process is inefficient. The FRC would shrink in size while most of the input compression energy would be deposited in the vacuum field. The multi-stage accelerator, utilizing smaller compressions in each stage, is more efficient.

The above coaxial accelerator analysis is highly idealized since it assumes that the flux inside each flux conserver is instantaneously increased while the FRC resides fully in the flux conserver, and the FRC will instantaneously reach a new equilibrium. This becomes unrealistic as the FRC speed increases, and necessitates the use of numerical calculations to accurately calculate f. However, the coaxial accelerator analysis is useful in examining the energetics of the system and is extremely accurate in describing the initial transit from the reversed field theta pinch formation chamber into a lower field translation region. Since the FRC is initially traveling slowly, there is sufficient time to bring each coil's flux to a constant value, and for the FRC to reach a new equilibrium.

2.5 FRC Acceleration

The TRAP facility employed a deuterium puff fill formation chamber with fill pressures of about 20 mTorr (N~$2x10^{20}$, M~0.6 mg). Operation at ~ 0.9 T formation fields produced FRCs with n~10^{16} cm^{-3} and T_t~100 eV. Analysis of the typical experimental operating conditions, with the initial accelerator and transport sections bias fields of 0.3 - 0.4 T, is shown in Table 2.1. B_o is the magnetic field that would be present without the presence of the FRC, and $B_e = B_o/(1-x_s^2)$ is the field confining the FRC. The first line gives the formation conditions, the next two lines give the initial and final conditions in the acceleration section, and the final line gives the condition in the transport section. $\Delta(v^2)$ is given by

$$\Delta(v^2)\left(m^2/s^2\right) = 2\Delta(KE)/Nm = 5(k/m)\Delta T_i = 2.4x10^8 \Delta T_i(eV) \qquad [2.11]$$

Table 2.1

FRC Conditions During Acceleration Process

Section	**B_o(kG)**	**B_e(kG)**	**r_s(cm)**	**n(10^{16} / cm^3)**	**l_s (cm)**	**T_t(eV)**	**Δv^2 $(cm/\mu s)^2$**
Formation	9.0	10.3	8.1	1.74	50	142	
							127
Accelerators	2.9	4.6	8.9	0.48	150	89	
	6.1	7.5	6.3	0.90	160	140	
							72
Transport	3.7	5.4	8.9	0.56	130	110	

The accelerator section consists of four separate 0.5 m long sections. Since the FRC length is over 100 cm, a simple estimate of the final velocity is made based on two 100 cm stages of acceleration as shown in Table 2.1. Each stage has vacuum field increasing from 2.9 kG to 6.1 kG, and B_e increasing from 4.6 kG to 7.5 kG. The calculated increase in v^2 (using Table 2.1) is therefore 127+2x(72) = 271 $cm^2/\mu s^2$. The final calculated velocity is 16.5 cm/μs, which matches closely the FRC's measured velocity using the diamagnetic loop array diagnostic.

Chapter 3

FRC Penetration and interaction theory

3.1 Analysis and Modeling

Upon encountering the transverse magnetic field, as opposed to the axial accelerator field, the FRC will tend to expand along the field lines and be compressed perpendicular to them. The expansion in the plane of the transverse field was modeled by assuming a completely flux excluding FRC. The FRC cross section was assumed to be elliptical (e = b/a), even though this did not result in a constant pressure on the FRC surface. This elliptical assumption allowed analytic calculations to be made of the resultant distorted transverse magnetic field, along with determinations of the average horizontal and vertical forces exerted on the FRC, and the increase in transverse field magnetic energy due to the FRC penetration. The model is completely two-dimensional and says nothing about the FRC axial compression or total cross sectional area, but for simple volume dependant energetics, the details of the compression, other than the ellipsivity e, do not affect the penetration. When combined with an axial compression model, the two dimensional flux excluding elliptical cross section model allows the FRC shape to be derived. Basic to the model is the assumption that the internal magnetic fields will adjust to provide full equilibrium, or that small departures from equilibrium will not result in significant differences from an elliptical shape in the short time it takes the FRC to penetrate the transverse field. The calculated average horizontal forces provided by the model can be used to estimate the time dependence of the overall transverse distortion.

3.2 FRC Tilt rates

The transverse field will exert a tilting force on a compact toroid which will try to align the internal magnetic field of the CT with the transverse field. This will result in tearing and reconnection of the external field lines of the CT with the transverse field and destruction of the CT. This process is necessary to disperse the CT plasma once the CT has penetrated to the desired location. Premature tilting and plasma deposition has been thought to be a possible limiting feature of CT fueling. The process is extremely complex as the tilting force will depend on the penetration of the transverse field into the CT, but we will calculate the tilting time based on full transverse field penetration. The tilting time of a CT will be shown to be

$$\tau_{tilt} \approx \sqrt{2}E\frac{r_s}{v_A} \qquad [3.1]$$

where $v_A = B_T/\sqrt{\mu_o \rho}$ is the Alfven velocity of the CT plasma in the transverse field. Full transverse field penetration is, of course, the complete opposite assumption of the flux excluding penetration model, but it follows previous analysis and provides a 'worst case' scenario for limiting penetration. For a rigid body FRC the large elongation E of an FRC provides for much longer tilting times than for an oblate (E<1) spheromak, and there is evidence that even aligned FRCs take several tens of μsec to be destroyed. Thus, FRC fueling may have the opposite problem from incomplete penetration, that of reflection before the fuel can be deposited in the center of the Tokamak.

Assuming that the FRC has a reasonable conductivity, and sufficient kinetic energy, it will push the Tokamak field aside. Longitudinal loop currents will be induced on the surface of the FRC in order to exclude the Tokamak field. The interaction of the diffused transverse field with the FRC toroidal currents, and the FRC internal field with the induced longitudinal loop currents, produce

the **JxB** forces that cause the FRC to tilt and align itself with the transverse field, causing the outer flux surfaces of the FRC to tear and reconnect with the transverse field.

At a 100 eV electron temperature, the classical plasma resistivity is about 10^{-4} ohm-cm, and the classical field diffusion coefficient is 0.08 $mm^2/\mu sec$. Even if the anomalous resistivity is 100 times the above value, as has been measured in small FRCs, the field diffusion coefficient would still only be about 0.1 $cm^2/\mu sec$. In the few μsec it takes the FRC to transverse the Tokamak minor radius, the current sheath should remain very thin.

The tilting time for the FRC in the toroidal Tokamak field is most simply analyzed by computations based on a rigid body tilt. For our prolate FRC the transport tube may prevent rigid tilting as it does in experiments without transverse fields. However, for the simple analysis that follows, the external geometry considerations will be ignored. The FRC will be assumed to be a circular cross-sectional cylinder of some given length l_s, radius r_s and density ρ. Deformation of the plasma cross-section to a more elliptical nature may slightly alter the approximate tilt time, but for the simple analysis that follows, this possible complication is neglected. The Tokamak plasma should have very little effect on the FRC interaction due to the low Tokamak beta, so the arguments should be the same whether or not the FRC is in the fringing field, or in the actual Tokamak discharge.

The tilting torque **T** an FRC will experience when it encounters a transverse field $\mathbf{B_T}$, is equal to $\mathbf{m} \times \mathbf{B_T}$ where **m** is the magnetic moment of the FRC. For simplicity **m** is assumed to be equal in magnitude to $\pi R^2 I_\theta$, where I_θ is the total FRC toroidal current and R is the FRC null field radius. I_θ is related to the FRC poloidal field B_p by the relationship

$$I_\theta = \frac{l_s B_p}{\mu_o} = \frac{2B_p}{\mu_o} E r_s \qquad [3.2]$$

Recalling that $r_s = \sqrt{2}R$ the torque exerted by a transverse field B_T on an FRC can be written as

$$T = \pi r_s^3 E \frac{B_p B_T}{\mu_o} = \pi r_s^3 E \sqrt{1-\beta}\, \frac{B_T^2}{\mu_o}. \qquad [3.3]$$

where the FRC internal pressure is assumed to be equal to the external field pressure and $B_p = \sqrt{1-\beta}\ B_T$. The moment of inertia of an FRC is

$$I_m = \frac{1}{5} M \left\{ r_s^2 + \left(l_s / 2 \right)^2 \right\} = \frac{1}{5} M r_s^2 \left(1 + E^2\right) \qquad [3.4]$$

where $M = 4/3\pi E r_s^3 \rho$ is the total FRC mass of an ellipsoidal FRC of constant density. A characteristic tilt time can be expressed as $\tau_{tilt} = \sqrt{\pi * I_m / T}$. Which then can be rewritten as

$$\tau_{tilt} = \left[\frac{\left(1+E^2\right)\mu_o M}{5 E r_s \sqrt{1-\beta}} \right]^{1/2} \frac{1}{B_T} = \left[\frac{4\pi\left(1+E^2\right)}{15\sqrt{1-\beta}} \right]^{1/2} \frac{r_s}{v_A}. \qquad [3.5]$$

For plasmas at densities of about 10^{16} cm^{-3} in a 1 Tesla field, the Alfven speed is about 1.38 x 10^5 m/sec, and FRC's with radial dimensions of tens of cm will tend to tilt rapidly unless E or β is large. Fortunately, both these parameters are substantially larger in an FRC than in other CTs such as Spheromaks, making it ideal for deep fueling of Tokamak reactors. For high E and the typical high

values of beta ($\beta > 0.8$) in an FRC the tilt time can be simplified and approximated by equation [3.1].

We can now compute a simple theoretical tilt time of a typical accelerated FRC used in the TRAP experiment. Using the values of the FRC example given in Table 2.1, and assuming no change in the interaction chamber, the separatrix radius is 8.9 cm and the elongation is E = 7.3. The calculated tilt time for this FRC in a 1T perpendicular field (Based on equation [3.1]) is 6.6 μsec.

3.3 FRC Deformation

For a long thin plasmoid, such as an FRC, the shape of the plasmoid in the transverse field can be approximated as a long circular cross-sectional cylinder, and the transverse field perturbations can be analyzed using a 2-D fluid model as shown in figure 3.

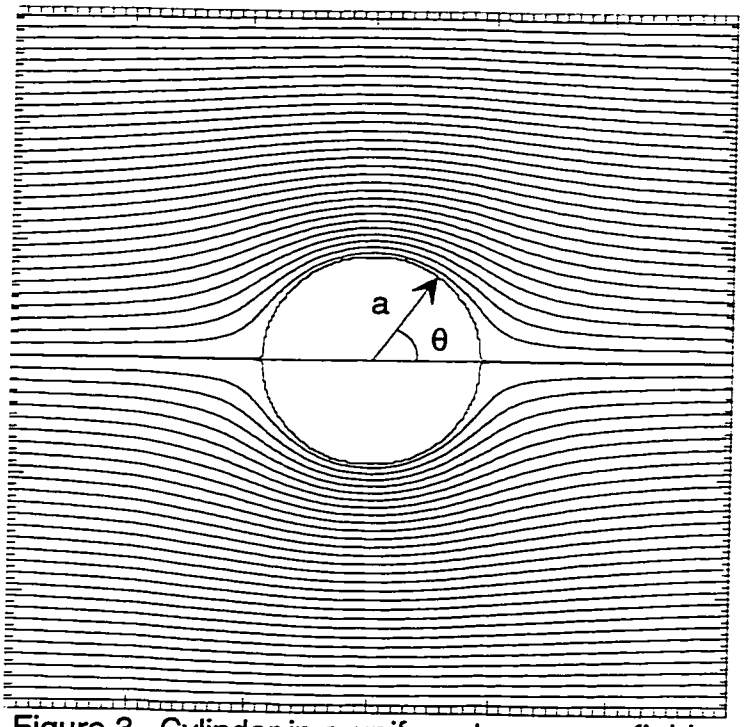

Figure 3. Cylinder in a uniform transverse field.

However, as previously mentioned the FRC cross-section is expected to deform as it expands parallel and is compressed perpendicular to the transverse field. A cylinder with an elliptical cross-section is a more accurate description of the penetrating plasmoid. In order to estimate the range of ellipsivity of the deformed plasma and the time-scale of plasma deformation a Lagrangian analysis of the plasma energies and magnetic field energies was conducted.

The Lagrangian analysis utilized a stationary, constant length uniform density cylindrical plasma with varying minor cross sectional area, while the cross sectional shape was constrained to be elliptical in nature. The plasma cylinder was instantaneously exposed to a spatially uniform transverse field. Conservation of mass per unit length was used to relate the cross sectional area to the density. Expansion or compression of the plasma was assumed to be isentropic, and the isentropic relationship was used to relate the plasma density to the pressure.

The kinetic energy of the system is simply the kinetic energy of the plasma associated with any radial expansion or compression of the cross section. The potential energy of the system must include the internal thermal energy of the plasma, the internal magnetic energy of the plasma, and the magnetic energy in the external field. Based on the results shown in section 3.4, the total excess transverse field energy per unit length produced by insertion of the FRC is given by $\varepsilon_c = \frac{B_t^2}{2\mu_0} A \frac{1}{e^{0.1}} \left(1 + \frac{1}{\sqrt{e}}\right)$, where e = b/a is the ellipsivity of the plasma cross section (shown in figure 5) with minor radius a and major radius b. The internal plasma energy per unit length is just $\varepsilon_{i.p.} = \frac{3}{2} PA$ and the internal FRC magnetic energy per unit length can be given by $\varepsilon_{i.m.} = \frac{1-\beta_0}{\beta_0} P_0 A_0 \frac{A_0}{A}$. Thus we can write for Lagrangian analysis purposes

$$V = \frac{3}{2}PA + \frac{1-\beta_0}{\beta_0}P_0A_0\frac{A_0}{A} + \frac{B_t^2}{2\mu_0}A\frac{1}{e^{0.1}}\left(1+\frac{1}{\sqrt{e}}\right) \qquad [3.6]$$

The kinetic energy per unit length associated with radial expansion is given by

$$T = \iint \frac{1}{2}\rho v_r^2 dxdy = \frac{1}{8}\rho_0 A_0\left(\dot{a}^2 + \dot{b}^2\right) \qquad [3.7]$$

With the energy terms of the system defined, the analysis continued using the equations derived in terms of the minor radius a and the major radius b of the plasma. The Euler-Lagrange equations for L=T-V in terms of a and b are:

$$\frac{d}{dt}\left(\frac{\partial L}{\partial \dot{a}}\right) - \frac{\partial L}{\partial a} = 0 \qquad \frac{d}{dt}\left(\frac{\partial L}{\partial \dot{b}}\right) - \frac{\partial L}{\partial b} = 0 \qquad [3.8]$$

and yield

$$\frac{1}{4}\rho_0 A_0 \ddot{a} = -\frac{\partial V}{\partial a} \qquad \frac{1}{4}\rho_0 A_0 \ddot{b} = -\frac{\partial V}{\partial b} \qquad [3.9]$$

The continuity and isentropic relations $A = \pi(a^2+b^2)$, $n \propto 1/A$, $P \propto (1/A)^{5/3}$ are used and non-dimensional variables are defined as follows.

$$x = \frac{a}{a_0}, \qquad w = \frac{\dot{a}}{a_0}, \qquad y = \frac{b}{b_0}, \qquad z = \frac{\dot{b}}{b_0}$$

(Expansion perpendicular to external field) *(Expansion Parallel to external field)*

The substitutions yield:

$$\dot{x} = w \qquad [3.10a\text{-}d]$$
$$\dot{y} = z$$

$$\dot{w} = \frac{-4}{a_0^2}\frac{P_0}{\rho_0}\left\{\frac{-1}{x}\left(\frac{1}{xy}\right)^{\gamma-1} + \frac{\frac{B_0^2}{2\mu_0}}{P_0}(xy)\left(\frac{x}{y}\right)^{1/10}\left[\frac{1.1}{x}\left(1+\left(\frac{x}{y}\right)^{1/2}\right)+\frac{1}{2}\frac{1}{x}\left(\frac{x}{y}\right)^{1/2}\right]-\frac{\frac{1}{2}x_{s_0}^2}{\beta_0}\frac{1}{xy}\frac{1}{x}\right\}$$

$$\dot{z} = \frac{-4}{b_0^2}\frac{P_0}{\rho_0}\left\{\frac{-1}{y}\left(\frac{1}{xy}\right)^{\gamma-1} + \frac{\frac{B_0^2}{2\mu_0}}{P_0}(xy)\left(\frac{x}{y}\right)^{1/10}\left[\frac{0.9}{y}\left(1+\left(\frac{x}{y}\right)^{1/2}\right)-\frac{1}{2}\frac{1}{y}\left(\frac{x}{y}\right)^{1/2}\right]-\frac{\frac{1}{2}x_{s_0}^2}{\beta_0}\frac{1}{xy}\frac{1}{y}\right\}$$

These equations required integration, and a numerical solution was developed using a fourth order Runge-Kutta solution for the system of equations. The Runge-Kutta solution used typical experimental conditions in an attempt to crudely simulate the deformation as it might occur in the experiment. The cylindrical plasma used had a radius of 7.2 cm and a temperature of T_t = 90 eV. The uniform transverse field had a magnitude of 0.435 Tesla, which corresponded to the magnitude of the field in the center of the interaction chamber during a shot with the interaction field energized to 7.5 kV. The results are shown in figure 4.

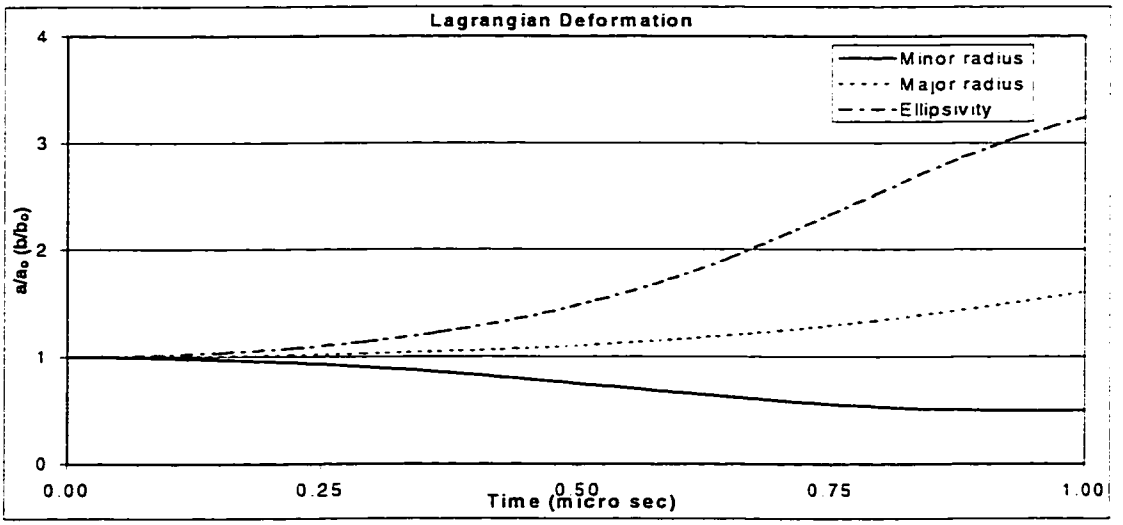

Figure 4. Lagrangian Analysis of plasma deformation

The cylindrical plasma can be seen to rapidly deform out of round into the expected elliptical shape. The time scale of this deformation can be seen to be on the order of ~ 1 μsec, indicating that the plasma should have sufficient time to experience severe deformation in the transverse field chamber during its 5 – 10 μsec transit time.

3.4 Transverse field perturbations

For the 2-D perturbation model we will assume a flux excluding superconducting cylindrical FRC of undetermined length, with a uniform elliptical cross section in a channel that conserves the transverse flux through the region. The FRC internal pressure is balanced by the average B_θ^2 magnetic field pressure at the surface of the cylinder. This model of the perturbed magnetic field is equivalent to the 2-D fluid flow pattern around an infinite elliptical cylinder in uniform rectilinear flow, as shown below in Figure 2, and is similar to the 3-D model used by Parks[8] for a spherical compact toroid in a transverse field. The magnetic field solution can easily be modified to take into account the magnetic flux conserving nature of a channel. Extrapolation of this method to the more complex geometry of the Tokamak chamber, however, would be more difficult.

The fluid stream function for an infinite elliptical cylinder in uniform rectilinear flow, as shown in figure 5, is[9]

$$\psi = V_\infty y - \frac{m}{2\pi}\tan^{-1}\left(\frac{2x_0 y}{x^2 + y^2 + x_0^2}\right) \qquad [3.11]$$

Where m is the strength and x_0 is one half the separation of the souce/sink doublet used to create the field pattern. X and Y components of the magnetic

field are $B_x = \frac{\partial \psi}{\partial y}$ and $B_y = -\frac{\partial \psi}{\partial x}$. The source/sink strength and location can be varied to produce a ψ=0 surface of any desired size given by the minor radius a and the ellipsivity e=b/a.

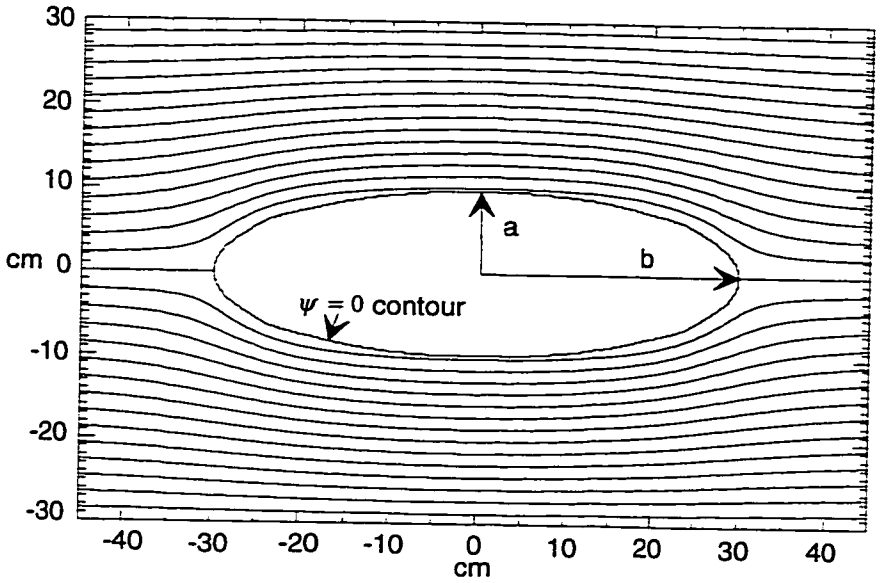

Figure 5. Elliptical cylinder in uniform rectilinear flow

Outside the ψ=0 surface the solution satisfies the fluid (and therefore the equivalent magnetic field) requirements that $\nabla \bullet \mathbf{B}=0$ and $\nabla \times \mathbf{B}=0$ and the boundary conditions at the ψ=0 surface. However, the solution is only valid when there is no constraining wall (flux conserving chamber) or the constraining wall is very far away. An exact solution to the magnetic field pattern in a flux conserving chamber is numerically modeled using a method of successive reflections of the solution in uniform rectilinear flow.

In the numerical model the penetrating FRC is assumed to be a $\beta \sim 1$ plasma with a pressure $P=P(a,e,B_t)$ equal to the average value of the external

field pressure at the Ψ=0 surface $P = \frac{\langle B_{\psi=0}^2 \rangle}{2\mu_o}$ Numerical calculations yield the following result.

$$P \cong \frac{B_t^2}{2\mu_o}\left(\frac{1+\frac{1}{\sqrt{e}}}{1-\frac{3}{4}\sqrt{e}\frac{a^2}{R_w^2}}\right) \qquad [3.12]$$

B_t is the original transverse field magnitude and R_w is the half height of the flux conserving wall. When a/R_w is small this reduces to

$$P \cong \frac{B_t^2}{2\mu_o}\left(1+\frac{1}{\sqrt{e}}\right) \qquad [3.13\ a]$$

and the forces per unit length exerted on the FRC were found to be.

$$F_x'/2a \cong \left(1+\frac{1}{3e^{3/4}}\right)\frac{B_t^2}{2\mu_0} \qquad F_y'/2b \cong \left(1+\frac{5}{3e^{3/4}}\right)\frac{B_t^2}{2\mu_0} \qquad [3.13\ b,c]$$

These forces become comparable at e~4. The FRC can reasonably be expected to deform to a cross-section of approximately this ellipsivity and the lagrangian analysis shows that this should occur quickly.

For a given ellipsivity, the compressed magnetic field energy ε_c in the transverse field was found to be simply a function of the plasma volume and the initial transverse field strength, with initial numerical calculations yielding

$$\varepsilon_c \cong \left(1+\frac{1}{\sqrt{e}}\right)\frac{B_t^2}{2\mu_o}\frac{1}{e^{0.1}}\pi abL_2$$

The $1/e^{0.1}$ term in the initial numerical calculation for the compressed magnetic field energy ε_c was a result of the limited range of the computational grid. When a larger computational grid was used the results yielded

$$\varepsilon_c \equiv \left(1+\frac{1}{\sqrt{e}}\right)\frac{B_t^2}{2\mu_o}\pi abL_2 \qquad [3.14]$$

The numeric field model results provide the necessary components to obtain a solution to the following FRC penetration model.

3.5 FRC Penetration Energetics

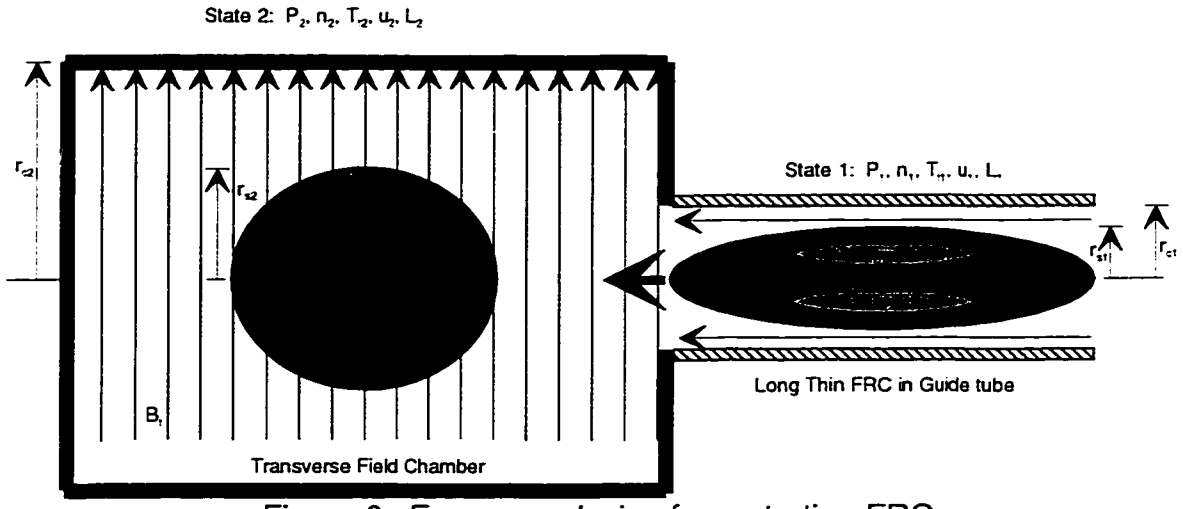

Figure 6. Energy analysis of penetrating FRC

The penetration analysis starts with the volume integrated energy equation for the volumes shown above.

$$N\left[\frac{5}{2}kT_{t1}+m_i\frac{u_1^2}{2}\right]=N\left[\frac{3}{2}kT_{t2}+m_i\frac{u_2^2}{2}\right]+\varepsilon_c \qquad [3.15]$$

This Equation assumes $<\beta_2>$ ~ 1, which will be accommodated by later using $P_2 = n_2kT_2$, where n_1 and n_2 are average values inside the FRC separatrix. The expression in equation [3.14] for the compressed magnetic field energy was then used to produce:

$$\left[m\frac{u_1^2}{2}-m\frac{u_2^2}{2}\right]=\left[\frac{3}{2}kT_{t2}-\frac{5}{2}kT_{t1}\right]+\left(1+\frac{1}{\sqrt{e}}\right)\frac{B_t^2}{2\mu_o}\frac{\pi abL_2}{N} \qquad [3.16]$$

Calling $n_2 = N/\pi abL_2$ and using the equation of state

$$\frac{1}{2}m\left(u_1^2 - u_2^2\right) = \frac{3}{2}\frac{p_2}{n_2} + \left(1+\frac{1}{\sqrt{e}}\right)\frac{B_t^2}{2\mu_o}\frac{1}{n_2} - \frac{5}{2}\frac{p_2}{n_2}\frac{T_{t1}}{T_{t2}} \qquad [3.17]$$

Using equation [3.13] for P_2

$$u_2^2 = u_1^2 - 2 * \frac{1}{mn_2}\frac{5}{2}\left(1-\frac{T_{t1}}{T_{t2}}\right)\left(1+\frac{1}{\sqrt{e}}\right)\frac{B_t^2}{2\mu_o} \qquad [3.18]$$

For $u_2=0$

$$\frac{1}{2}mn_1u_1^2 = \frac{n_1}{n_2}\frac{5}{2}\left(1-\frac{T_{t1}}{T_{t2}}\right)\left(1+\frac{1}{\sqrt{e}}\right)\frac{B_t^2}{2\mu_o} \qquad [3.19]$$

Clearly, high values of n_2 (ρ_2) are desirable for penetration. The final value for n_2 depends on the relationship between $\frac{n_2}{n_1}$ and $\frac{p_2}{p_1}$, where

$$\frac{p_2}{p_1} = \left(1+\frac{1}{\sqrt{e}}\right)\frac{B_t^2}{B_g^2} \qquad [3.20]$$

is determined by equation [3.13a] for a $\beta=1$ plasma. The B_g used in the energetics analysis is the confining field in the transport/guide section and is equivalent to what was previously called B_e. For a completely isentropic transition from state 1 to 2, again using the $<\beta> \sim 1$ assumption

$$\frac{n_2}{n_1} = \left(\frac{p_2}{p_1}\right)^{3/5} \quad \text{and} \quad \frac{T_2}{T_1} = \left(\frac{p_2}{p_1}\right)^{2/5}. \qquad [3.21]$$

An approximation of the effects of a non-isentropic compression from state 1 to 2 can be made by assuming a single shock compression of a $\gamma = 5/3$ gas to the pressure ratio of $p_2/p_1 = (1+1/\sqrt{E})B_T^2/B_e^2$. The jump conditions are then

$$\frac{n_2}{n_1}=\frac{4\left[1+\frac{4}{5}\left(\frac{p_2}{p_1}-1\right)\right]}{\left[1+\frac{4}{5}\left(\frac{p_2}{p_1}-1\right)\right]+3} \quad \text{and} \quad \frac{T_2}{T_1}=\frac{p_2}{p_1}\frac{n_1}{n_2} \qquad [3.22]$$

Using these relationships, the model is only dependant on the ellipsivity and overall compression of the FRC and not on the relation between axial and radial compression.

Equation [1.1] with K=1 has been used to evaluate the kinetic energy density required for a compact toroid to penetrate a transverse field, and it was with this form in mind that equation [3.19] was written. One does note that, regardless of the method of transition from state 1 to 2, at low values of B_t/B_g the value of the expression for the coefficient of $\frac{B_t^2}{2\mu_o}$ approaches zero. This is somewhat intuitive in that if the FRC is already compressed to the final transverse field pressure it should require very little extra energy to penetrate. The energy required to achieve this compression however is generally greater than that required to produce the equivalent kinetic energy, and to disregard this energy in the penetration analysis would be unrealistic. A more informative scaling relationship for the penetration of an FRC into a transverse field would be

$$\frac{1}{2}mn_1u_1^2+\frac{5}{2}p_1=\mathrm{K}\frac{B_t^2}{2\mu_o} \qquad [3.23]$$

where $p_1=\frac{B_g^2}{2\mu_o}$.

Equation [3.23] takes into account the enthalpy of the entering FRC, and is the meaningful relationship for evaluating the tradeoffs between initial compression and acceleration. To do this we define a parameter M_1

$$M_1=\left(\frac{mn_1u_1^2}{B_g^2/\mu_o}\right)^{1/2} \qquad [3.24]$$

which is an Alfven Mach number of the penetrating plasma. Equation [3.23] can then be written as

$$K = \frac{5}{2}\frac{1+\frac{2}{5}M_1^{\ 2}}{(B_t/B_g)^2} \qquad [3.25]$$

The relationship between $(B_t/B_g)^2$ and M_1 is evaluated for both isentropic and non-isentriopic penetration and equation [3.25] is then used to evaluate the effects of M_1 on reducing K below 5/2. For isentropic penetration, $(B_t/B_g)^2$ can be found (from equations [3.19]-[3.21]) to be

$$\left(\frac{B_t}{B_g}\right)^2 = \frac{\left(1+\frac{2}{5}M_1^2\right)^{5/2}}{1+\frac{1}{\sqrt{e}}}, \qquad [3.26]$$

while for non-isentropic penetration, the expression is more complex.

$$\left(\frac{B_t}{B_g}\right)^2 = \frac{\left(\frac{4}{5}M_1^2+\sqrt{\frac{16}{25}M_1^4+\left(1+\frac{2}{5}M_1^2\right)}\right)}{1+\frac{1}{\sqrt{e}}} = \frac{\frac{p_2}{p_1}}{1+\frac{1}{\sqrt{e}}} \qquad [3.27]$$

These equations lead to

$$K_{i.} = \frac{5}{2}\frac{1+\frac{1}{\sqrt{e}}}{\left(1+\frac{2}{5}M_1^{\ 2}\right)^{3/2}} \qquad [3.28]$$

for isentropic penetration and

$$K_{n.i.} = \frac{5}{2}\left(1+\frac{1}{\sqrt{e}}\right)\frac{4+\frac{4}{5}\left(\frac{p_2}{p_1}-1\right)}{4\left[1+\frac{4}{5}\left(\frac{p_2}{p_1}-1\right)\right]} \qquad [3.29]$$

for non-isentropic penetration. These expressions for K are plotted in figure 7 for various values of e.

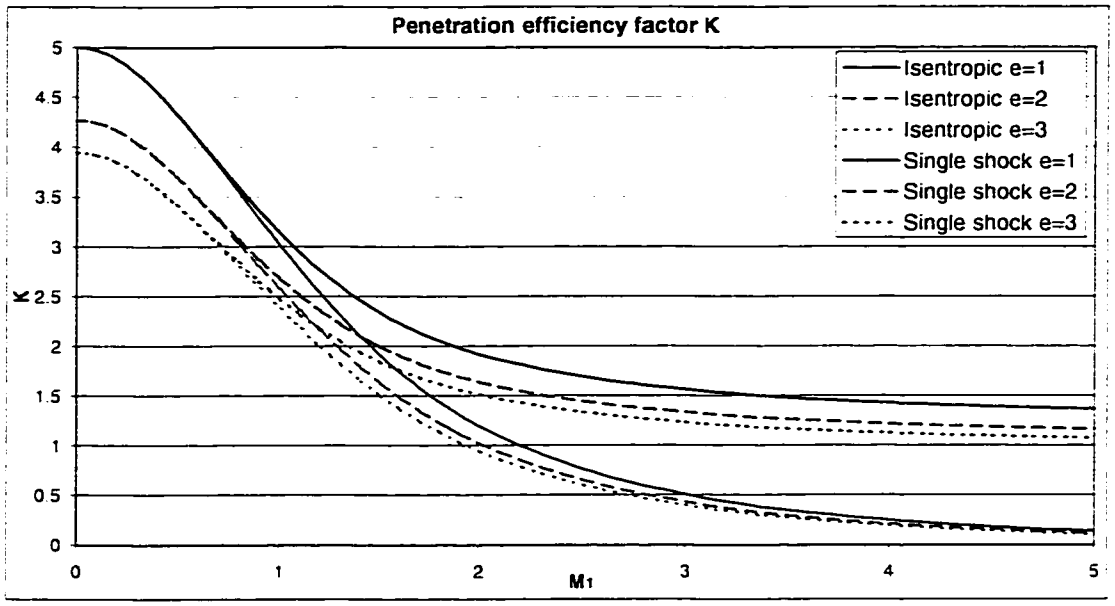

Figure 7. Efficiency of FRC penetration including enthalpy

FRC penetration is easier when the FRC deforms elliptically since it will not experience as high as a pressure in the transverse field nor will it require as much energy to exclude the field, but this advantage of ellipsivity drops off sharply after approximately e = 4. The K factor is higher than 5/2 in equations [3.28] and [3.29] for low values of M_1 since the enthalpy density of the FRC in the transverse field is higher than just p_2 by the factor $\left(1+\frac{1}{\sqrt{e}}\right)$. As M_1 increases, the insertion energy decreases and K drops below 5/2. This is due to the strong compression of the FRC.

For non-isentropic compression the results would be somewhat different. The compressed temperature will be higher, and the density lower for a given field into which the FRC penetrates. The FRC's radius will be larger and more of the translational energy will have to go into compressing the external magnetic

field. The method of compression of the FRC depends strongly on the scale length of the field gradient L_{fg} into which the FRC penetrates. For a gentle gradient where $L_{fg} \geq L_{FRC}$ the compression process should be isentropic, while for a sharp field gradient $L_{fg} << L_{FRC}$ the compression process should resemble a shock.

3.6 Axial Compression Considerations

The previous analysis assumed a uniform FRC at any position. In the presence of strong deceleration forces this will be inappropriate. The FRC mass will be concentrated in the front (just as it is concentrated in the rear during acceleration) and, even if the compression is isentropic, the total volume of the FRC may be larger than it would be if there was equilibrium along flux surfaces.

To examine these effects FRC penetration into a co-axial field gradient was modeled using a 2D, fully resistive MHD code with the FRC dynamics resolved in the r,z plane of the guide field. The gradient in field pressure experienced by the FRC in the transverse field was modeled by a conically shaped flux coil of the proper convergence and size to simulate the field gradient. The axial magnetic field does not change direction in the same manner at the transition from the guide field to transverse field and is a poor mock-up for the actual injector. The assumption of azimuthal symmetry in the 2D calculations will not reproduce the deformed FRC shape in the x-y plane of the transverse field. The radial changes in the 2D results must be interpreted as the average dimensional change of the FRC in the x-y plane, while the calculated FRC cross-sectional area should be accurate. The average field pressure experienced by the FRC is only approximately reproduced, but the FRC penetration should behave in a similar manner, if the penetration is based on P_2/P_1.

Using the same scaling relationship as given by equation [3.23], the value of K corresponding to simple isentropic penetration to the final axial field B_f would be

$$K = \frac{5}{2}\left(\frac{B_g}{B_f}\right)^{6/5} \qquad [3.30]$$

which is equivalent to the equation [3.28] result as e becomes large. Several simulation were made for various interaction fields and FRC velocities and masses to determine the relationship between (B_f/B_g) and M_1^* and to better understand and examine any departure from the isentropic penetration predictions.

The results of the calculations are shown in figure 8., where the density in equation [3.24] is taken as the FRC peak density. Completely isentropic penetration is represented on the graph by the line $\frac{B_t}{B_g} = \left(1 + \frac{2}{5}M_1^2\right)^{5/4}$.

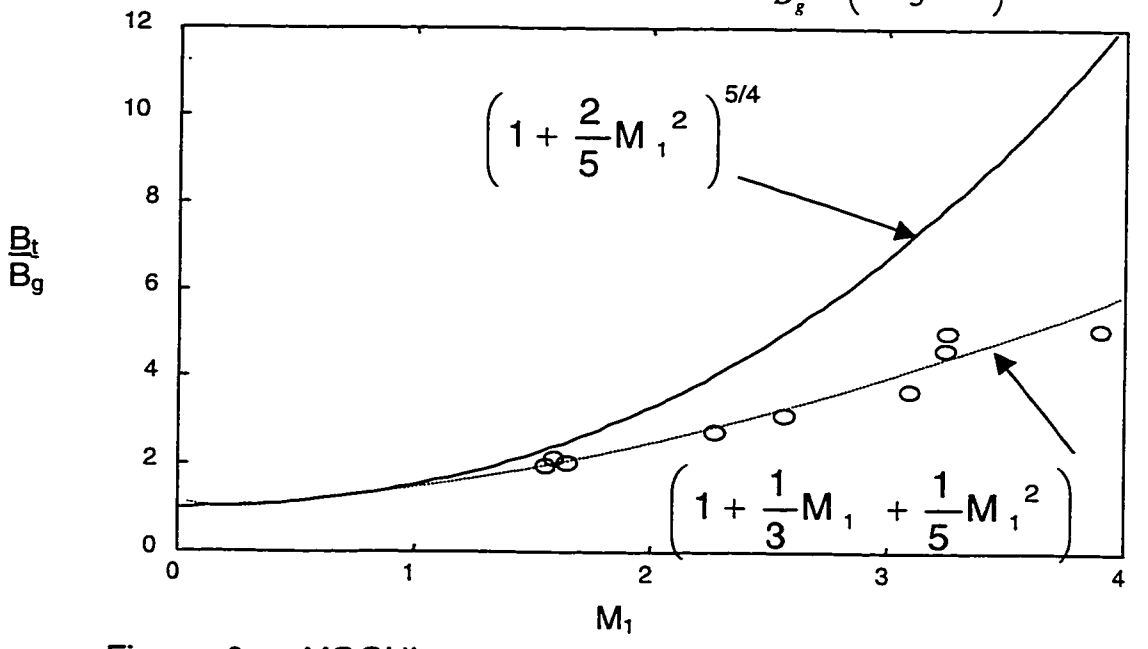

Figure 8. MOQUI penetration results showing ratio of maximum transverse field penetration to initial guide field as a function of directed velocity normalized to V_a. Solid curve is given by analytic isentropic model. Circles represent calculations with dashed line as a fit.

The MOQUI results for $M_1 \geq 2$ were fit to the dashed curve represented by

$$\frac{B_t}{B_g} = \left(1 + \frac{1}{3}M_1 + \frac{1}{5}M_1^2\right). \qquad [3.31]$$

The curve is not a very good fit for $1 < M_1 < 2$. For $M_1 \leq 1$ the isentropic result is approximately correct. The expressions for K for these two examples are then found from equation [3.25] to be

$$K_1 = \frac{5}{2}\frac{1}{\left(1 + \frac{2}{5}M_1^{\,2}\right)^{3/2}} \qquad [3.32]$$

for isentropic penetration into a coaxial field, and

$$K_2 = \frac{5}{2}\frac{\left(1 + \frac{2}{5}M_1^{\,2}\right)}{\left(1 + \frac{1}{3}M_1 + \frac{1}{5}M_1^2\right)^2} \qquad [3.33]$$

for the MOQUI simulations of penetration into a coaxial field. If one were to extrapolate the MOQUI results to a transverse field one would get a K factor of

$$K_3 = \frac{5}{2}\left(1 + \frac{1}{\sqrt{e}}\right)\frac{\left(1 + \frac{2}{5}M_1^{\,2}\right)}{\left(1 + \frac{1}{3}M_1 + \frac{1}{5}M_1^2\right)^2}. \qquad [3.34]$$

This expression for K is plotted in figure 9 for e = 3. Figure 9 also shows plots of the K expressions for isentropic penetration (equation [3.28]) and a single shock penetration (equation [3.29]) into a transverse field for an FRC with final ellipsivity e=3.

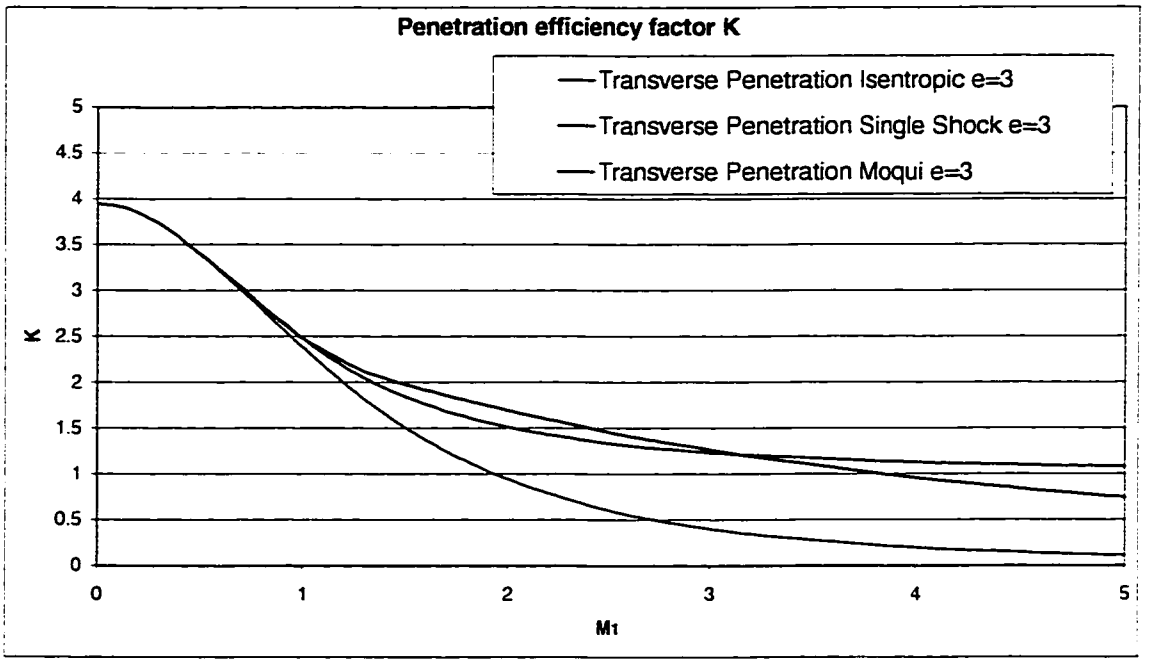

Figure 9. Simulations of FRC penetration including enthalpy

It was found from the MOQUI calculations that the field that the FRC center of mass reached was less than that predicted. For a given temperature FRC, the departure from the predictions became greater as the FRC velocity increased. The reason for this is seen most clearly for those extremely fast moving FRC's.

The penetration of the FRC depends on the mass density. At high velocities, the deceleration of the front flux surfaces of the FRC results in a rapid flow of the plasma along each flux surface to the front. The high β of the FRC means that there is little internal field pressure to retard this mass flow, and very rapidly there is a decoupling between the FRC mass and flux (see figure 10).

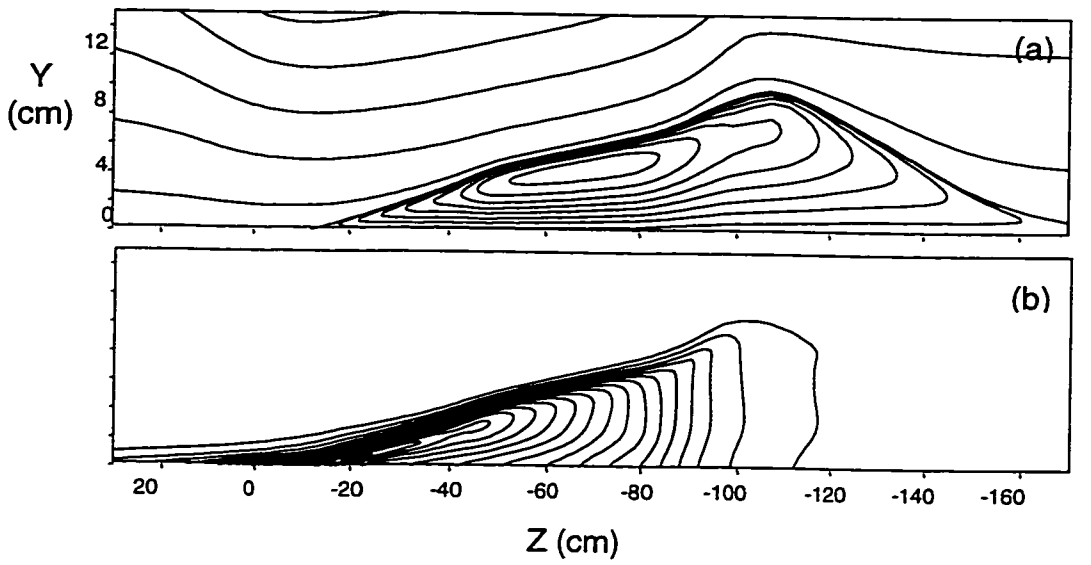

Figure 10. MOQUI calculated contours of (a) flux and (b) density for an FRC during penetration at high M_1^* (~3).

This behavior is seen in the experiment during the FRC acceleration, but in the opposite direction. With most of the flux surfaces left behind the FRC mass continues to penetrate at a much smaller cross-section and higher density, however, the FRC plasma is magnetized so that the flux must eventually be pulled in as well. The mass density retained with the flux is now much lower than that required to penetrate into the higher field region of the high density mass in front. Additionally, the region of low density is no longer in equilibrium with the external field. The external field compresses the flux and the now conical shape of the FRC causes the external field to push the FRC flux back. The flux then acts like a parachute that eventually drags the FRC to a halt prior to maximum penetration. The simulations show that although the FRC does compress, at high velocities, the de-coupling of the mass from the flux results in larger volume and a lower average density than a purely isentropic compression. It is unknown whether this 'parachuting' effect will occur during penetration into a

transverse field or what effect the transverse field might have on the severity of the effect.

If we assume that the MOQUI calculations outline the correct behavior of the FRC when penetrating into a transverse field, the results show poorer penetration into the transverse field than even the shock model when $1 < M_1 < 3$. The penetration does not seem to be as simple to analyze as single shock heating of the FRC, although the MOQUI results for $1 < M_1 < 3$ are closer to the single shock approximation than to isentropic penetration. A series of shocks may be better model.

The MOQUI calculations used a M_1 based on the peak density ρ_0 while the average number density $<\rho>$ would have a lower M_1 and would result in weaker penetration. Some of the kinetic energy of translation could also be lost to field line stretching of the internal FRC flux as the FRC experiences the 'parachuting' effect. Additionally, the FRC never seems to completely stop as the rear end starts to move backwards before the front completely stops and some of the kinetic energy of translation way be lost to residual kinetic energy of plasma oscillation.

The 'parachuting' effect reduces the benefit of operating at high M_1, but the increase in efficiency still makes it best to operate an FRC injector at high M_1. M_1 is limited only by the energy delivery rates from the accelerator power supplies, and the density at which the FRC can be formed. To minimize the energy per ion, we want to operate at the highest possible ρ_1, so high M_1 are best achieved by high density rather than velocity. FRC's should be formed at the highest possible densities while still maintaining a high enough temperature to allow for preservation of the plasmoid configuration during formation, acceleration, and injection.

The TRAP experiment operated at (Table 2.1) B_g=.54 Tesla with n= 0.56 x 10^{16} /cm^3 corresponding to a v_A of 1.11 x 10^5 m/s. Typical plasma velocities

were $1.6 - 2.0 \times 10^5$ m/s leading to M_1~1.44 to 1.8. For the FRC isentropically penetrating into the transverse field chamber with a deformed ellipsivity of 3 the maximum field into which it could penetrate based on these calculations is 0.91 Tesla to 1.22 Tesla, while for the FRC penetrating into the transverse field chamber, using the single shock model, with a deformed ellipsivity of 3 the maximum field into which it could penetrate based on these calculations is 0.84 Tesla to 1.02 Tesla. The maximum field that could be produce at the back of the transverse field chamber was 0.9 Tesla due to energy storage limitations. The experiment was not able to stop the injected FRC's, so was not a good test of the modeling used. Instead of looking at a stagnated FRC, we were forced to examine the deformation of the cross section of the injected FRC during penetration, and in order to do this we needed a model for the axial contraction of the FRC in the transverse field chamber.

The section 3.5 energy analysis of penetration is based on a large Tokamak or interaction chamber where the walls are very far away and wall effect terms in equation [3.12] can be ignored. For our experiment, the FRC radius in the transverse field chamber could not be assumed to be small compared to the chamber size, and the penetration energy was not just dependant on the final FRC volume, but on the details of the relationship between a and L_2. An axial compression model was needed to provide this relationship. Additionally, since the experiment was unable to effectively stagnate the FRC, an axial compression model was needed to compare modeled deformations and FRC cross sections with the experimental measurements of the FRC deformation and cross sectional area.

To provide the model an approximation is used to equate the change in cross sectional area of the FRC in the transverse field chamber to what it would be if it penetrated into a larger flux conserving axial field chamber with the same equivalent magnetic pressure. This is a rather extreme approximation, and it

breaks down as the radius of the larger flux chamber approaches infinity, but the transverse field chamber used is far from this condition.

When an FRC is transported between two coaxial flux conserving tubes with areas A_{tube1} and A_{tube2} while maintaining constant x_s, it can be shown that $\frac{B_{e_1}}{B_{e_2}} = \frac{A_{tube2}}{A_{tube1}}$. If the field in tube 2 is than increased to a new field B_{e3} to compress the FRC to a new cross sectional area dictated by pressure balance with the external field, the relationship describing this compression can be found to be[10] $\frac{B_{e_2}}{B_{e_3}} = \left(\frac{x_{s_3}}{x_{s_2}}\right)^{3+\varepsilon}$ where ε is a factor between 0 and 1 that depends on the FRC flux profile, and is typically between 0.2 and 0.3. Combining these two and relating to the change in cross sectional area of the plasma, creates $\frac{B_{e_1}}{B_{e_3}}\frac{A_{tube1}}{A_{tube2}} = \left(\frac{A_{plasma_3}}{A_{plasma_1}}\right)^{\frac{3+\varepsilon}{2}}\left(\frac{A_{tube1}}{A_{tube2}}\right)^{\frac{3+\varepsilon}{2}}$. Now rotate the field B_{e3} 90 degrees to a transverse field and allow it to decrease to a new field B_{e4} so as to maintain the FRC pressure balance and cross sectional area. The ration of B_{e3} to B_{e4} would depend on the ellipsivity of the FRC according to Equation 3.12 and would show $\frac{B_{e_3}}{B_{e_4}} \cong \sqrt{1+\frac{1}{\sqrt{e}}}$. This analysis finally yields the relationship

$$\left(\frac{A_{plasma_4}}{A_{plasma_1}}\right) = \left(\frac{B_{e_1}}{B_{e_4}}\right)^{\frac{2}{3+\varepsilon}}\left(1+\frac{1}{\sqrt{e}}\right)^{\frac{-1}{3+\varepsilon}}\left(\frac{A_{tube2}}{A_{tube1}}\right)^{\frac{1+\varepsilon}{3+\varepsilon}}. \qquad [3.35]$$

The minor radius of the elliptical plasma in the transverse field can then be inferred from the cross sectional area simply by $a = \sqrt{\left(\frac{A_{plasma_4}}{A_{plasma_1}}\right)r_1^2\frac{1}{e}}$. The energy analysis including wall effect terms on pressure then proceeds. The minor radius of the FRC and the transverse field strength yield the plasma pressure according

to Equation 3.12 The plasma pressure and the isentropic relations then yield the plasma density and temperature, and the energy equation then yields the velocity.

To additionally verify the field requirements needed to completely stagnate the penetrating FRC in a finite dimensional chamber and to examine the remaining forward velocity of the FRC as it penetrated into the experimental transverse field gradient, numerical calculations of the energetics model utilizing the full pressure relationship (equation [3.12]) were carried out based on the typical plasma conditions observed during the operation of the TRAP experiment. Plasmas were regularly accelerated to velocities of ~1.6 to 2.0 x 10^5 m/sec with plasma total temperatures and number densities of T_e+T_i ~80 to 100 eV and n ~ 0.7 to 1.0 x 10^{22} /m^3. The FRC's were typically 1.20 to 1.70 m long with a radius of 60 to 100 mm. The transverse field chamber used on the TRAP experiment was a squat cylindrical stainless steel vacuum vessel set onto its side, with a large port for plasma injection, and capped on top and bottom with stainless steel flanges. The chamber had an I.D. of ~ .90 m and was ~ .60 m high.

For the purposes of the numeric calculations, the transverse field chamber was modeled as a rectangular flux-conserving channel 60 cm high and 90 cm wide. The FRC was assumed to be centered in the chamber for the transverse field perturbation model. The initial plasma conditions of the accelerated FRC were T_t = 90 eV, V = 1.8 x 10^5 m/sec, n = 0.76 x 10^{22} /m^3, r_{plasma} = 72 mm, and L_{plasma} = 1.60 m. The simple relationship

$$\frac{1}{2}mn_1u_1^2 = \frac{1}{2}mn_2u_2^2 + \frac{B_t^2}{2\mu_o} \qquad [3.36]$$

(which reduces to equation [1.1] when u_2=0) would predict that a plasmoid of this number density and velocity would penetrate an ~ 1 Tesla field before being completely stopped.

The results of the numeric calculation for the remaining forward velocity of an FRC, after penetration are shown in figure 11 as a function of B_T. The calculations were performed with an initial confining field of B_e~ .57 Tesla, so that transverse fields less than ~.4 Tesla result in additional acceleration.

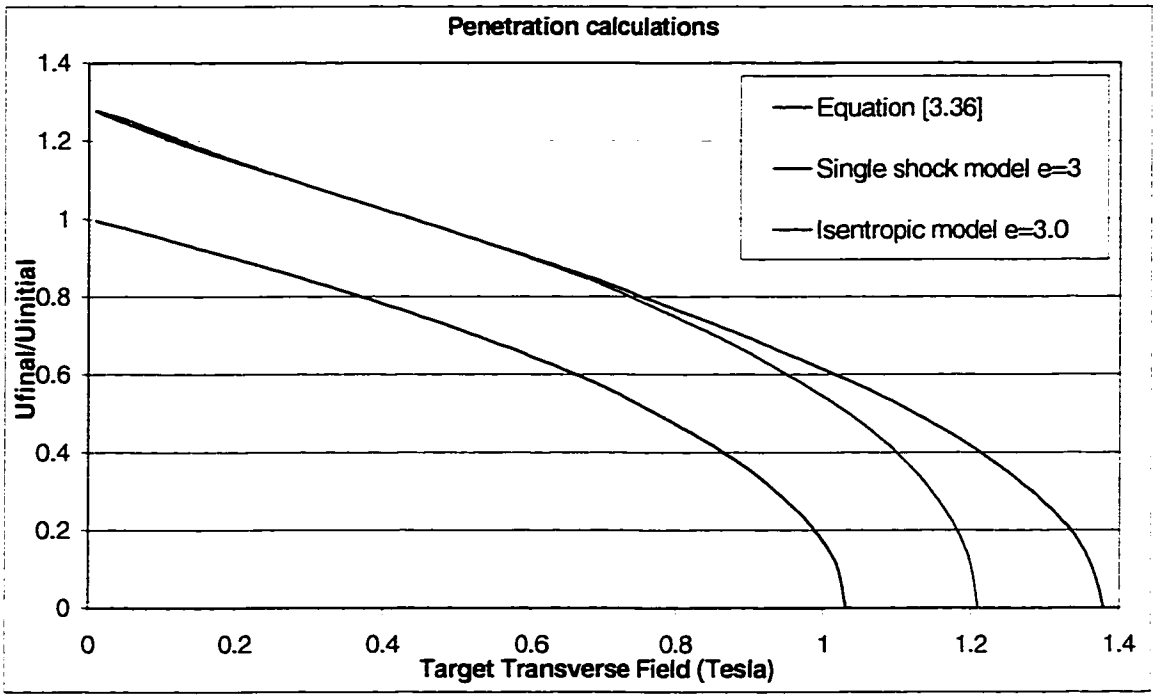

Figure 11. Numerical penetration results with wall effects

Again as expected, regardless of the method of penetration, the maximum field into which the FRC could penetrate before being completely stagnated is higher than the peak field that could be produced in the transverse field chamber. The numerical calculations still provided information on the expected velocity of the penetrating FRC that could be compared to experimental results given the appropriate diagnostics. Unfortunately, we were not able to accurately gauge the velocity of the FRC in the transverse field chamber while operating the TRAP experiment.

Chapter 4

TRAP Experimental apparatus

An overall layout of the TRAP experimental apparatus is shown in figure 12, showing the vacuum chamber, formation chamber, acceleration and transport sections and interaction chamber.

4.1 Formation chamber

The formation section consists of a 40-cm ID 2.5 meter long quartz plasma tube with (20) 46-cm diameter single turn coils arranged in 8 individually powered groups. As shown in figure 13, the left most group acts as a plug coil and only has bias modules attached to it. The central three groups are connected together and form a one meter long central section where the FRC is initially formed. The two 25-cm long groups on either side act as fast trigger/plug coils to program the formation and control the ejection of the FRC. A joint at the end of the formation section forms the junction between the 40-cm diameter formation tube and the 27-cm diameter acceleration tube.

4.2 Acceleration and transport sections

The acceleration section is a 27-cm ID, 2 meter long quartz tube driven by 8 acceleration coils with effective diameters of 30-cm. The 8 acceleration coils are 3-turn coils and are connected in (4) 50-cm long groups. They are powered by both bias field and fast bank modules. An additional joint forms the junction between the acceleration section and the transport section.

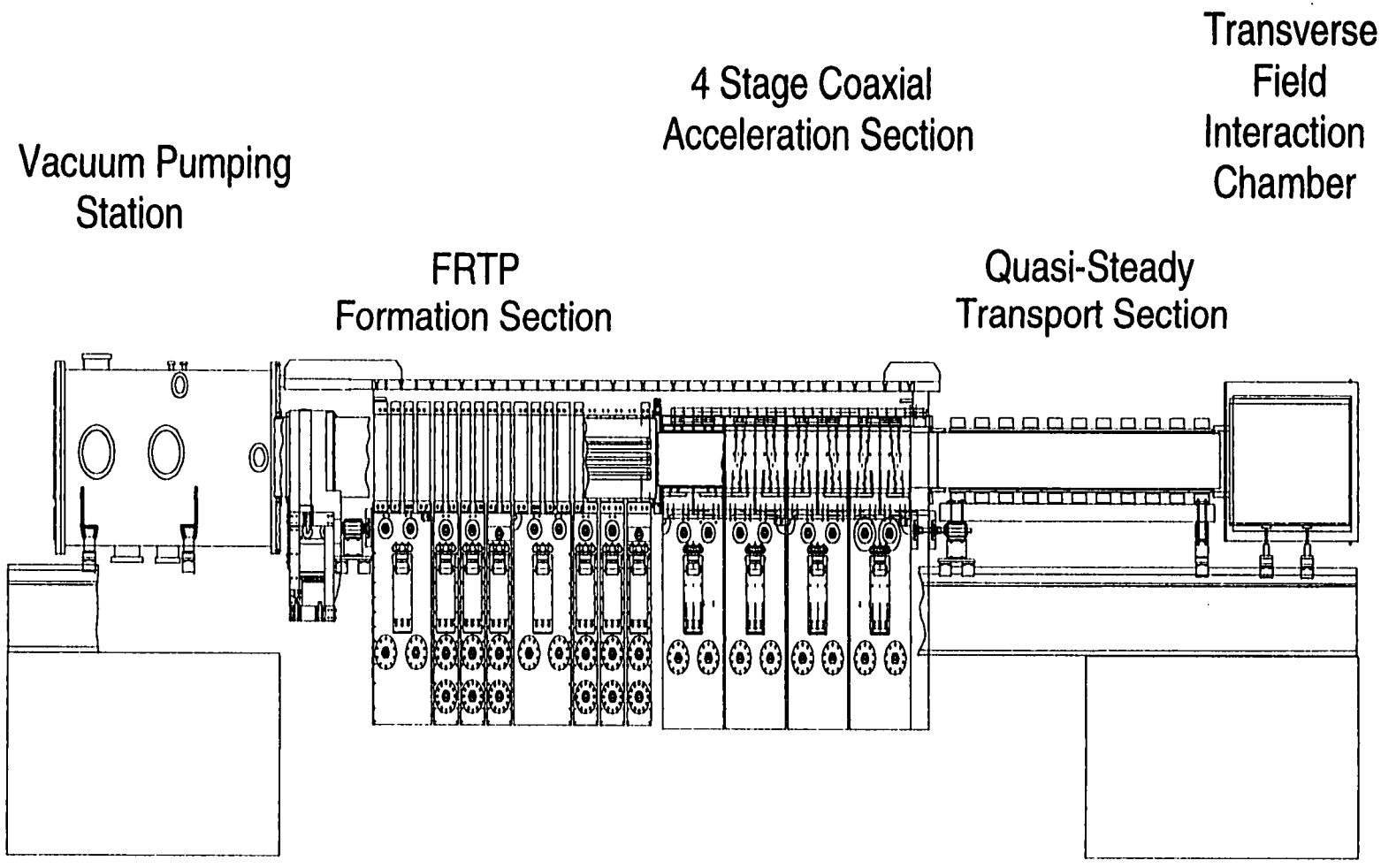

Figure 12. Overall TRAP Configuration

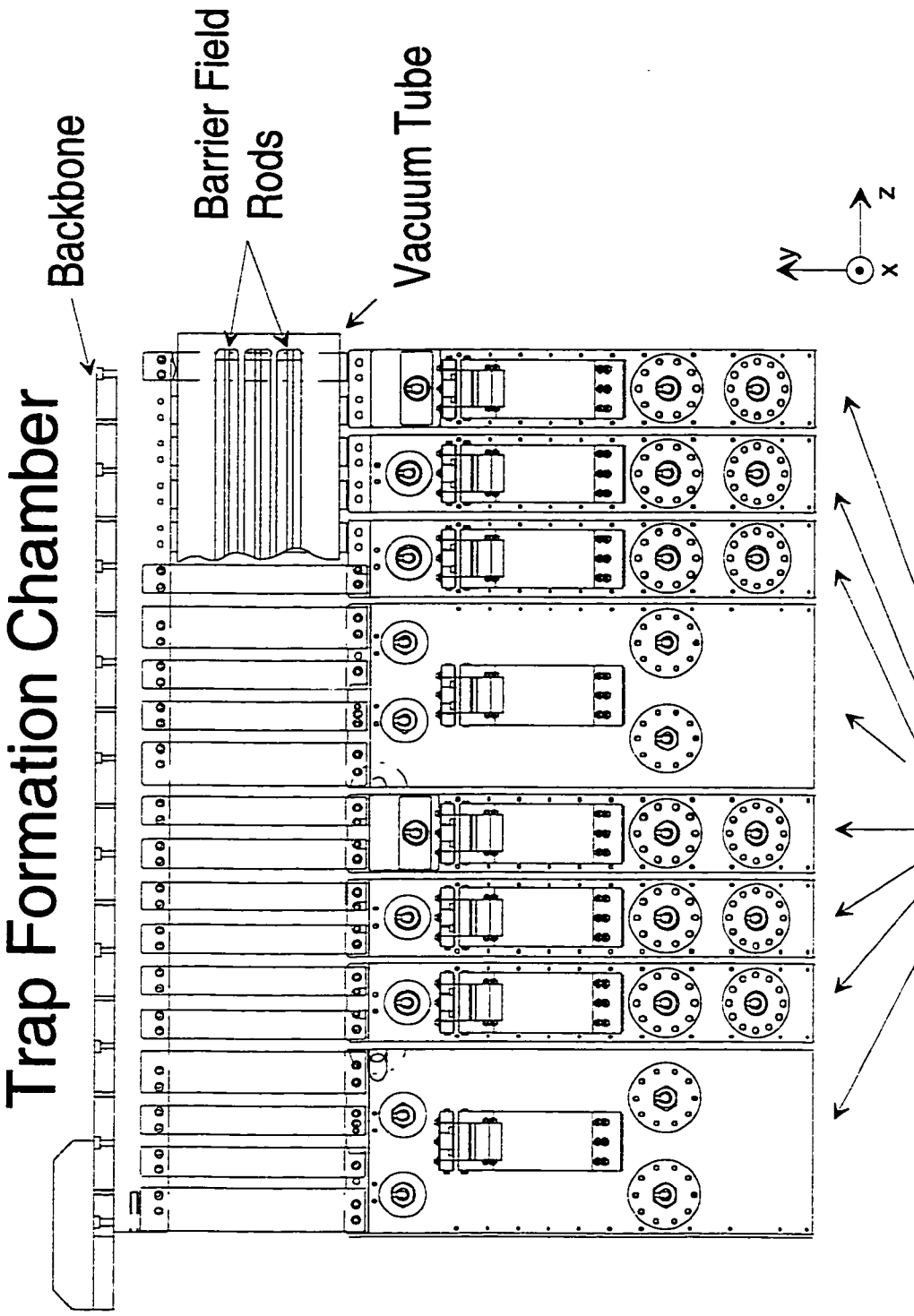

Figure 13. TRAP Formation Chamber

The transport section is a 27-cm ID, 2 meter long quartz plasma tube designed to transport the FRC from the acceleration section into the interaction chamber in the same manner that would be required in an actual large Tokamak. As seen in figure 14, the transport tube is surrounded by a quasi-steady solenoidal magnet set to provide radial confinement for the FRC. The solenoidal magnet set consists of eleven 40-turn coils connected in series to two bias bank modules. The magnetic field rise time is 2 msec. The transport tube could have been constructed out of thin walled stainless steel, but was constructed from quartz to be interchangeable with the accelerator section tube and to allow good diagnostic access. 3/16" stainless cases are used about the individual coils to provide flux conservation during the fast passage of the FRC. In order to make the individually connected solenoid coils provide a uniform field, an aluminum flux shaper consisting of an axially split aluminum shell, is inserted between the coils and the plasma tube. As long as the gap between magnetic sections is small, and the gap between the shell halves is small, there should be a uniform voltage across the gap, and an axially constant flux inside the shaper.

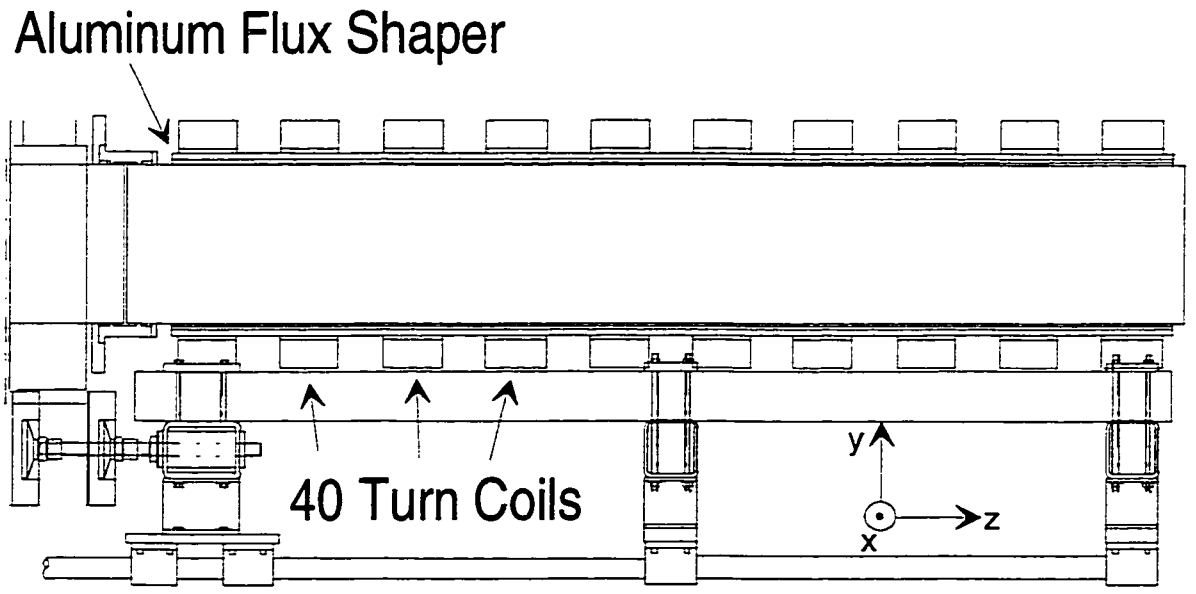

Figure 14. Transport Section

4.3 Interaction Chamber

The interaction chamber was constructed to act as a mock-up of a Tokamak, with the transverse (toroidal) field provided by a pair of rectangular Hemheoltz-like quasi-steady coils arranged in a 'pie-piece' or 'V' geometry. A top view of the interaction chamber is shown in figure 15. The diameter of the interaction chamber is 90 cm and it is 60 cm high. The interaction chamber is just large enough to give some information about the behavior of the FRC as it leaves the axial field of the accelerator and enters the transverse field.

Two 152-turn rectangular coils were procured to be used in the 'V' shape shown. Each coil has an inductance of about 50 mh, and is powered in series by a 9.6 mf, 10 KV capacitor bank. The 47 msec quarter cycle time is long enough to ensure full penetration of the flux into the stainless steel interaction chamber with acceptable losses. The angle and spacing of the interaction coils produced a transverse field and field gradient that simulated a Tokamak with a major radius of ~ 1.3 m and an aspect ratio of 3. Due to energy storage limitations, the peak field was limited to less that 1 Tesla in the interaction chamber.

The top flange of the interaction chamber had extensive diagnostic ports, consisting of one large central window surrounded by eight smaller ports. The central window was used primarily for visible light photography, while the smaller ports allowed for the insertion of internal probes. The bottom flange had attachments for 8" and 10" flanges that allowed for additional diagnostics (either internal or non-invasive). Two 2 ¾ " flange, 1 ½ " I.D. ports were accessible through the chamber on the sides in the middle of the chamber at a 90^0 spacing from the transport tube entrance. Additional small ports were machined into the sides of the interaction chamber to allow for the insertion of small (2mm Dia)

quartz tubes into the chamber. The use of the quartz tubes will be described in the diagnostics section.

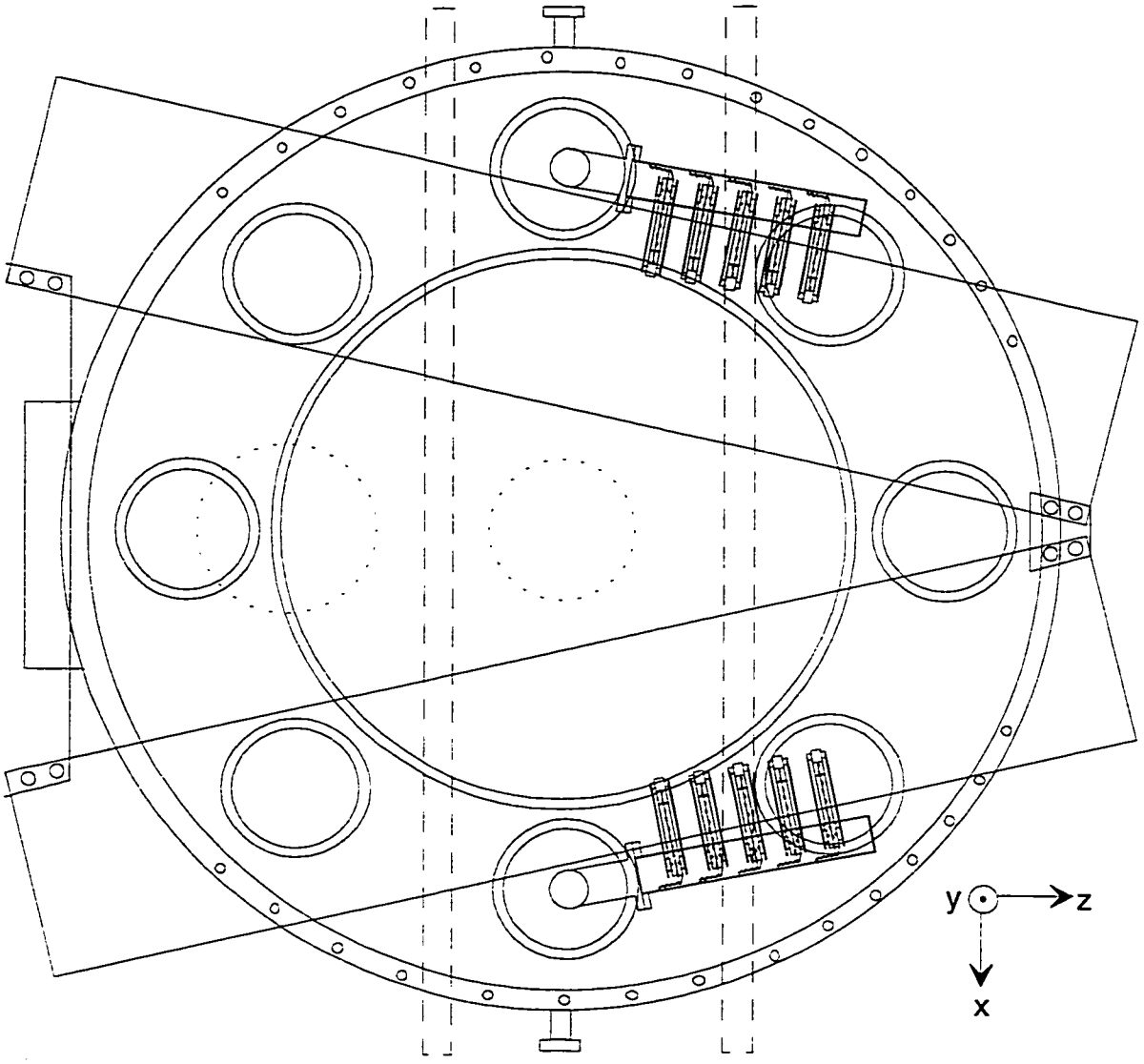

Figure 15. Interaction Chamber Top View

Chapter 5

Experimental Operation

5.1 FRC Acceleration

The description and analysis of the acceleration process used on the TRAP experiment is explained in greater detail by J.A. Grossnickle[11], but briefly the TRAP device was built to utilize the existing LSX apparatus. The capacitor banks, cabling, and ignitron switches were all designed for use on the much larger and longer time scale LSX experiment. Utilization of the LSX power supply system for TRAP presented some unavoidable difficulties. The power supplies did not inductively match well with the TRAP coil system, and imposed severe restrictions in the acceleration section. The smaller diameter acceleration coils had to be designed to match the relatively high inductance power supplies, and were built with three turns. This caused them to have a high, ~14 μsec quarter cycle time. Ideally rise times with normal single turn coils could have been one-third this value with low inductance power supplies of the same ~30 kV voltage.

The slow acceleration coil rise times required the study of larger mass, ~0.8 mg, FRC's for acceleration. These FRC's required ~10 - 5 μsec rise times whereas smaller FRC's, ~0.4 mg or less, would have required less than ~5 μsec rise times. Even the larger mass FRC's were not fully or efficiently accelerated by the TRAP acceleration section, but were a closer match to the TRAP coil system than the smaller mass FRC's. For efficient fueling, the higher mass, high density FRC's were of most interest since high density minimizes the kinetic energy per particle required to penetrate a given toroidal field.

Field reversed configuration plasmas were formed and accelerated to high velocities in the TRAP device. FRC's with initial fill pressures of 5, 10, and 20 mTorr D (~0.2, ~0.4, and ~0.8 mg D) were studied, with the 20 mTorr FRC's given the most attention. FRC's formed with fill pressures of 20 mTorr showed the best results due to a better match of their velocity and the long rise time of the capacitor banks and acceleration coils. Final velocities in the guide field region of 200 km/s, with 0.6 mg final mass and 1.5×10^{22} m^{-3} peak density were achieved. The total kinetic energy was ~13 kJ, with acceleration efficiencies approaching 35%.

FRC's were formed in the TRAP device via the FRTP formation process outlined in Chapter 2. Initial bias field in the source was -3 kG with the forward field reaching ~1 T. Bias field in the acceleration section ranged from +1 kG for the first coil to +2-3 kG for the last three coils. A low first coil bias field was necessary for the larger mass FRC to be drawn out of the source section into the acceleration section. Due to slow coil rise times the accelerator coils had to be fired early. A high first coil bias would not allow the FRC to escape the source quickly enough, and consequently the back end of the FRC was cut off and trapped in the source by a mirror caused by the first accelerator coil. The forward field in the acceleration section, the acceleration field, ran between 8-10 kG. The transport field, all forward bias, ran between +3 and +5 kG depending on whether or not additional FRC compression was desired.

FRC position, FRC shape, poloidal flux, and external field data were provided by diamagnetic loop arrays. Density and mass position information was provided by an interferometer and emission arrays. An example of a typical 20 mTorr fill pressure acceleration shot can be seen in figure 16. This 0.8 mg initial mass FRC was accelerated to a final velocity of ~200 km/s with an associated kinetic energy of ~13 kJ. This shot was simulated using a 2-D code known as MOQUI in an attempt to gain more knowledge of the internal FRC structure, mass and flux loss, and final velocity and density. Plots of FRC velocity and

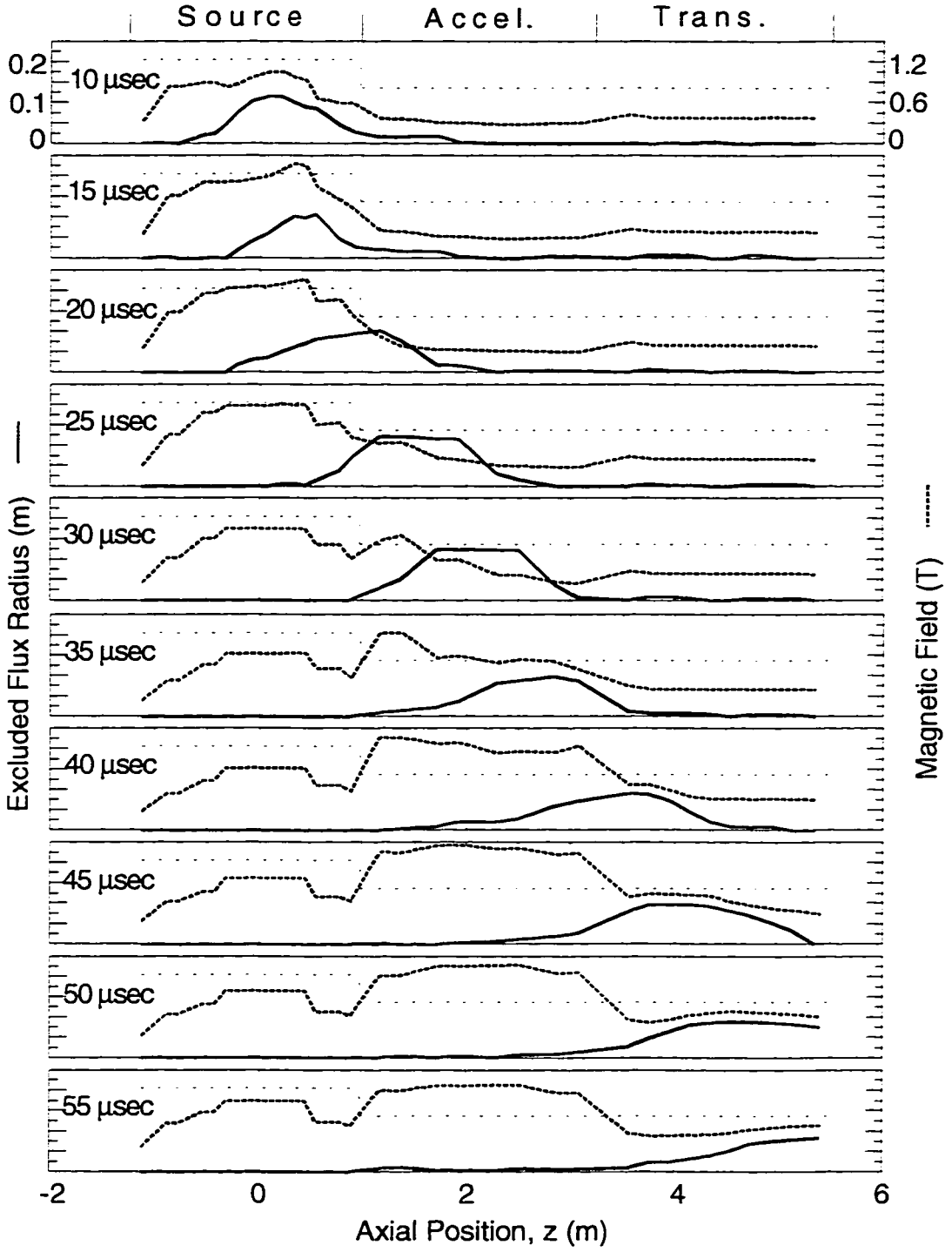

Figure 16.

Excluded flux radius and magnetic field for a 20 mTorr shot (1647). Final velocity ~200 km/s, acceleration ~0.65 cm/µsec^2, final KE ~13 kJ.

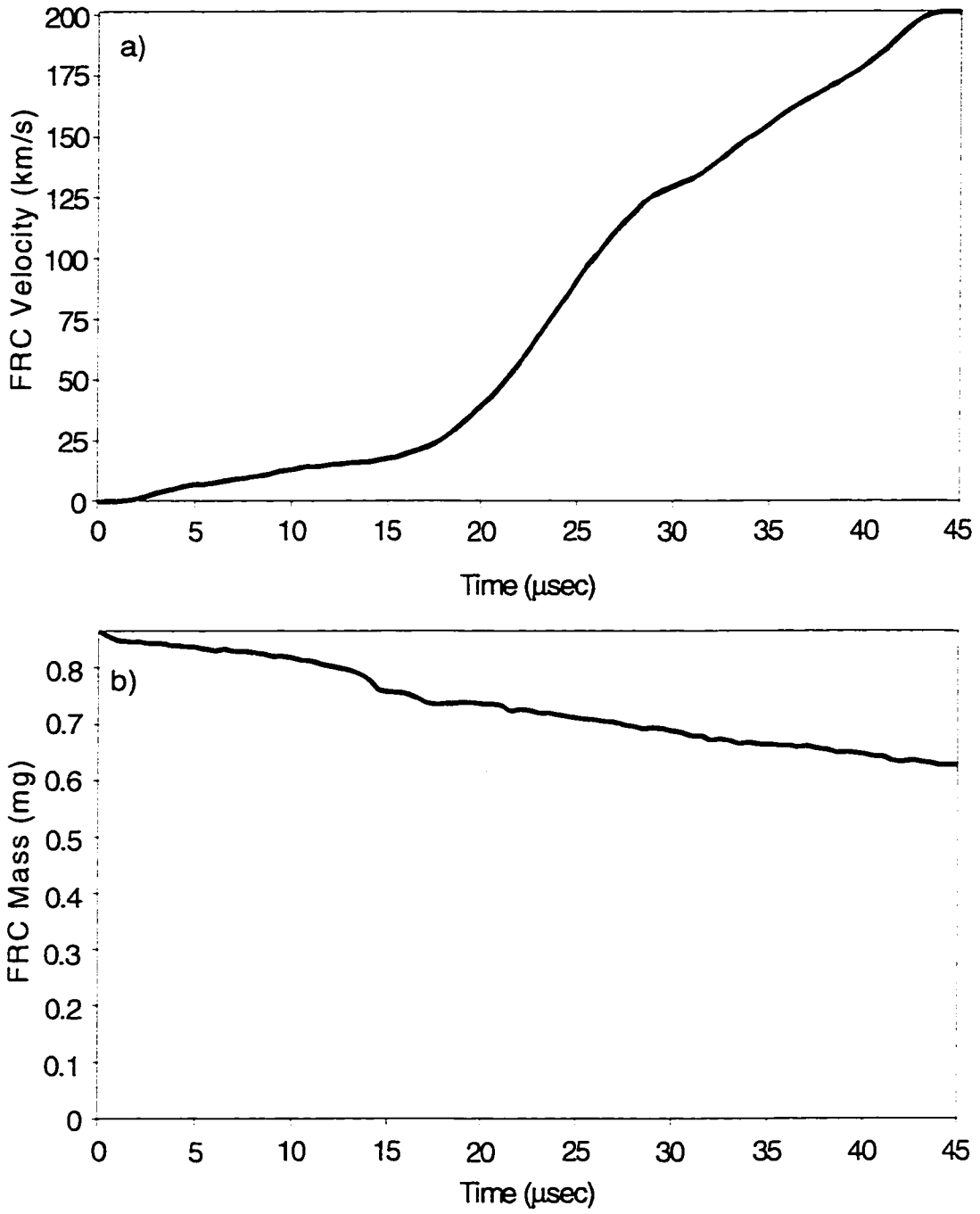

Figure 17.

FRC a) velocity and b) mass versus time from a 20 mTorr MOQUI simulation with parameters corresponding to shot 1647.

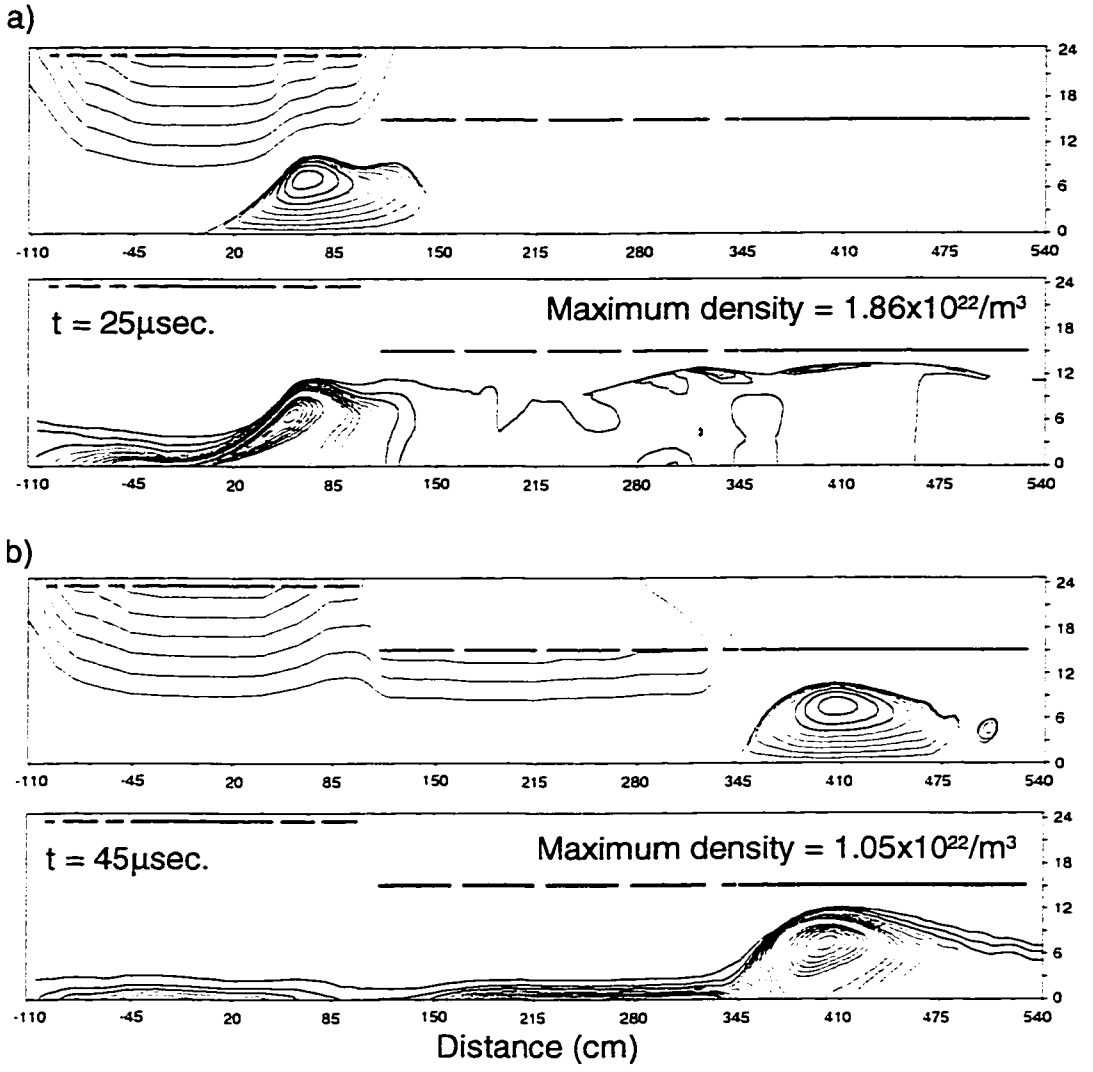

Figure 18.

Flux and density contours from a 20 mTorr MOQUI simulation with parameters corresponding to shot 1647 at a) 25 µsec and b) 45 µsec.

mass versus time, as well as flux and density contours from the MOQUI simulations, are presented in figures 17 and 18.

5.2 Transverse field injection

As mentioned, the FRC's were formed in the TRAP device using a puff fill FRTP formation process. Once the formation process was found to be consistent and reliable, the acceleration of the FRC's was studied in detail. Optimal firing times for the magnets were determined to produce maximum possible acceleration on the FRC for the various fill pressures, despite the problem that the FRC's were not fully or efficiently accelerated by the TRAP acceleration section due to the slow rise time of the acceleration magnets. After the acceleration process had been optimized, the experiment ran for several months to allow sufficient time for data collection on the acceleration process.

Upon arrival the transverse field magnets were installed, the capacitor banks were tested, and the transverse field magnets were then tested and calibrated. The transverse field was calibrated over a series of several shots with the transverse field coils energized to 2.5 kV. An internal B probe recorded the field at a number of points along the axis of the experiment ($\Sigma(z_i,x=0,y=0)$).

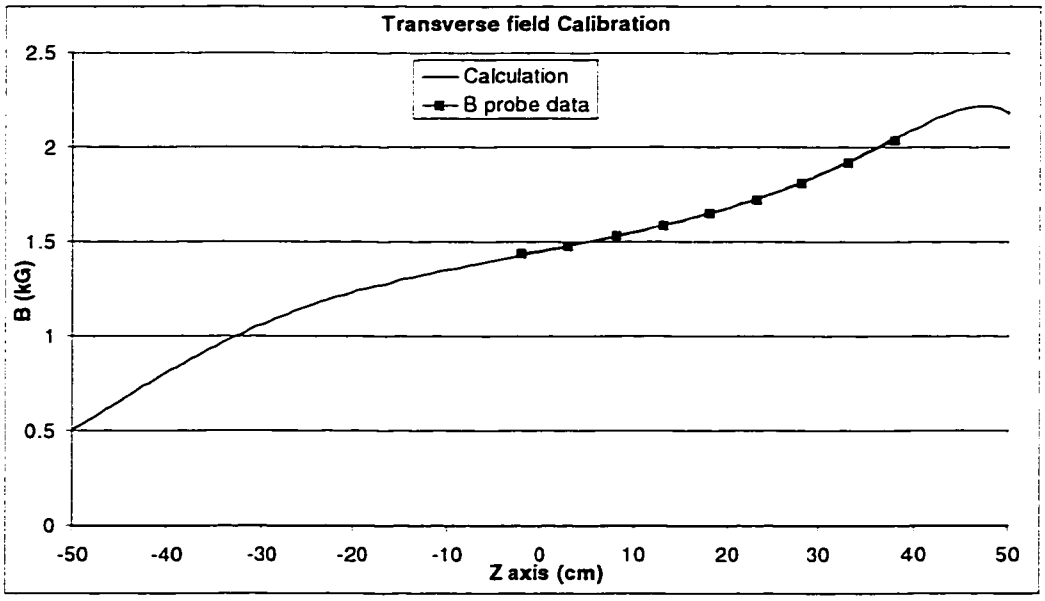

Figure 19. Transverse field calibration

The B probe used was a 7 turn rectangular cross section probe with an area of ~ 1.43 X 105 mm^2 and a nA of ~10^6 mm^2. The signal was numerically integrated and calibrated and then compared to Biot-Savart calculations based on the transverse field magnet currents. The calculated field magnitudes and the probe data are shown in figure 19, and matched extremely well.

The experiment then ran for several weeks with the transverse field energized at different levels, while several diagnostics were employed and tested. During this period external B probes recorded the perturbations of the transverse field caused by the injection of the plasma and visible light imaging cameras examined the gross motion of the plasma during injection. Initial images showed extreme light up at the entrance to the transverse field chamber indicating that the plasma was hitting the steel tube at that location. To correct this problem, an additional magnet was designed and built to slide over the steel tube at the throat of the transverse field chamber so as to extend the guide field further into the transverse field chamber and keep the plasma from hitting the steel tube. Although necessary, this however caused other problems.

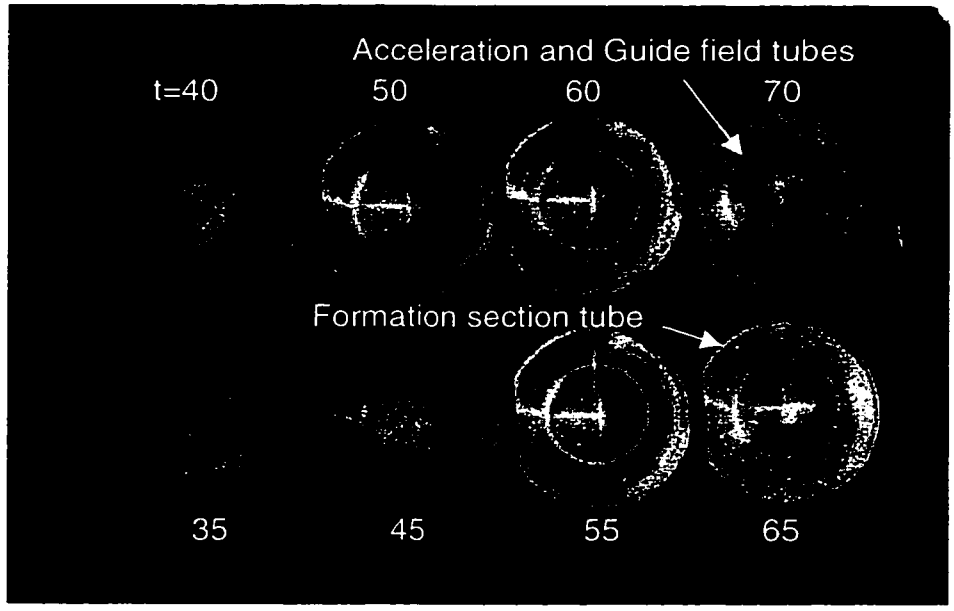

Figure 20. Imacon picture of FRC during injection. All times in μsec.

During the initiation of plasma penetration, the visible light imaging camera consistently showed bright light up on the left side of the guide field tube as shown above in figure 20. The camera viewed light between 510nm and 600nm wavelengths and produced an eight frame picture of the plasma. The frames start in the lower left corner of the picture at 35 μsec and proceed up and to the right at 5 μsec increments. Each frame has an exposure time of approximately 1 μsec. The crescent on the left side of the quartz tube at the t=45 μsec frame in figure 20 indicates that the plasma is hitting the wall on the left as it begins to enter into the transverse field chamber. In order to better visualize the plasma deflection, two thin (2mm dia.) quartz tubes were placed in a cross hair near the throat of the transverse field chamber at z=-33cm. The t=50 μsec frame of figure 20 shows the plasma after it has begun to penetrate into the transverse field chamber and has made contact with the quartz tube "cross-hairs." The light up from the plasma contact was very noticeable to the left of center.

Further investigation and simulations led to a realization of the significance of the magnetic field gradient at the throat of the transverse field chamber. This gradient was due to the mixing of the transverse field and the axial guide field, and it resulted in a sideways push of the FRC. Several attempts were than made to eliminate or minimize the sideways field gradient.

The first attempt was to "screen out" the transverse field from the throat of the chamber by placing two 18 inch high by 9 inch wide by 1 inch thick copper plates near the throat perpendicular to the transverse field. A magnetic probe then determined that the transverse field was reduced by 50 % in the region between the two plates. Larger plates could have been more effective but were not used due to their weight and the difficulty attaching them to the experiment. The second attempt was to "screen out" the transverse field from the throat of the chamber by constructing two small magnets that would generate a field opposite to the transverse field in the region of the chamber throat. This method

was also examined with a magnetic probe and found to be about as effective as the copper plates. Eventually, the focus of the experiment shifted more toward characterizing the sideways field gradient, and examining the effect it had on the plasma trajectory.

5.3 Magnetic field calculations and FRC deflection

To evaluate the gross effects of the mixing of multiple fields as well as the field perturbations caused by the FRC penetrating into the transverse field interaction chamber, several numerical computer programs were used to calculate the magnetic fields of the experiment. These programs were 3-D Biot-Savart solving field calculations written in IDL (Interactive Data Language) for the known magnetic coil geometry. Programs were used to calculate the field from the transport coils, as well as the field from the interaction chamber transverse field magnets. These calculations allow for easier field visualization and aide in diagnostic placement. Additional 2-D programs were used to simulate the perturbations caused by a flux excluding FRC penetrating the transverse field. A plot of the transverse magnetic field magnitude in the interaction chamber for the typical bank voltages is shown in figure 21.

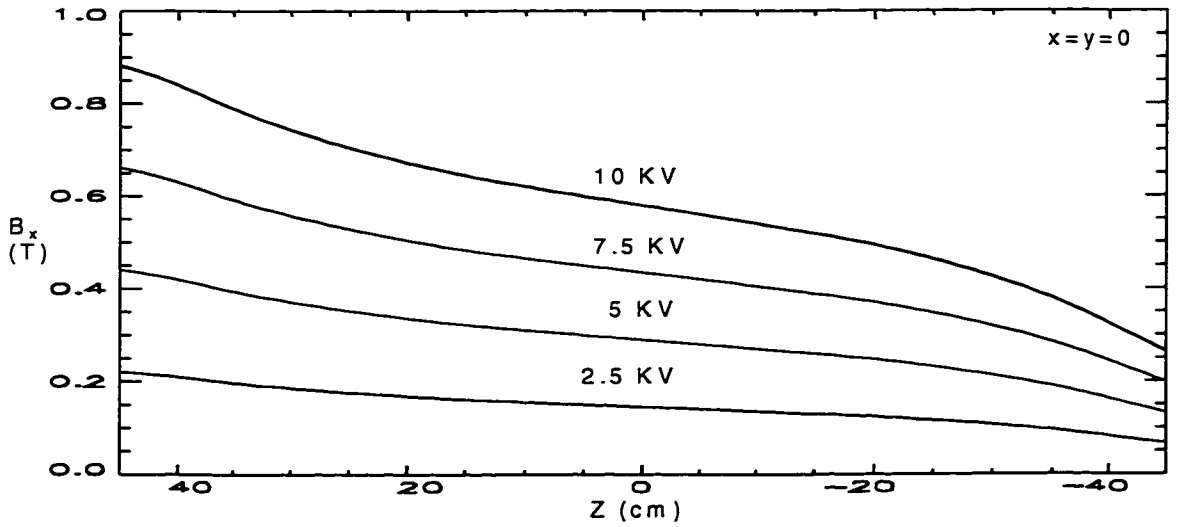

Figure 21. Interaction chamber field strengths

Figure 21 shows magnetic field calculations for the transport coils energized to ~4.5 KG and the interaction field energized to ~ 7 KG at the back of the interaction chamber. The plot of the magnetic field vectors for the joint interaction chamber field and transport field in the x-z plane shows that the magnetic flux inside the transport coils can be seen to map into the toroidal field in the same direction. Again, the most noticeable effects are the bending around of the transport flux as it exits the last transport coil and proceeds into the interaction chamber, and the field gradient in the transverse (x) direction in the throat of the interaction chamber entrance.

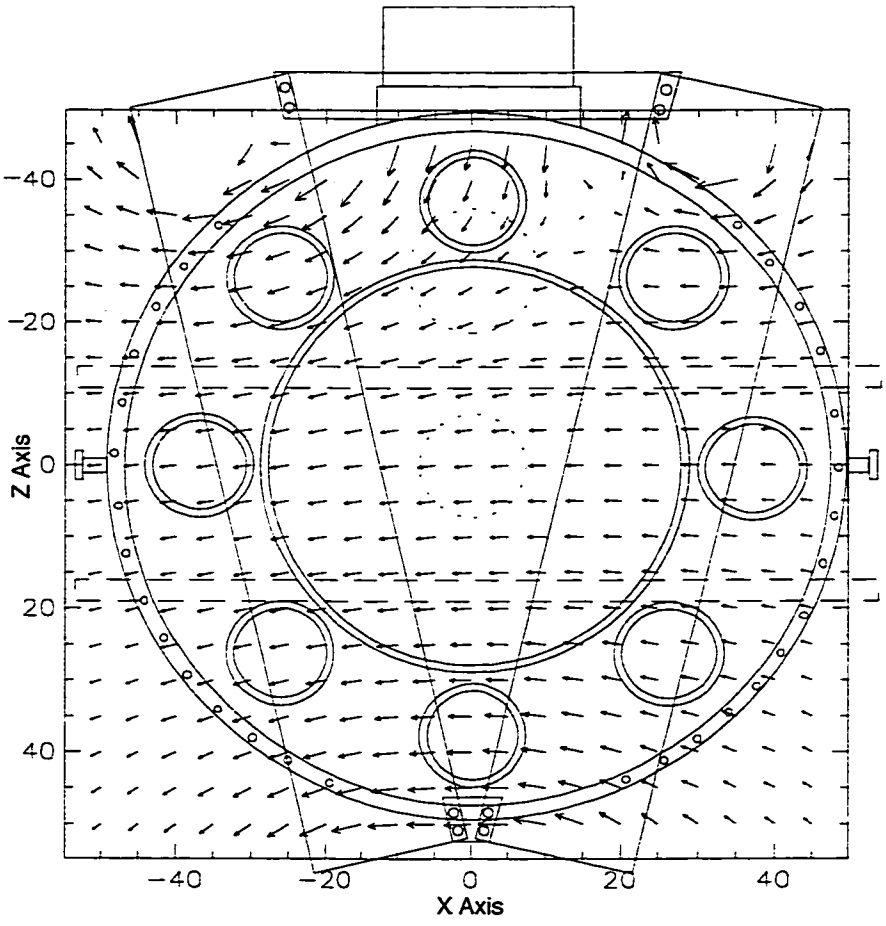

Figure 22. Calculated fields in interaction chamber

Figure 23. shows the calculated B^2 pressure forces in the x direction. The total sideways impulse imparted to the FRC can be roughly calculated, and from this the imparted sideways velocity can be inferred. For r_{frc} = 10 cm, V_{frc} = 20 cm/μsec, and L_{frc} = 130 cm, the total imparted impulse is calculated to be 1.3 x 10^{-2} Kg m/sec. This would equate to an imparted velocity of approximately 2.1 cm/μsec for a 0.6 mg FRC (20 mtorr fill pressure). Slower, lighter FRC's could experience greater impulses and could see sideways imparted velocities of 3 to 6 cm/μsec. The pressure gradient was an inevitable result of the curvature of the transverse field mixing with the guide field.

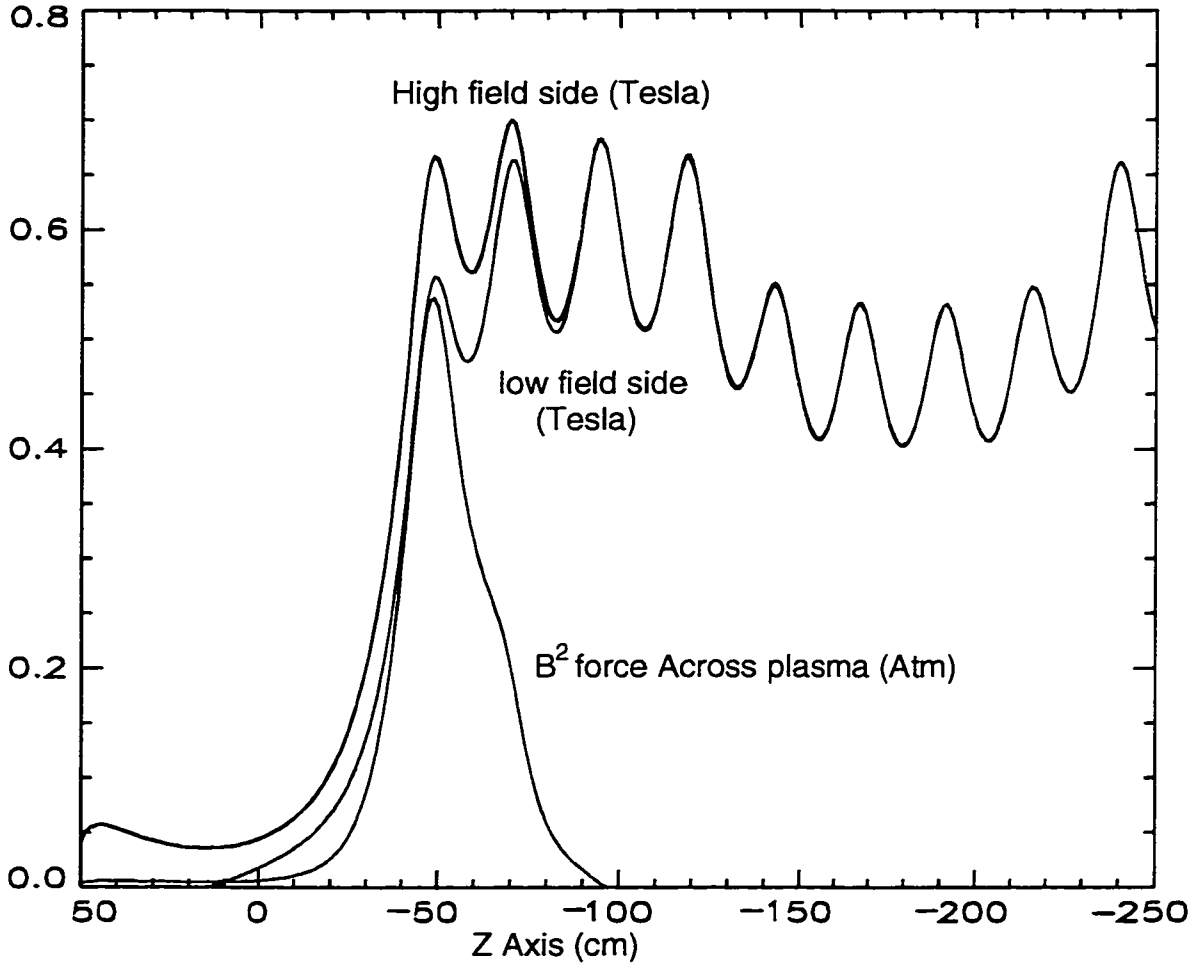

Figure 23. Magnetic field code results

This sideways force caused the FRC to inject at an angle from normal with respect to the transverse field (with the angular displacement increasing with increasing transport or transverse field). In an actual injector, this non perpendicular trajectory could be advantageous in that it allows for a trajectory that initiates the tilting of the FRC as well as providing for increased dwell time in the Tokamak field for disassembly and fueling.

The injection angle of the FRC was dependant on the forward velocity of the FRC and the velocity imparted to the FRC as it traversed the field gradient region. The forward velocity of the FRC was a known parameter. The imparted sideways velocity was evaluated in the following manner and then compared to experimental results.

The imparted velocity Δv of the FRC after it translated through the region of sideways force should be the imparted impulse divided by the FRC mass M, where the impulse is just the product of the sideways pressure force times the time of influence.

$$\Delta v = F\Delta t/M \qquad [5.1]$$

The sideways force and the time of contact can be related to the guide field $B_{gz}(z)$ (along the axis of injection) and the transverse field $B_{tz}(z,r,\theta)$ (perpendicular to the axis of injection), where the additional subscript z denotes the components of that field in the z (axial) direction. An expression for the imparted impulse can be found using the following method:

$$F\Delta t = \int_0^{L_{tf}} F_x \frac{dz}{U_{frc}} \qquad [5.2]$$

Where F_x is the force in the x direction exerted by the pressure of the combined magnetic fields acting over the $2\pi r_{frc}L_{frc}$ surface of the cylindrical FRC. L_{tf} is the length of the region of influence on the plasma of the combined fields and can be approximated as the region where the z gradient in the transverse field is

approximately linear. For most injector geometry's, L_{tf} is approximately the major radius of the toroidal or transverse field.

The pressure of the combined magnetic fields acting over the surface of the FRC cylinder is $(B_{gz}+B_{tz})^2$. The force exerted by the pressure will be in the x-y plane perpendicular to the external magnetic field and the experimental axis (z-axis). The component of the pressure forces in the x direction is $(B_{gz}+B_{tz})^2\sin\theta$ where $\theta=0$ is the negative y axis. The total force F_x on the FRC then becomes

$$F_x = \int_0^{2\pi} \frac{(B_{gz} + B_{tz})^2}{2\mu_o} \mathrm{L}_{\mathrm{frc}} r_{frc} \sin\theta d\theta \qquad [5.3]$$

On the surface of the cylindrical FRC B_{tz} should be zero on the y axis of the experiment ($\theta=0$) and should be at its maximum at the x axis ($\theta=90$). For simplicity $B_{tz}(z,r,\theta)$ is assumed to be $B_{tzmax}(z,r)\sin\theta$, where B_{tzmax} is the maximum magnitude of the transverse field component acting on the FRC at $\theta=90$ at a z = constant plane. Equation [5.3] can then be written as

$$F_x = \int_0^{2\pi} \frac{(B_{gz} + B_{tz\max} \sin\theta)^2}{2\mu_o} \mathrm{L}_{\mathrm{frc}} r_{frc} \sin\theta d\theta \qquad [5.4]$$

which can be analytically solved to yield

$$F_x = 2\pi \frac{B_{gz} B_{tz\max}}{2\mu_o} L_{frc} r_{frc}. \qquad [5.5]$$

Equation [5.2] then can be rewritten as

$$F\Delta t = \int_0^{L_{tf}} F_x \frac{dz}{U_{frc}} = \int_0^{L_{tf}} 2\pi \frac{B_{gz} B_{tz\max}}{2\mu_o} L_{frc} r_{frc} \frac{dz}{U_{frc}} = 2\pi r_{frc} \frac{L_{frc}}{U_{frc}} \int_0^{L_{tf}} \frac{B_{gz} B_{tz\max}}{2\mu_o} dz \qquad [5.6]$$

If we approximate the transverse field as a simple curved magnetic field the B_{tzmax} component of the magnetic field can be found from geometry. This approximation will underestimate the actual B_{tzmax} of the field created by the two rectangular magnets, but allows a model to be examined that evaluates the effects of the transverse magnetic field and guide field scale lengths on the

impulse imparted to the FRC. From geometry $B_{tzmax} = B_t \sin\phi$, where $\phi = \tan^{-1}(r_{frc}/z)$ and z is the distance from the magnetic axis of the transverse field. When r_{frc} is much smaller than z (as is usual) the small angle approximation can be used for ϕ that $\sin\phi = \tan\phi = r_{frc}/z$ leading to $B_{gz}B_{tzmax} = B_{gz}B_t\, r_{frc}/z$. The region of interest of the sideways field gradient runs from 1/3 L_{Tf} to L_{Tf}, and r_{frc}/z varies inversely from 3 r_{frc}/L_{Tf} to r_{frc}/L_{Tf} with an average value of $\langle r_{frc}/z \rangle = 1.65\, r_{frc}/L_{Tf}$. This leads to $B_{gz}B_{tzmax} = 1.65\, B_{gz}B_T\, r_{frc}/L_{Tf}$ and the final result

$$\Delta v = \frac{3.3\pi}{M} r_{frc}^2 L_{frc} \frac{1}{L_{Tf}} \frac{1}{U_{frc}} \int_0^{L_{Tf}} \frac{B_{gz} B_t}{2\mu_0} dz \qquad [5.7]$$

The magnitude of the transverse field B_t can be roughly approximated as the linear function $B_t = B_{tmax}\,(1\text{-}z/L_{Tf})$, as shown next. z=0 is the back of the transverse field chamber, $z=1/3L_{Tf}$ is the center of the chamber, $z=2/3L_{Tf}$ is the entrance to the chamber, and $z=L_{Tf}$ is the point in the guide field at which the magnitude of the transverse field becomes negligible. a is the radius of the solenoidal field coils.

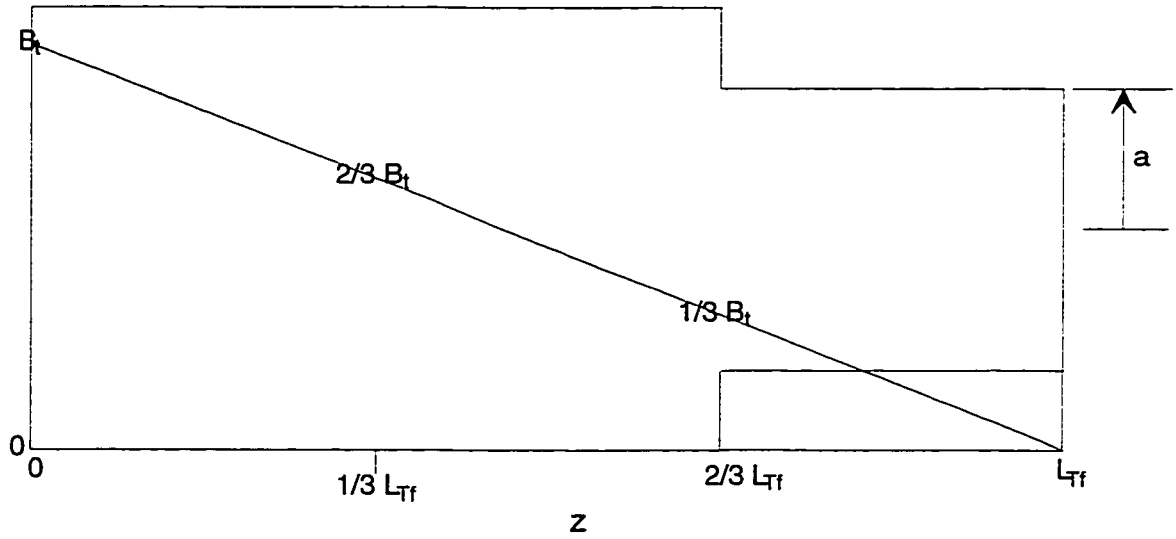

The z component of the guide field B_{gz} can be approximated as a constant B_{gmax} for $z>2/3\ L_{Tf}$. For $z < 2/3\ L_{Tf}$, the B_{gz} field can be approximated in

one of two ways. Either as the decaying field from a current ring located at $z=2/3L_{Tf}$:

$$B_{gz} = B_{g_{max}} \frac{a^3}{\left(a^2 + \left(z - \frac{2}{3}L_{Tf}\right)^2\right)^{3/2}} \qquad [5.8]$$

or as a field that linearly decays from the peak field magnitude of the solenoidal field to zero over a scale length of 2a.

$$B_{gz} = B_{g_{max}} \frac{z - 2/3\, L_{Tf}}{2a} + 1 \qquad [5.9]$$

The integral $\int_0^{L_{Tf}} \frac{B_{gz} B_t}{2\mu_0} dz$ then becomes

$$\int_0^{L_{Tf}} \frac{B_{gz} B_t}{2\mu_0} dz = \frac{1}{2\mu_0} \int_{2/3 L_{Tf}}^{L_{Tf}} \left(1 - \frac{z}{L_{Tf}}\right) B_{t_{max}} B_{g_{max}} dz +$$

$$\frac{1}{2\mu_0} \int_0^{2/3 L_{Tf}} \left(1 - \frac{z}{L_{Tf}}\right) \frac{\left(\frac{a}{L_{Tf}}\right)^3}{\left(\left(\frac{a}{L_{Tf}}\right)^2 + \left(\frac{z}{L_{Tf}} - \frac{2}{3}\right)^2\right)^{3/2}} B_{t_{max}} B_{g_{max}} dz \text{ or}$$

$$\frac{1}{2\mu_0} \int_{2/3 L_{Tf} - 2a}^{2/3 L_{Tf}} \left(1 - \frac{z}{L_{Tf}}\right) \left(\frac{z - 2/3\, L_{Tf}}{2a} + 1\right) B_{t_{max}} B_{g_{max}} dz \qquad [5.10]$$

The first part of the integral can be easily solved for to yield $\frac{1}{2\mu_0} \int_{2/3 L_{Tf}}^{L_{Tf}} \left(1 - \frac{z}{L_{Tf}}\right) B_{t_{max}} B_{g_{max}} dz = \frac{L_{Tf}}{2\mu_0} B_{t_{max}} B_{g_{max}} \frac{1}{18}$. The second part of the integral must be numerically solved for the current ring case. An approximate numerical solution yields:

$$\frac{1}{2\mu_0}\int_0^{\frac{2}{3}L_{Tf}}\left(1-\frac{z}{L_{Tf}}\right)\frac{\left(\frac{a}{L_{Tf}}\right)^3}{\left(\left(\frac{a}{L_{Tf}}\right)^2+\left(\frac{z}{L_{Tf}}-\frac{2}{3}\right)^2\right)^{\frac{3}{2}}}B_{t_{max}}B_{g_{max}}dz =$$

$$\frac{L_{Tf}}{2\mu_0}B_{t_{max}}B_{g_{max}}\frac{1}{2}\left[\left(\frac{a}{L_{Tf}}\right)-3\left(\frac{a}{L_{Tf}}\right)^2+18\left(\frac{a}{L_{Tf}}\right)^3\right] \qquad [5.11]$$

For the linear decaying field, the second part of the integral can be analytically solved to yield

$$\frac{1}{2\mu_0}\int_{\frac{2}{3}L_{Tf}-2a}^{\frac{2}{3}L_{Tf}}\left(1-\frac{z}{L_{Tf}}\right)\left(\frac{z-\frac{2}{3}L_{Tf}}{2a}+1\right)B_{t_{max}}B_{g_{max}}dz =$$

$$\frac{L_{Tf}}{2\mu_0}B_{t_{max}}B_{g_{max}}\frac{1}{3}\left[\left(\frac{a}{L_{Tf}}\right)\left(1+2\frac{a}{L_{Tf}}\right)\right] \qquad [5.12]$$

The total imparted velocity then becomes

$$\Delta v = \frac{3.3\pi}{M}r_{frc}^2L_{frc}\frac{1}{L_{Tf}}\frac{1}{U_{frc}}\int_0^{L_{Tf}}\frac{B_{g_z}B_t}{2\mu_0}dz =$$

$$\frac{3.3\pi}{M}r_{frc}^2L_{frc}\frac{1}{L_{Tif}}\frac{1}{U_{frc}}\frac{L_{Tf}}{2\mu_0}B_{t_{max}}B_{g_{max}}\left(\frac{1}{18}+\left[either\frac{1}{2}\left(\left(\frac{a}{L_{Tf}}\right)-3\left(\frac{a}{L_{Tf}}\right)^2+18\left(\frac{a}{L_{Tf}}\right)^3\right)or\right.\right.$$

$$\left.\left.\frac{1}{3}\left(\frac{a}{L_{Tf}}\right)\left(1+2\frac{a}{L_{Tf}}\right)\right]\right) \qquad [5.13]$$

Using $M=mn_{frc}\pi r_{frc}^2L_{frc}$ this can be rewritten as

$$\Delta v = \frac{3.3}{mn_{frc}}\frac{1}{U_{frc}}\frac{B_{t_{max}}B_{g_{max}}}{2\mu_0}\left(\frac{1}{18}+\left[either\frac{1}{2}\left(\left(\frac{a}{L_{Tf}}\right)-3\left(\frac{a}{L_{Tf}}\right)^2+18\left(\frac{a}{L_{Tf}}\right)^3\right)or\right.\right.$$

$$\left.\left.\frac{1}{3}\left(\frac{a}{L_{Tf}}\right)\left(1+2\frac{a}{L_{Tf}}\right)\right]\right) \qquad [5.14]$$

The experiment operated with a/L_{Tf} ~1/8. The numerical field models were used to verify this simple analysis and to analyze the trajectory. Again, the basic equation used in the analysis the FRC trajectory was

$$\Delta v = \frac{1}{M}\int_0^{L_{Tf}} F_x \frac{dz}{U_{frc}}$$

The integral was numerically calculated based on previous field calculations and found to be

$$\int_0^{L_{Tf}} F_x \frac{dz}{U_{frc}} = 1.14\times10^6 r_{frc}^2(m)\frac{L_{frc}(m)}{U_{frc}(m/s)} B_{g_{max}}(T) B_{t_{Max}}(T) \quad \text{(kg m/s)} \qquad [5.15]$$

The results from the simple analysis yield

$$3.3\pi r_{frc}^2 L_{frc}\frac{1}{L_{Tf}}\frac{1}{U_{frc}}\int_0^{L_{Tf}}\frac{B_{gz}B_t}{2\mu_0}dz = 3.3\pi r_{frc}^2 L_{frc}\frac{1}{U_{frc}}\frac{B_{g_{max}}B_{t_{Max}}}{2\mu_0}(0.1122) =$$

$$0.463\times10^6 r_{frc}^2(m)\frac{L_{frc}(m)}{U_{frc}(m/s)} B_{g_{max}}(T) B_{t_{Max}}(T) \text{ (kg m/s)} \qquad [5.16]$$

for the exponentially decaying solenoidal ring case, and

$$3.3\pi r_{frc}^2 L_{frc}\frac{1}{L_{Tf}}\frac{1}{U_{frc}}\int_0^{L_{Tf}}\frac{B_{gz}B_t}{2\mu_0}dz = 3.3\pi r_{frc}^2 L_{frc}\frac{1}{U_{frc}}\frac{B_{g_{max}}B_{t_{Max}}}{2\mu_0}(0.1076) =$$

$$0.444\times10^6 r_{frc}^2(m)\frac{L_{frc}(m)}{U_{frc}(m/s)} B_{g_{max}}(T) B_{t_{Max}}(T) \text{ (kg m/s)} \qquad [5.17]$$

for the linear decaying guide field.

The results of the simple analysis are approximately 2.5 times lower than the numeric calculations. This error arises from the assumption that $B_{tzmax} = B_t \sin\phi$, where $\phi = \text{Tan}^{-1}(r_{frc}/z)$ and z is the distance from the magnetic center of the field. While this is valid for a transverse or toroidal field generated from a line current at the magnetic center of the field, it is not valid for conditions used on the TRAP experiment. The transverse field in the TRAP experiment was generated using a set of two rectangular Hemheoltz-like quasi-steady magnets

arranged in a 'pie-piece' or 'V' geometry. The field generated by the magnets is significantly different than the field that would be generated by a single line current and greatly increase the magnitude of the sideways field gradient.

To examine the plasma trajectory, the visible light tomographic imaging arrays and the thermocouple probes were installed. While the experiment was non-operational for installation of new diagnostics, the transverse field was again calibrated along the Z axis with the internal B probe. Results were the same. When the experiment was again operational, the bulk of the data used to analyze the FRC injection into the transverse field was collected.

5.4 Data Collection and recording

Experimental data traveled through either fiber optics or coaxial cables to shielded Hoffman boxes and then to the screen room to a CAMAC based data acquisition system. The setting of fast timing pulses and data acquisition equipment was automated. Experimental parameters were input from PC's in a control room, and then programmable logic controllers executed the experiment automatically. Fast trigger timing and data acquisition specifications were displayed on the same PC's, which were on a local area network (LAN) with a MicroVAX computer running the MDS module addressing and data-base system. The fast timing generators and transient digitizers were located in a screen room, which communicated with the control room using fiber optics.

The entire system was run by one technician and one scientist, although several scientists and students monitored individual instruments using individual PC's on the LAN. The MicroVAX can also be addressed, and data viewed at the University of Washington. About 200 transient digitizer channels, with 10 to 20 MHz digitizing rates, were used on the entire experiment.

Chapter 6

Diagnostics

6.1 Magnetic pickup probes

Two groups of magnetic pick-up probes were used on the TRAP experiment. The first group used was an array of small triple axis probes wound around prefabricated polyurethane forms encased in quartz tubing used to look at the magnetic perturbation of the transverse field exterior to the FRC. These probes were similar to those used by G.C. Spanjers[12], and were calibrated using the same equipment and technique as specified by him. The probes were encased in quartz tubing and the arrays entered the vacuum interaction chamber from the bottom as shown in Figure 24. through sliding double O-ring seal vacuum interfaces. Four triple axis probes were employed in a linear array.

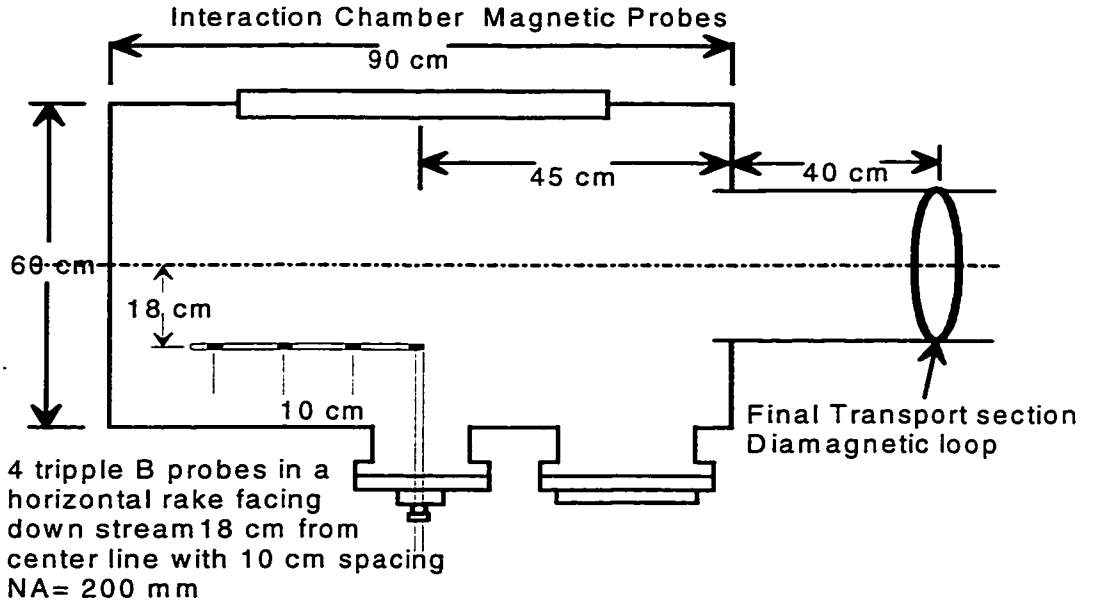

Figure 24. External B probes used to measure field perturbations of the Transverse field.

These 'external' magnetic field pick-up probes were located at z = 0, 10, 20, 30 cm, approximately 18 cm below the expected line of trajectory of the FRC. This array was used to measure changes in the magnetic field at four points in a line perpendicular to the interaction chamber field, but parallel to the experimental axis. The magnetic probe data from the array was used to look at the field perturbations caused by the penetrating plasma and was compared to calculations based on a flux excluding plasma.

The second set of magnetic pick-up probes was an array of eight single axis probes with approximately 30 turns wound around a 50 mil fiber optic cable at ten cm spacing. The array was sheathed in a 3mm O.D. by 2mm I.D. sealed quartz tube. The array was post-experimentally calibrated using the previously cited methods. The array entered the experiment from a hole drilled in the back wall of the interaction chamber at its vertical center and was positioned to lie in the expected line of trajectory of the FRC (z axis of the experiment) with the probes aligned to measure changes in the FRC internal field along the z axis. The magnetic probe data from this array was used to look at the penetration of the accelerated plasma.

6.2 Internal Pressure sensing probes

To study the interaction of the plasma in the interaction chamber; namely the dispersion of plasma along the transverse field lines, an internal direct plasma sensing diagnostic was developed to provide meaningful quantitative data. Piezoelectric pressure probes were constructed in an attempt to meet this requirement.

A piezoelectric device operates using the property of a piezoelectric material that if a voltage is applied to the material it will exert a pressure normal to its surface, or conversely, if a pressure is applied normal to its surface it will

register a voltage. It is the later property of these materials that allows for the construction of pressure sensing probes.

In its simplest form, a pressure sensing probe simply requires some sort of piezoelectric material (hereafter referred to as a wafer) mounted on a backing in such a way as to allow the electrical potential across the faces of the wafer to be measured. One common concept used in the design of piezoelectric pressure probes (the one that was used in the TRAP experiment) is that of the pressure bar. In this design, the piezoelectric wafer is either glued to one end or sandwiched in between two ends of an acoustically conducting rod. The rods are either made of an electrically conducting media or the ends that are in contact with the wafer are dipped and coated with a thin layer of some electrically conducting material. In either case the piezoelectric wafer is glued to the end, or glued in between the ends of the acoustically conducting rod with electrically conducting glue. The electrical leads are then more easily attached to the pressure bar and the signal sent to be analyzed. The physical constraints on the design of the probe are derived from the existing experimental set up and how the probe may affect the experimental operation and results. These important design considerations led to the following.

The piezoelectric material was selected so as to produce a noticeably high voltage when the probe is impacted by the plasma. Additionally, the material directly in contact with the wafer was selected so as to match the acoustical properties of the wafer so as not to degrade the pressure pulse traveling through the medium and to avoid signal reflections.

The piezoelectric material needed to be shielded from direct contact with the plasma to prevent signal contamination from the plasma potential. The potential from the plasma is at least on the order of the expected pressure voltage signal, and contamination would render the signal meaningless. An electrically insulating sleeve was therefore employed. Additionally, an identical

probe was constructed and used without a piezoelectric wafer in order to directly measure any pick-up from the plasma potential.

The electrical leads coming from the probe were arranged so as to minimize the amount of electrical and magnetic pickup that could result in excessive noise. The electrical signal from the probe needed to exit the vacuum chamber, yet the probe face must be exposed to vacuum. An electrical vacuum feed through was required. All surfaces exposed to the vacuum were made of appropriate material so as not to introduce impurities into the chamber in the event of ablation caused by plasma bombardment. The probe was designed so as to eliminate or minimize the affect of any reflected signals interfering with the primary signal, yet still meet the above requirements.

The magnetic field the plasma was expected to penetrate through is approximately one Tesla. The corresponding magnetic field pressure is about 4 atmospheres or ~ 4 x 10^5 N /m^2. The probes were expected to see pressure pulses on this order of magnitude, so the piezoelectric material was selected with these limits in mind. These criteria lead to the selection of the Lead Zirconate-Titanate piezoelectric Ceramic Kezite K350, provided by Keramos Inc. of Indianapolis, IN.

Kezite K350 has a piezoelectric voltage constant of 25 x 10^{-3} Volt-meters/Newton; which can be rewritten as 25 x 10^{-3} (V / m) / (N / m^2). The speed of sound through the material is 3.96 mm/μs. The acquired wafer thickness is approximately 1 mm, providing for a rise time on the order of 0.25 μs. The expected voltage as a function of applied pressure can then easily be expressed as:

$$V_{wafer} = \frac{25\times10^{-3}V/m \bullet 10^{-3}m}{N/m^2} = \frac{25\times10^{-6}V}{N/m^2}. \qquad [6.1]$$

For pressures on the order of 4 x 10^5 N / m^2 the expected output voltage is 10 Volts. The digitizers with a range of -5 to 5 volts were easily be able to

accommodate these signals with some simple divide by 2 attenuation. With the wafer material selected, the components of the probe were selected so as to match the wafer's acoustical properties.

The components of the pressure bar (the acoustically conducting medium) were machined from Brass. Brass was selected because it is an electrical conductor and due to its almost exact match to the acoustical properties (speed of sound, and acoustical impedance $z=[E\rho]^{1/2}$) of the piezoelectric wafer. The electrically conducting glue used was TRA-DUCT 2902 conductive silver epoxy adhesive manufactured by TRA-CON, Inc. of Medford, Mass.

In order to minimize the affect of any electrical or magnetic pickup, and to facilitate the signal feed-through out of the vacuum chamber, initial test probes were constructed with co-axial signal leads that could easily be mounted to an isolated BNC vacuum feed-through. The brass rod backing was used as one of the signal leads, while a Teflon coated wire, attached through the brass backing rod and the wafer, to the brass rod glued to the front of the piezoelectric wafer was used as the other lead. In the final design of the pressure probe arrays, the individual probes were still constructed with co-axial signal leads, however the probes do not mount into BNC feed-throughs. The signals were brought out with twisted pairs of Teflon coated wire.

Material ablation into the vacuum chamber precluded having the wafer at the end of the pressure bar and directly in contact with the plasma. Additionally, the problem with possible signal contamination from the plasma potential required that the face of the pressure probe not be in electrical contact with the piezoelectric wafer. In en effort to minimize the introduction of impurities into the vacuum chamber and to eliminate the plasma potential pick-up problem, a clear fused quartz rod, similar in composition to the quartz tubes used in the vacuum system, was used as the tip of the probe. Of the materials available (brass, quartz, and stainless steel), the quartz proved to have the worst acoustical match to the piezoelectric wafer. However, the quartz rod was used despite

this discrepancy in order to minimize the more series problems of plasma contamination from material ablation and pick-up from the plasma potential. The remaining components of the probe casings were machined of stainless steel similar to the interaction chamber walls.

A commonly observed problem in pressure probes is signal reflection interfering with the original signal. To eliminate this problem the probe was made of sufficient length to ensure that the transmission time between the original signal and any possible reflections is much longer than the expected time scale of the signal. Knowledge of the time scale of signal event was therefore important. From simple dimensional analysis it is determined that the expected signal time can be expressed as:

$$\Delta t_{impact} \cong \frac{L_{frc}}{V_{frc}} \qquad [6.2]$$

For an FRC with a velocity V_{frc} ~ 18 cm/μs and a length of L_{frc} ~ 160 cm the expected signal time scale should be on the order or 9 μs. Probe lengths were selected to provide reflection transmission times on the order of 30 μs to 60 μs to ensure that any reflected signal does not interfere with the primary signal.

Before final design and fabrication of the probe arrays, two test probes were constructed to examine the best means of probe calibration and installation for experimental use. The finalized test probe design is shown in figure 25. The piezoelectric wafer was electrically glued between two 0.394 " Dia Brass rods machined at the end to press fit over the center conductor and into the outer sheaf of a floating ground BNC vacuum feed-through. A 1/16 " Dia. hole was carefully drilled through the brass rods and the piezoelectric wafer to allow for an electrical lead from the center conductor to the front face of the forward brass rod. The center conductor was connected to the front face of the forward brass rod with 30 gauge Teflon coated wire soldered at both ends. The press fit between the rear brass rod and the BNC outer sheaf proved to be an excellent electrical connection, and was used as the second signal lead.

Test piezoelectric pressure probe final design

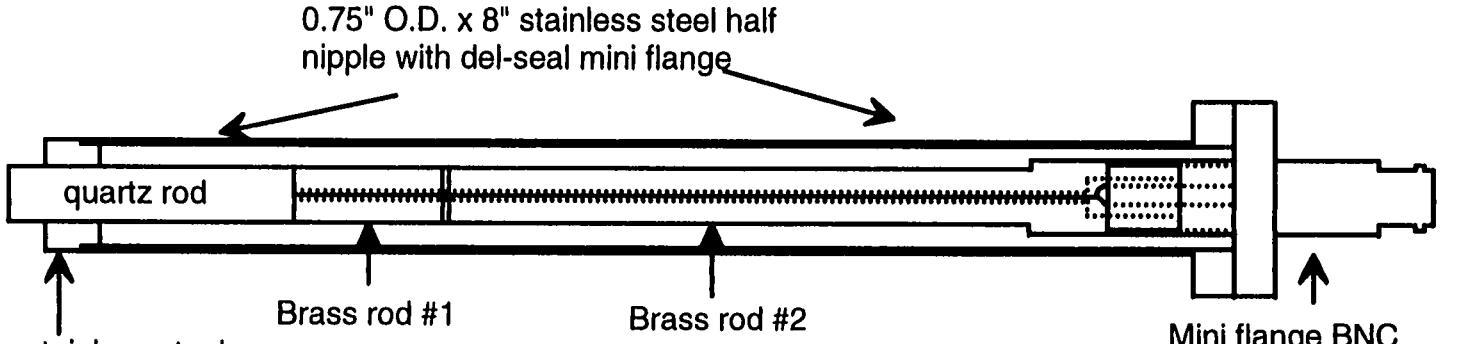

Quartz rod: 1 cm Dia, 5 cm length
Brass rod #1: 0.394 " Dia, 1.0 " length
Brass rod #2: 0.394 " Dia, 4.0 " length
with 0.625 " long, 0.5 " Dia. mount
Piezoelectric wafer: 1 cm Dia, 1 mm length
K350 Lead Zirconate Titanate Ceramic

Figure 25. Piezoelectric Test probe

The 4.0" length of the rear brass backing conducting rod was selected based upon the round trip acoustic time of brass. The speed of sound of brass is known to be 3.56 mm/μs. (Very close to the 3.96 mm/μs for the piezoelectric material.) The 4.0" brass backing has a length of ~100 mm, and a reflected signal should take ~ 57 μs to re-compress the piezoelectric wafer. Reflections do not seem to interfere with analysis of the original signal from the probe.

A 1-cm dia., 5-cm long fused clear quartz rod was glued to the forward 1" brass rod with commercially bought Krazy glue. Krazy glue provided an extremely intimate contact between the two rods which aided in decreasing the reflections caused by material mismatching. The joint did, however, seem to be extremely vulnerable to shear forces. The speed of sound through quartz is ~5.6 mm/μs. Any reflections due to material mismatching at the quartz/brass interface take ~ 17 μs to again reach the wafer and did not pose any problems in signal analysis.

A piezoelectric wafer is a charge generator where the charge Q is proportional to the applied pressure, and the voltage V = Q/C. So, for calibration purposes, the electrical characteristics of the piezoelectric pressure probes were analyzed as a simple RC circuit solving for Q. The capacitance was measured directly from the probe and the resistance used was either the 1MΩ input impedance of the viewing scope, or a 50 Ω termination. The 50Ω termination was necessary to view the signal on the scope as it would be seen in the screen room by the 50Ω terminated digitizers. The 1MΩ input impedance of the scope was closer to the natural resistance of the piezoelectric wafer and gave a more accurate representation of the applied pressure pulse, while the 50Ω terminated signal (as will be seen later) showed the differentiated pressure signal.

From simple analysis of a RC circuit (as shown below) it can be shown that the differential equation governing the charge through the circuit can be expressed as:

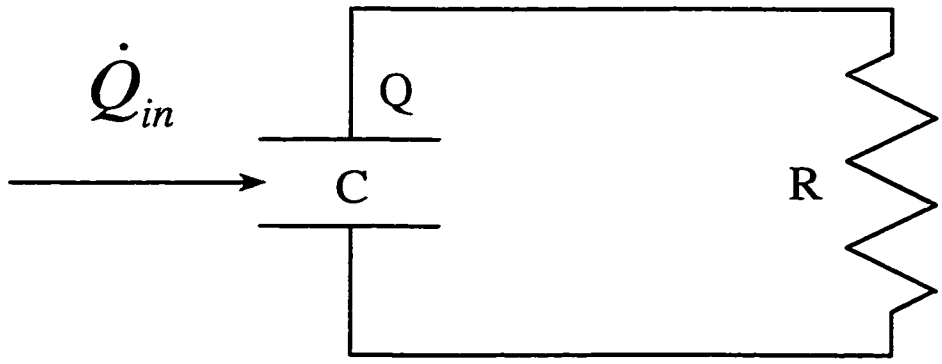

$$\frac{dQ}{dt}+\frac{Q}{RC}=\dot{Q}_{in} \qquad [6.3]$$

For an assumed sinusoidal pressure impulse $F = F_o \sin\omega t$, one can relate an assumed charge Q_{in} and dQ_{in}/dt by $Q_{in} = Q_F \sin\omega t$ and $dQ_{in}/dt = \omega Q_F \cos\omega t$ where Q_F is related to F_o by the material properties of the piezoelectric wafer, and the measured voltage is related simply by $V = Q/C$. With some mathematical manipulation this equation can be solved to yield:

$$Q = Q_F\left(\frac{\omega\tau}{1+(\omega\tau)^2}\left[\cos(\omega\tau)-e^{-1/\tau}\right]+\frac{(\omega\tau)^2}{1+(\omega\tau)^2}\sin(\omega\tau)\right) \qquad [6.4]$$

Where $\tau = RC$. This solution can be further simplified for either very high or for low impedance systems where $\omega\tau$ is either very large or very small and one of the terms of the solution can be ignored.

For large impedance measurements ($R=1M\Omega$) when $\omega\tau$ is large the solution simplifies to $Q = Q_F \sin\omega t$ and represents the natural signal as seen by the probe. For low impedance measurements ($R=50\Omega$) the solution reduces to $Q = Q_F(\omega\tau)\cos\omega t$ and represents a differentiated signal as seen by the probe.

The 1 cm dia. test probes were calibrated using a ballistic pendulum with the probe signal sent to a scope with either a 50Ω or 1MΩ termination as shown in figure 26. A 1mg mass was dropped from a height h_1 of 8.1 cm and its return bounce height h_2 was recorded at approximately 4 cm.

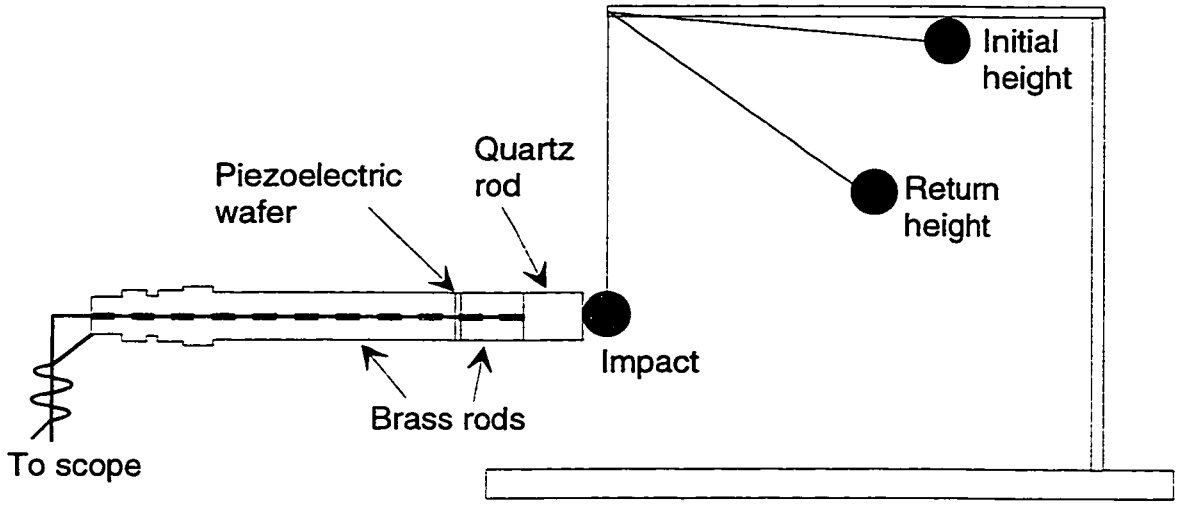

Figure 26. Calibration of pressure probes using ballistic pendulum

The imparted pressure pulse $\int pdt = \frac{m\sqrt{2g}\left(\sqrt{h_1}+\sqrt{h_2}\right)}{A_{impact}}$ was calculated to be 27.4 $\mathrm{kg}\frac{\mathrm{m/s}}{\mathrm{m}^2}$. The scope signal in figure 27 from the probe with 1 MΩ termination was integrated and the total signal magnitude was calculated to be ~ 720 x 10^{-6} volt sec. Integrating the 1 MΩ terminated signal was required to relate the Voltage(pressure) vs time trace to a total imparted impulse. The calibration constant relating voltage to pressure was calculated by dividing the magnitude of the integrated signal by the above imparted impulse and was found to be 26.3x10^{-6} Vm^2/N. The calculated calibration constant for a 1 mm thick wafer was very close to the 25.0 x10^{-3} Vm/N voltage constant specified in the material properties provided by the manufacturer.

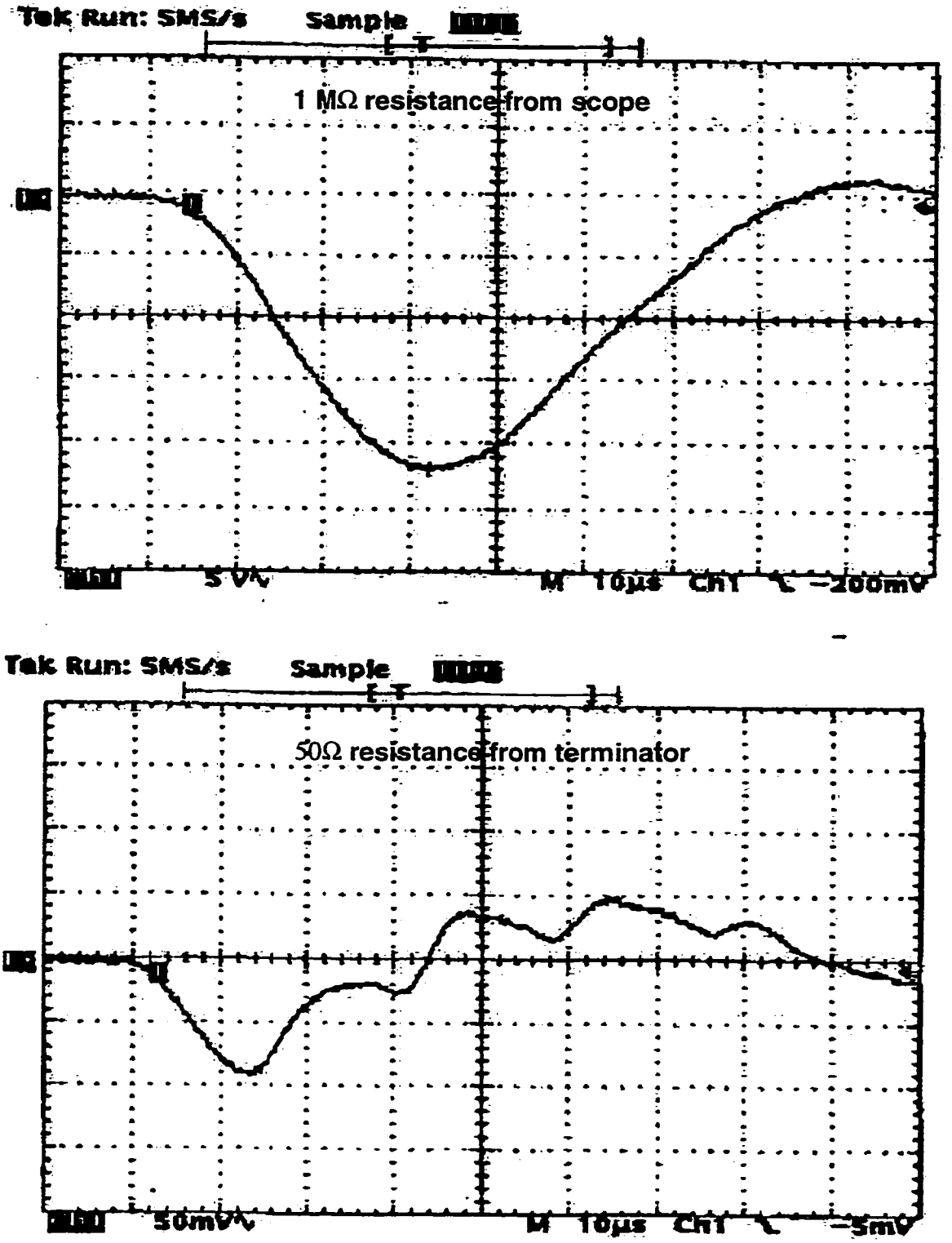

Figure 27. Pressure probe calibration traces

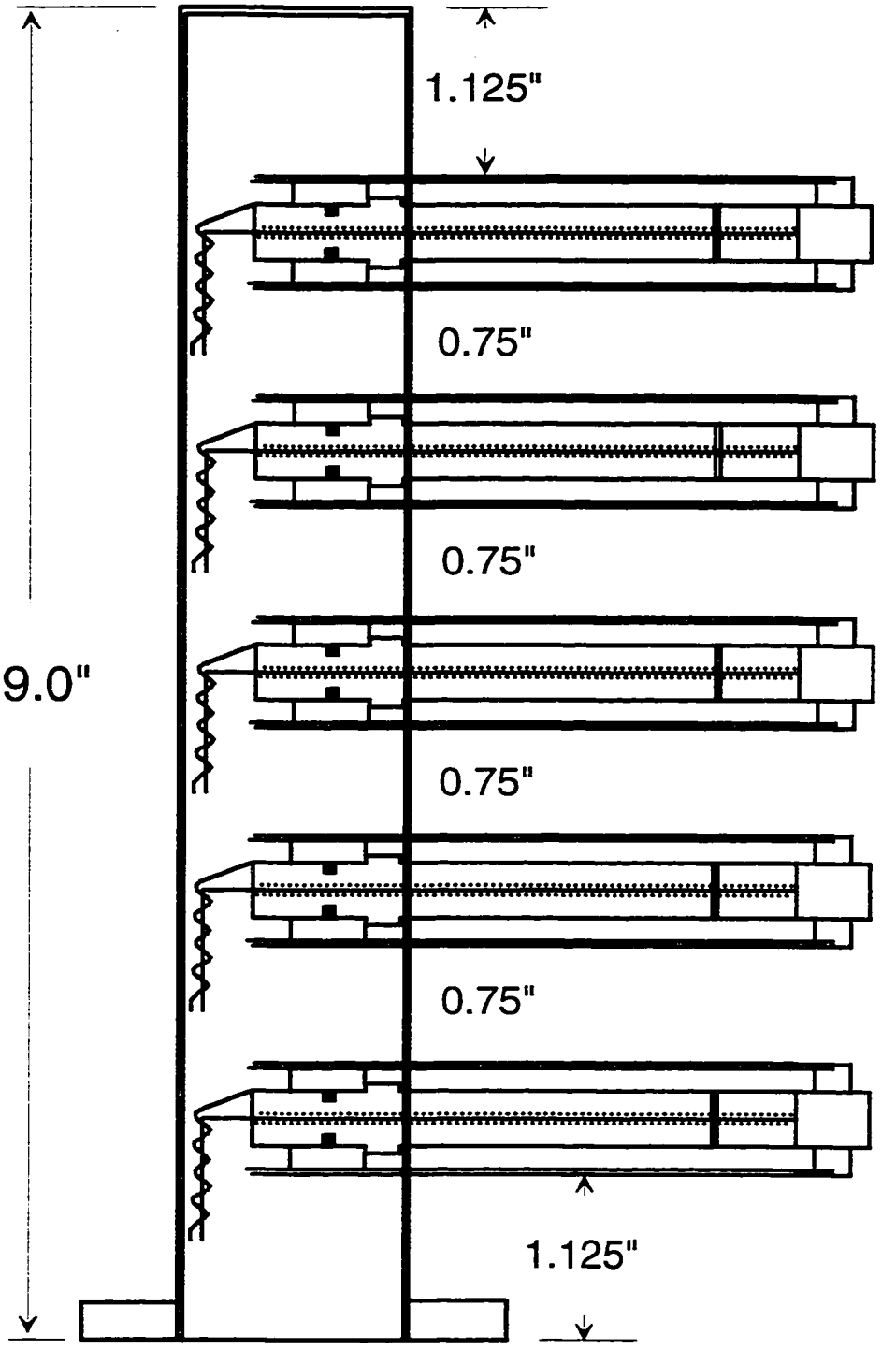

Figure 28. Pressure probe array design

The 50Ω terminated differential signal in figure 27 was integrated and compared to the 1 MΩ terminated signal and found to yield approximately the same calibration results.

The final design for the pressure probe arrays is shown in figure 28. The array consisted of five probes centered in a 9" vacuum half nipple. The center probe on the arrays was constructed without a piezoelectric waver, and acted as a dummy probe that only measured the plasma potential locally. Two such arrays were constructed, but only one was used. The array entered the interaction chamber through the top flange in the eastern port at 90 degrees from the transport tube entrance. The locations are shown in Figure 15. During experimental operation the high impedance signals from the array were processed through multi-channel 50Ω line drivers with 0.2 amplification before traveling to the screen room. The signal was then numerically integrated and calibrated during data storage. The final calibration for the imparted pressure pulses was 2.62×10^{-5} V/(N/m^2).

6.3 Visible light imaging cameras and emission arrays

In order to visually observe the interaction of the FRC in the transverse field chamber two high speed imaging cameras were employed. The Visible light imaging cameras were Imacon 790 sub μsec exposure time, multi-frame grabbing cameras, with high and low pass filters to filter out the D_α and D_β lines. One Imacon camera viewed the plasma in the interaction chamber through the large central port in the top flange of the chamber, while another viewed the plasma from the source end of the experiment through a window in the vacuum tank. Multiple images were formed on a single phosphor screen and the images are then recorded on film. Quartz tubes arranged in a cross hair near the throat of the entrance region (as described earlier) were used to aid in visualization.

The end on visible light imaging camera (as seen previously in figure 20) allowed the plasma to be observed during formation, acceleration, translation, and initial injection. Relative to the picture, right is East, left is West, and up and down are up and down. The camera produced an eight frame Polaroid picture of the plasma. The frames start in the lower left corner of the picture at 35 μsec and proceed up and to the right at 5 μsec increments. Each frame has an exposure time of approximately 1 μsec. The imaging camera was used to observe the gross trajectory of the FRC as it traversed the formation, acceleration and translation sections of the experiment as well as observe the FRC position in the translation tube as it initially penetrates into the transverse field. The pictures allowed for the observation of any formation problems or wall contact by the FRC as it traversed the experiment prior to the interaction chamber.

The interaction chamber imaging camera allowed for the observation of the plasma during penetration into the interaction chamber. The camera produced a ten frame Polaroid picture of the plasma from above reflected off a mirror. Relative to pictures shown in figure 29, right is upstream toward the formation section, left is downstream, up is West, and down is East. The frames start in the lower left corner of the picture at 45 μsec and proceed up and to the right at 2 μsec increments. Each frame has an exposure time of approximately 0.4 μsec. The camera was used to observe the gross trajectory and penetration depth of the FRC in the transverse field interaction chamber. The pictures also provided insight into plasma deposition from light-up by plasma-wall contact in the interaction chamber. In the figure 29 example we see the plasma first making contact with the quartz 'cross-hair' tubes at t = 49 μsec. The bright spot is the vertical (y axis) tube, and the line is the horizontal (x axis) tube. At t = 51 μsec we see that the majority of the light up on the horizontal tube is above the center of the image. This indicates that the FRC was pushed west during injection due to the field gradient a the throat of the chamber.

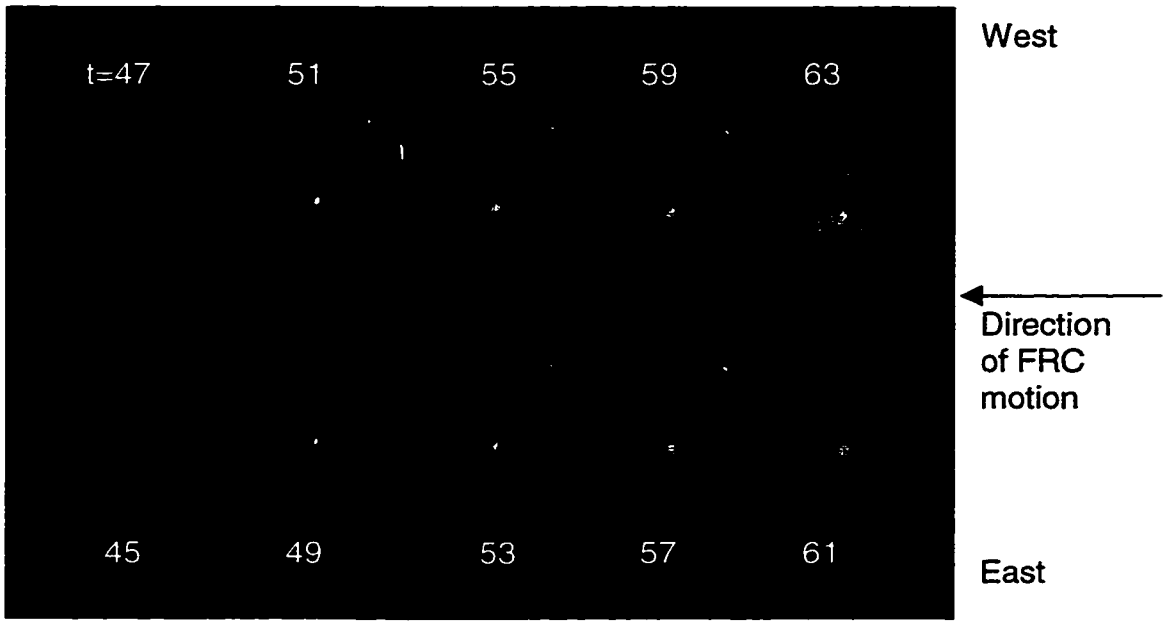

Figure 29. Interaction Chamber Imacon Picture view from above. All times in μsec. B_t = 0.25 Tesla at back of interaction chamber.

The penetration and deformation of the FRC in the transverse field was also observed by visible light emission arrays used to record and tomographically image the plasma in the transverse field chamber. The arrangement at z=0 is sketched in figure 30. A single visible light emission array was positioned along the axial direction ($\int \varepsilon (z_i, x=0) dy$) to monitor the penetration of the FRC into the transverse field. Additional emission arrays were positioned to view the FRC both up/down ($\int \varepsilon (y_i, z=0) dx$), and side to side ($\int \varepsilon (x_i, z=0) dy$) as it passed midway through the transverse field chamber. These arrays were then used to tomographically image the FRC by using a least squares fit of the emission data to the functional values expected from an arbitrary sized and centered ellipse. The emissions ε from previous studies were found to be proportional to n^2, allowing these diagnostics to be quite useful in tracking the FRC mass density while discriminating against low density background plasma.

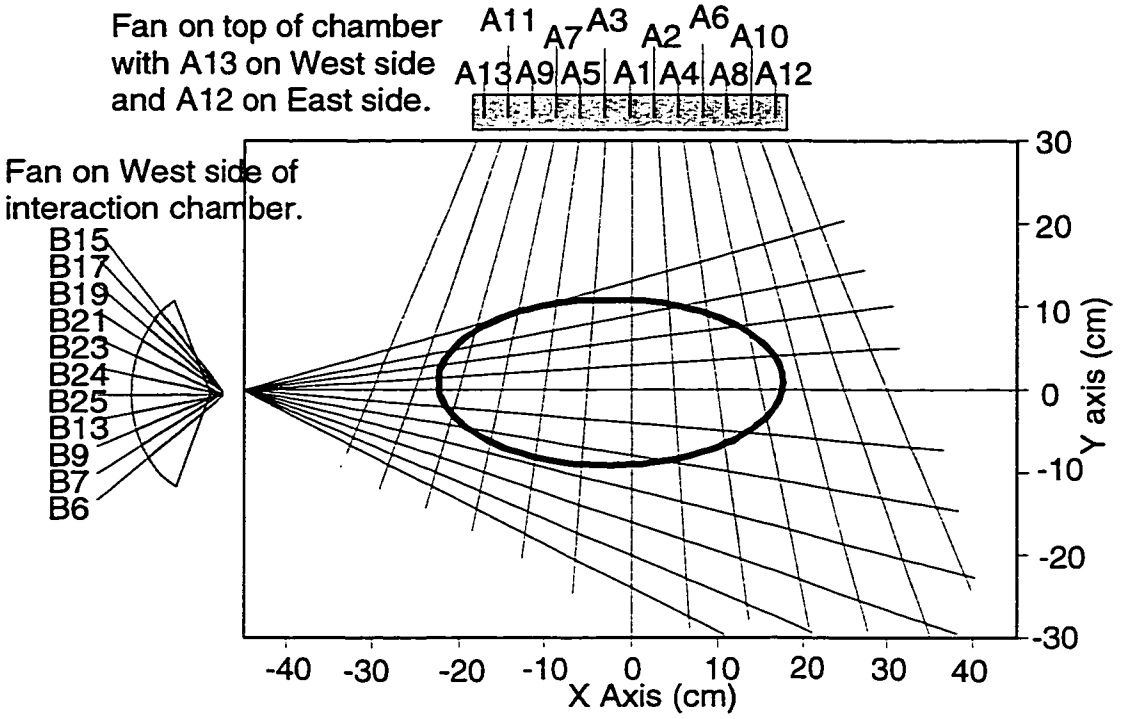

Figure 30. Tomographic fitting of emission array data.

6.4 Thermocouple probes

The thermocouple probes were 5 mil naked thermocouples inserted into 2mm x 1mm quartz tubes used to measure the power flux onto the quartz from the plasma's internal and translational energies. The power flux is related to the plasma kinetic energy ρU^2, density n, thermal velocity $v_t = \sqrt{\frac{8kT}{\pi \cdot m_i}}$ and thermal energy kT. The local power flux and the time of contact gave the localized total energy deposition to the quartz tube. Localized sputtering and ablation is observed, but was followed by material redeposition. Multiple materials were tested for use as the thermocouple sheath, with the probe temperatures shown below in figure 31, using the following method.

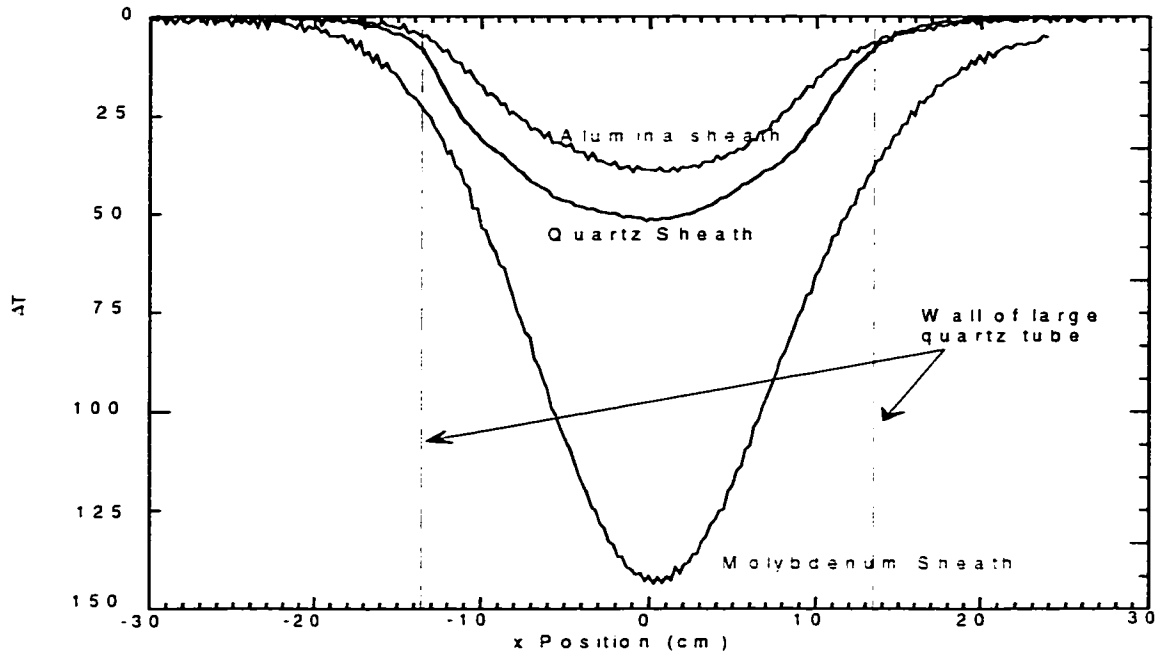

Figure 31. Comparison of thermocouple sheath materials. FRCs translated over thermocouple at joint between acceleration and guide field regions.

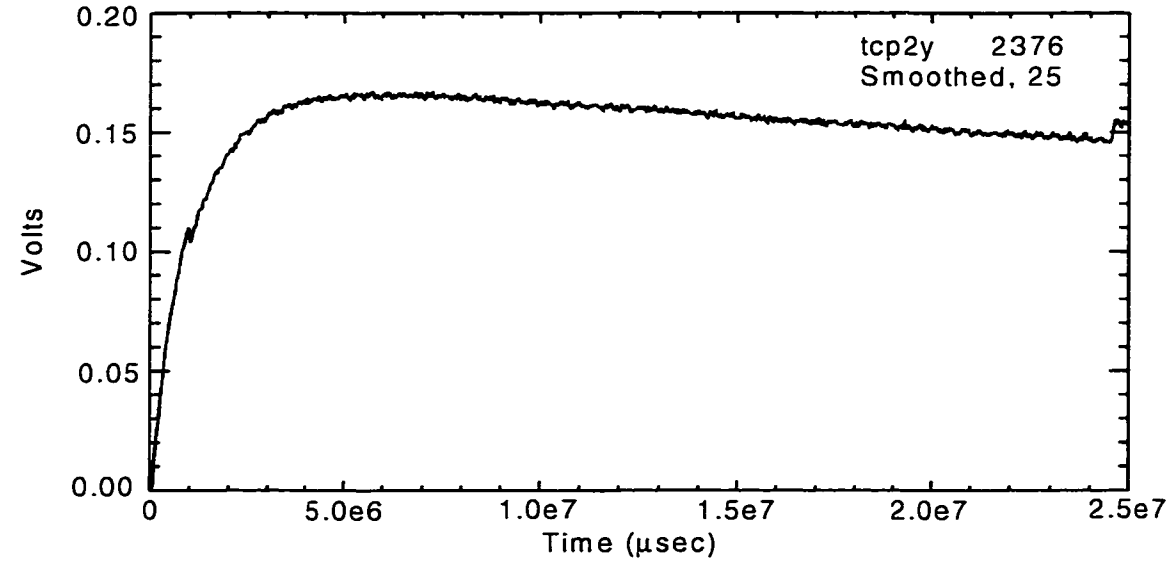

Figure 32. Stationary thermocouple trace. Trace used to experimentally determine the radiative cooling time constant of the quartz tube.

For the figure 31 calibration runs, the thermocouple was positioned at the joint between the acceleration and guide field regions. The material properties of most interest were the specific heat c (J/g°K) and thermal conductivity K (W/cm°K). The Molybdenum tube had a much lower specific heat than the Alumina and quartz tubes and therefore reached a higher temperature than the other tubes. The Molybdenum tube also had a much higher thermal conductivity which would account for more spreading of the temperature along the tube and the wider recorded signal. Visual inspection of the quartz tube indicated that minimal ablation occurred followed by immediate redeposition. Material ablation did not create any analysis problems as the tubes never reached any saturation temperature that would be indicated by a flat line saturated signal on the thermocouple probe. Quartz was selected due to its relatively high heat capacity and extremely low thermal conductivity. Quartz was also the least expensive, most readily available sheath material, with the least potential for vacuum contamination.

An example of the response of a stationary probe inside one of the quartz tubes after it had been struck by the plasma is shown in figure 32. The signal is used to analyze the probe response time and the radiative decay rate of the quartz tube in the following manner. The quartz tubing rapidly comes to local thermal equilibrium at a new temperature determined by its material properties and the local total energy deposition. The time required to reach the new equilibrium temperature is easily solved for using the 1-D heat equation: $\frac{\partial \cdot T}{\partial \cdot t} = \frac{K}{\rho \cdot c}\frac{\partial^2 T}{\partial \cdot x^2}$. For quartz K = 0.02 W/cm°K, c = 0.74 J/g°K, and ρ = 2.6 g/cm^3. For a δ = 1 mm thick wall, the temperature will bleed through and come to a new equilibrium in $t \sim \frac{\delta^2}{(K/\rho c)} = 1$ sec.

Using the signal shown in figure 32, the thermocouples were experimentally determined to come to radiative equilibrium with the inside of the quartz tube about 2-3 sec after the tube came to its new equilibrium temperature. It was additionally verified from this signal that the radiative cooling of the quartz tube proceeds on a much slower time-scale than that required for the thermocouples to reach radiative equilibrium with their local surroundings. Assuming radiative cooling only $\frac{dT}{dt} \approx T^4$ it can be easily shown that $\frac{T}{T_0} = \frac{1}{(\kappa \cdot t + 1)^{1/3}}$ where κ is a constant that was experimentally determined, using figure 32, to be 0.021/sec. Using this time constant, the time required for the temperature profile to radiatively cool to one half its original value is approximately 330 sec.

Immediately after the experiment was fired, the thermocouples sample the temperature at 500 Hz and were mechanically pulled through the quartz tubes at approximately 3 cm/sec for 20 to 30 sec to produce temperature profiles. These temperature profiles were then used to infer a local plasma flux. This diagnostic has proven to be the most effective at providing data that describes the internal density profile of the FRC and was also extremely useful in analyzing the trajectory of the FRC.

Typical results from a plasma shot (# 2376) with the interaction magnetic field energized to 2.5 kV and pointing East are shown in figure 33.

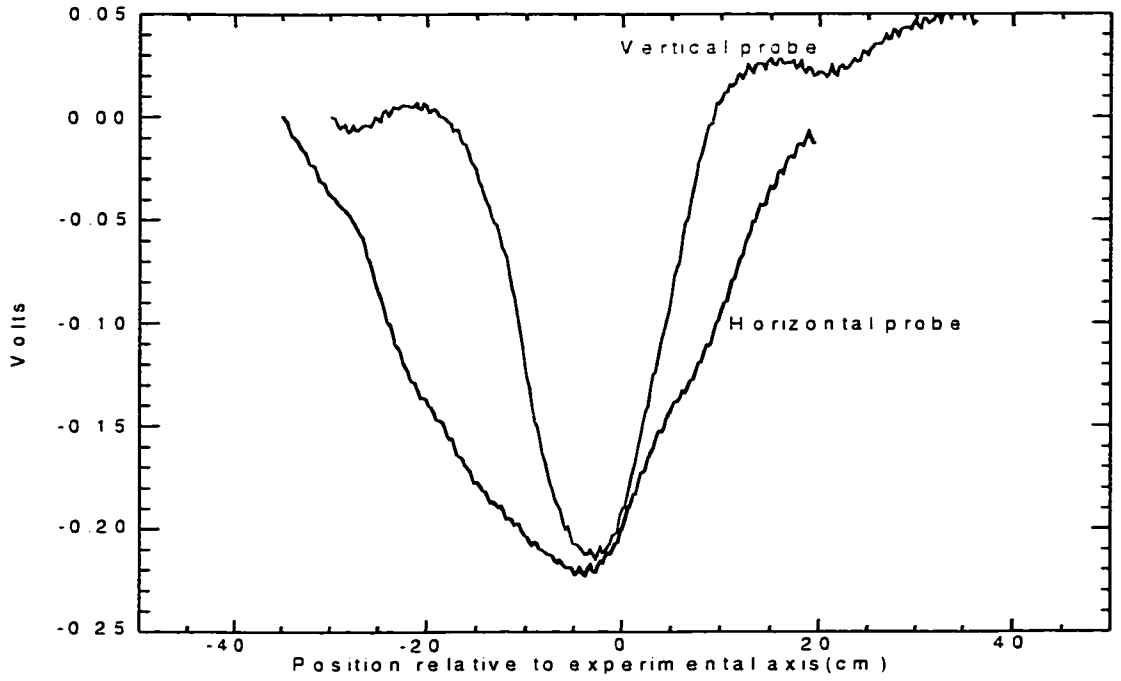

Figure 33. Typical thermocouple probe results

The horizontal probe was swept from west to east after the experiment was fired, while the vertical probe was swept from the bottom of the interaction chamber to the top. For a perfectly centered FRC, the center of the horizontal probe signal should be at 0 cm and the center of the vertical probe signal should be at 0 cm. This shot shows the horizontal probe signal centered at ~ -3 cm indicating that the plasma was slightly left of center, consistent with theory and the other diagnostics. The vertical probe signal was centered at ~-2 cm indicating that the plasma was mostly centered but might have been coming in slightly low. Another important feature of the signals is the signal width. The horizontal probe signal is much wider than the vertical probe signal indicating that the plasma is wider horizontally than vertically, which confirms our rough expectations of how the plasma should deform as it penetrates into a transverse field.

Chapter 7

Experimental Results

The movement of the FRC during formation, acceleration and translation was primarily observed using diamagnetic loops. Results from these loops are shown in figure 34 and were used to bench-mark the timing of the FRC throughout the experiment.

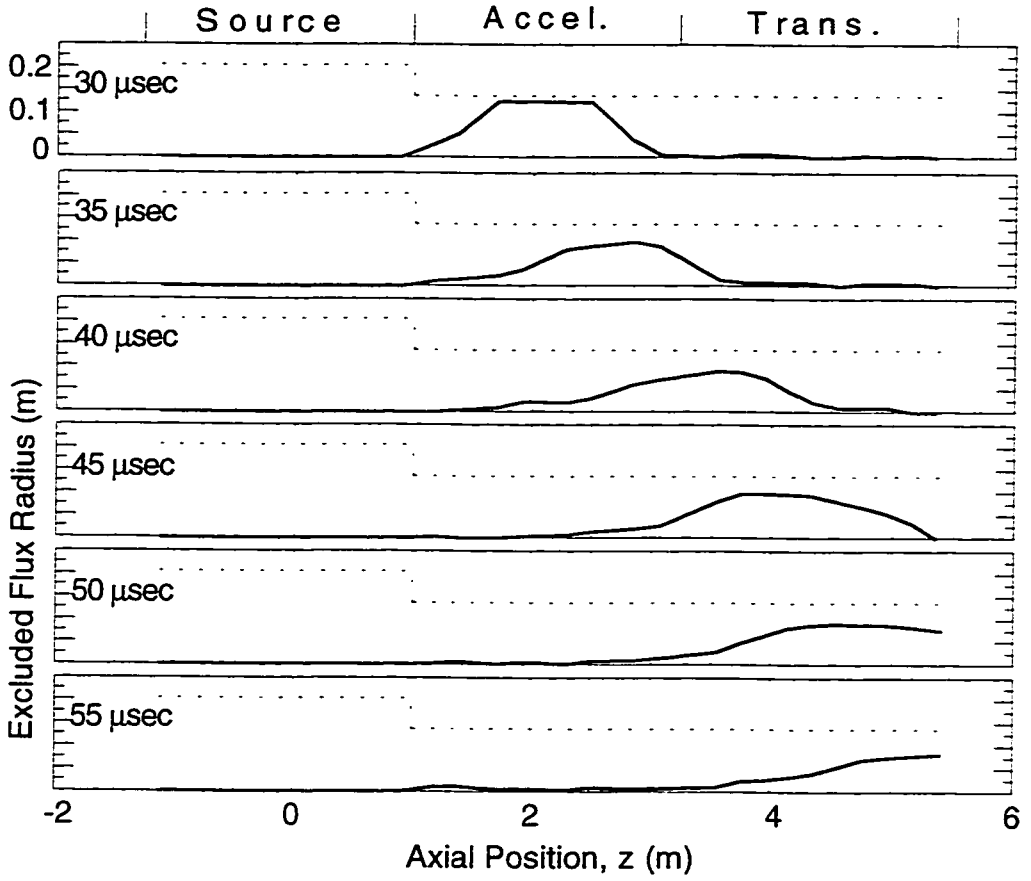

Figure 34. Timings based on excluded flux radius for a typical 20 mTorr shot. Final velocity ~200 km/s.

The throat to the transverse field chamber was located approximately 5.5 m downstream of the center of the formation chamber. The front of the FRC first began to enter the transverse field chamber at ~ 45 μsec. By 50 μsec, the main body of the FRC had penetrated, and by 55 μsec the FRC was almost completely injected into the transverse field chamber. All FRC's were formed at 20 mtorr and had a final velocity of ~ 16-20 cm/μsec.

7.1 FRC deflection

The FRC deflection was first observed in the Imacon pictures as seen in figures 20 and 29. Figure 20 clearly shows a bright crescent on the left side of the guide field tube wall at t=45 μsec, when the plasma is beginning to enter the transverse field chamber, indicating that the plasma has made contact with the tube wall. The frame at t=50 μsec shows ablation light from plasma passing over the quartz tube cross-hairs, where it clearly can be seen to be significantly shifted left of center. This shift continues to be observed in subsequent frames and is also observed in the Imacon camera pictures from above. Figure 29 shows the same shift to the left (up relative to picture) of the plasma in the frame at t=49 μsec and all frames afterward.

Additional evidence of the plasma deflection was obtained from a visible inspection of the pressure probe arrays upon removal from the experiment. While only one probe array was actively monitored during experimental operation, both arrays were mounted in the transverse field chamber during much of the experiment. The majority of the experimental shots were conducted with the transverse field directed to the east, and the expected deflection of the FRC would be to the west. Upon removal of the pressure probe arrays, the west array was observed to be significantly more discolored than its counter. This discoloration was due to heat loading and possibly to deposition of silicon contaminates entrained from the quartz tubes used as the cross-hairs.

Results from plasma shot # 2376 with the interaction magnetic field energized to 2.5 kV and pointing East are shown in figure 35. The scrape off layer of the plasma was expected to follow the field lines and flow off in the direction of the transverse field. This was observed and verified from pressure probe signals on the array arriving earlier than the main signal, while the main signal from the bulk of the plasma occurred after the FRC had reflected off the back wall. Negative voltages correspond to pressure signals. Positive voltages correspond to expansion of the piezoelectric wafer after a pressure pulse or to signal contamination from the plasma potential.

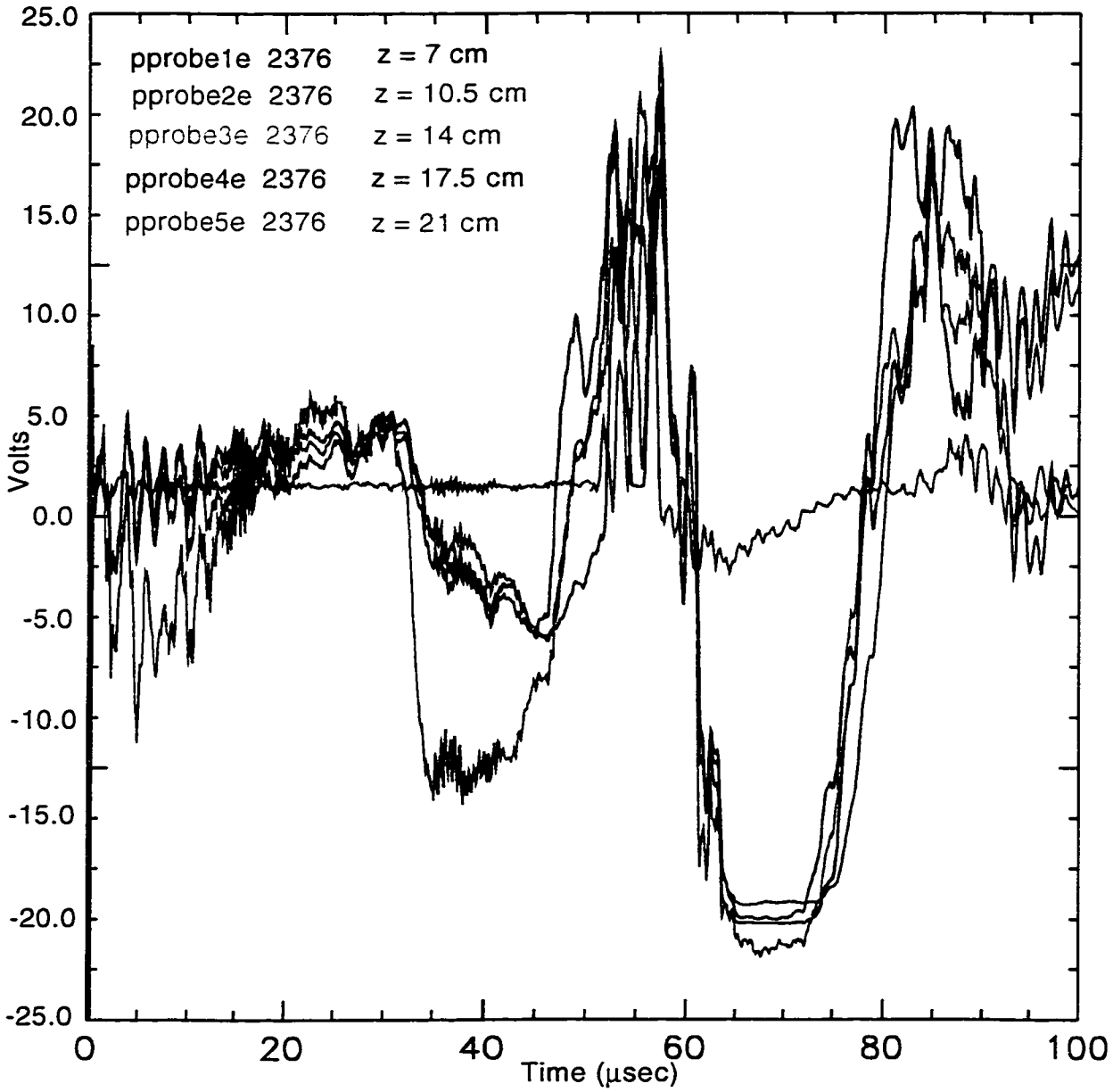

Figure 35. East Piezoelectric pressure probe array results with B_t charged to 2.5 kV pointing East.

The center probe (probe 3e) was the dummy probe that measured only the plasma potential. Signal contamination from the plasma potential on the order of 15 volts was briefly seen immediately prior to the larger of two peaks seen on the live probes, but then quieted down to less than 3 volts. The live probes saw two distinct negative peaks which correspond to pressure pulses. The first smaller signal at approximately 33 μsec is the impact from the scrape off layer plasma, while the main larger signal approximately 30 μsec later is the bulk of the plasma hitting the probes after the FRC has impacted with the back wall of the chamber, reflected, and continued to spread out (deform) in the x direction due to external forces. The penetration and disassembly of the FRC will be examined in a later section.

The signal due to the scrape off layer was not seen on the East array when the transverse field direction was reversed. Figure 36 shows results from plasma shot # 2420 with the interaction magnetic field energized to 2.5 kV and pointing West. No signal was recorded at the time expected for the scrape off layer of the FRC, in fact, no significant signal was recorded at all. In addition to the plasma being deflected off axis due to the field gradient, the FRC frequently was not perfectly vertically centered or drifted vertically off axis in the transverse field chamber. This particular plasma shot was observed by emission arrays to be approximately 5 cm below axis when it reached the center of the transverse field chamber. While this would account for the lack of the larger secondary signal, it should not preclude the signal from the scrape off layer. Plasma from the scrape off layer should flow along the open field lines ahead of the FRC and impact the probe array regardless of the position of the FRC relative to the axis of the guide field or accelerator sections. The vertical displacement of the FRC off axis increased as the transverse field was energized to higher magnitudes. At the 7.5 kV and 10 kV charge values for the transverse field, the FRC plasma consistently missed the pressure probes. This was not desirable, but

understandable, since the probes viewed the plasma in only a 1 cm high by 15 cm wide region.

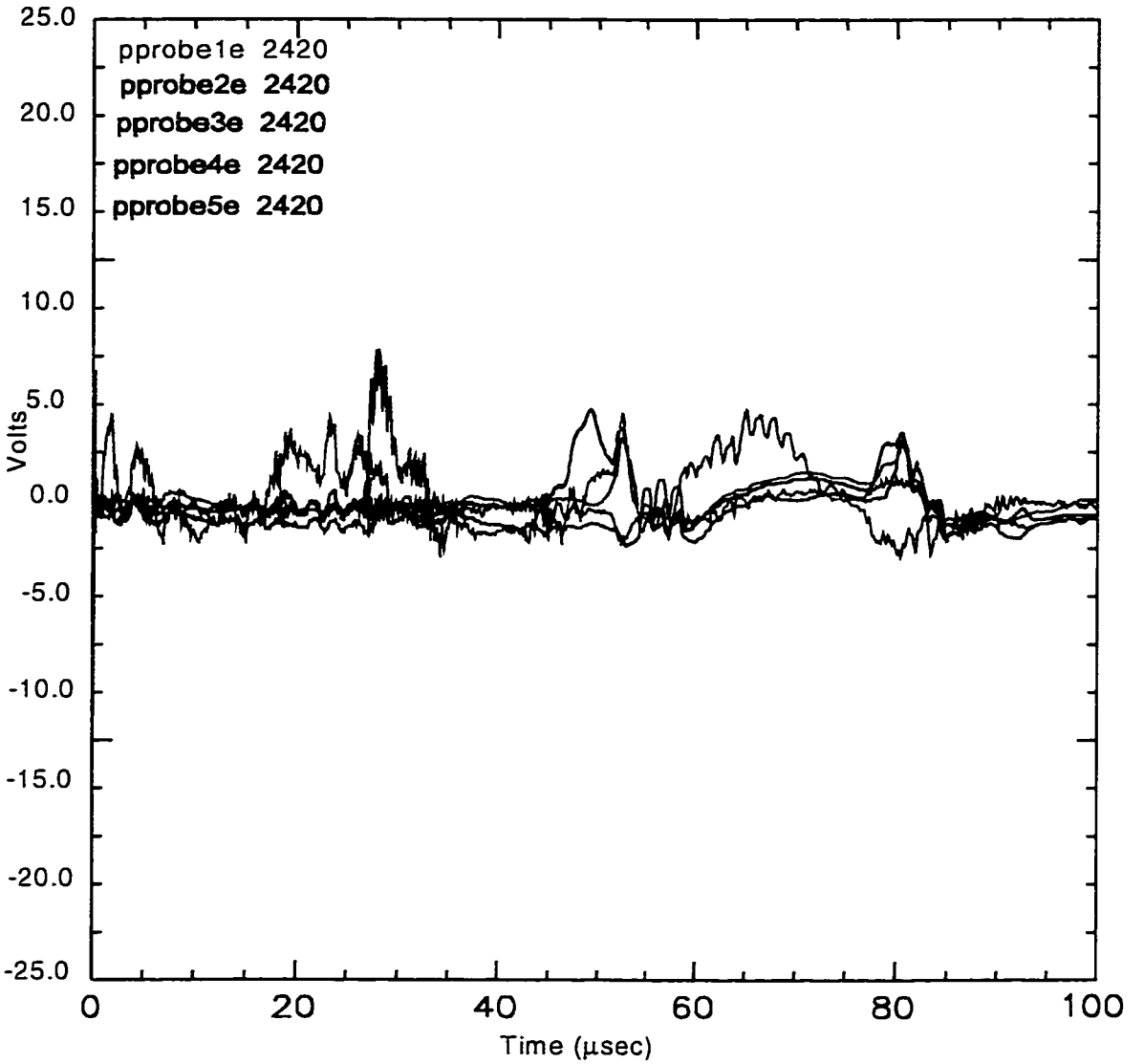

Figure 36. East Piezoelectric pressure probe array results with B_t changed to pointing West

The deflection of the FRC was also qualitatively observed by the array of internal B probes. The probes measure field changes in the z direction, which are strongly dependant on the vertical position of the FRC since B_z varies rapidly in direction with r(y) even for a quiescent FRC. Thus B_z signals can only be interpreted as signaling the presence of the FRC.

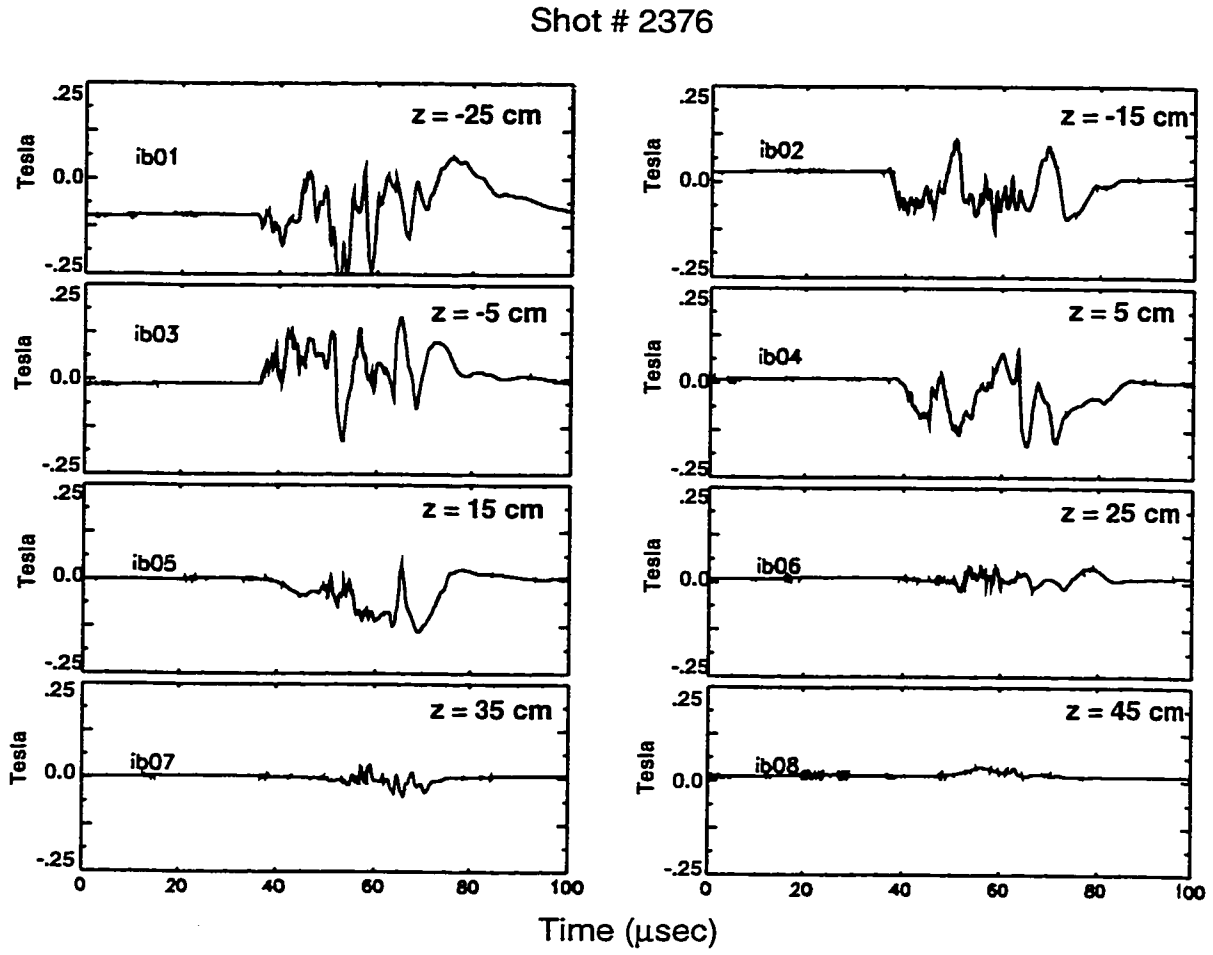

Figure 37. Internal magnetic probe array results with B_t energized to 2.5 kV. B_t = 0.145 Tesla at x = y = z = 0.

The first probe ib01 was located approx. 25 cm forward of the center of the chamber with the other probes spaced behind in 10 cm increments to ~ 45 cm (the Back wall) for ib08. The structure of the signals was hard to decipher reflecting the internal turbulence of the FRC, however, the presence and magnitude of the signal was distinctive and noticeable. The array showed signals on all probes except possibly ib08, although the signal magnitudes decreased the further back the plasma reached. Near the back wall, where the probe would be measuring the B_z component of the FRC internal field at the front of the FRC, the signal should be small due to the internal field structure of the

FRC. At the ends of an FRC, the internal field is sharply curved as the outer field lines curve around to connect with the inner reversed field lines (see figure 1.), and the internal field is primarily in the radial direction.

The signals indicate that the FRC penetrated into the chamber with only minor deflection caused by the transverse field. Shot #2376 was energized to a low transverse magnetic field and only minimal deflection was expected. Other shots, when the interaction field was energized to a higher magnitude, showed no signals on the back probes indicating less penetration and more severe deflection. Data from shots where the interaction is fully energized to 10 KV (~9 Kg field) showed signals only on the first few probes indicating extreme deflection.

Further support from tomography and thermocouple probes that analyze the FRC position provided some quantitative analysis of the FRC deflection. Two emission arrays were positioned to view the FRC both up/down ($\int \varepsilon (y_i, z=0) dx$), and side to side ($\int \varepsilon (x_i, z=0) dy$) at the center of the transverse field chamber. The data from these two arrays was least squares curve fit to match the emissions calculated for a uniform density, elliptical cross section FRC of arbitrary minor radius, ellipsivity, and center. Results of this tomographic imaging of the emission array data are shown in figure 38 for various transverse field strengths and show the deflection of the FRC. The data shown examined the plasma at the center of the transverse field chamber approximately 2-3 μsec after the front of the FRC had reached the center of the chamber. The tomographic imaging record that the FRC has shifted left (- X direction) ~ 4 to 8 cm, reflecting the effect of the field gradient in the transverse direction in the throat region. Deflection of the FRC at the highest field magnitude was less than expected by the trend and will be explained at the end of this section.

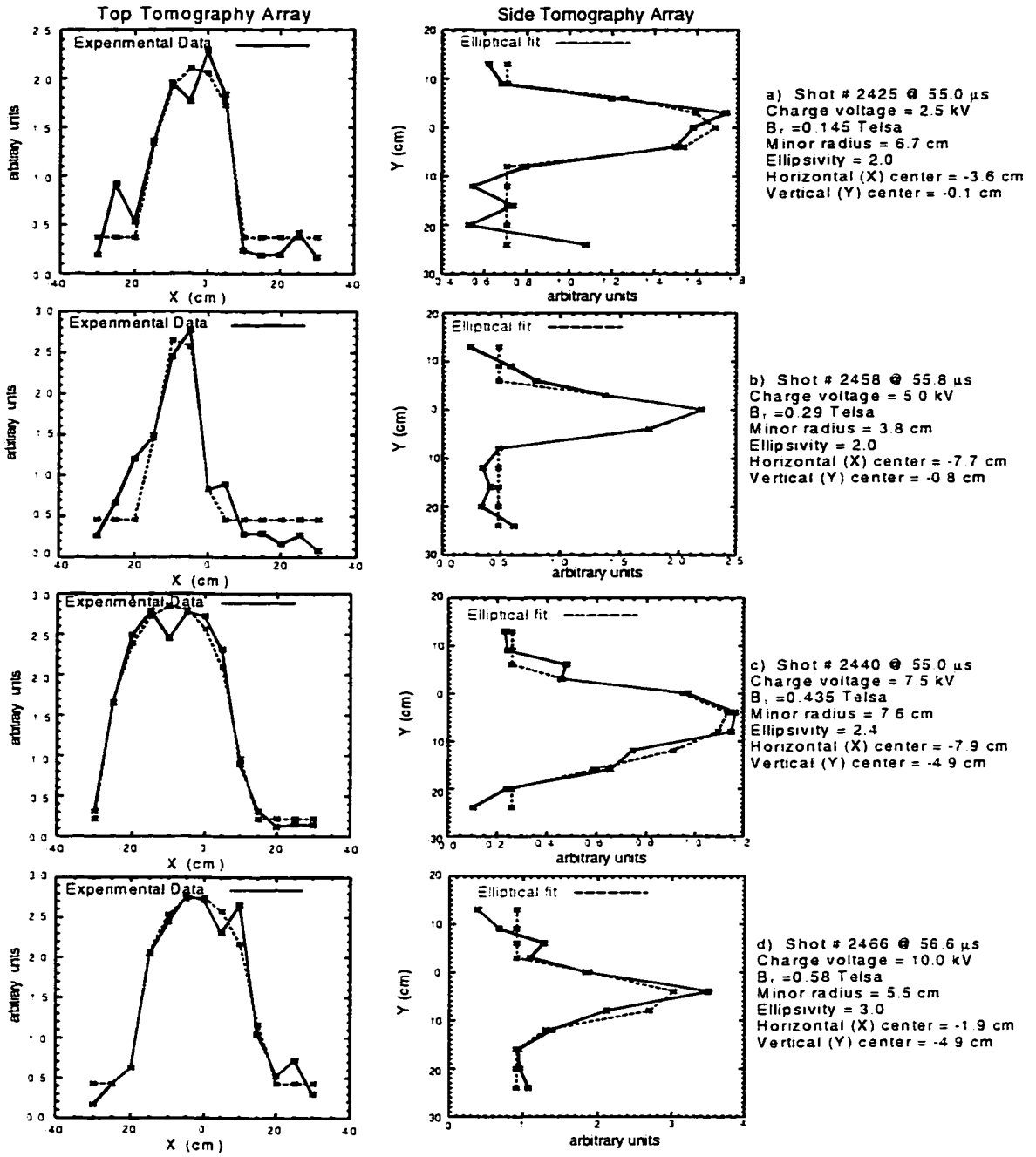

Figure 38. Tomographic imaging of plasma during initial penetration.

Thermocouple results for various transverse field strengths are shown in figures 39 and 40. In figure 39 the thermocouple probes were positioned in the throat entrance region of the transverse field chamber at ~ -33 cm from the center, while those in figure 40 were positioned at the center of the transverse field chamber. The thermocouple signals were curve fit to a gaussian where possible, and the center of the peak and the e-folding distance σ of the major and minor elliptical radii were recorded.

The deflection of the FRC in the x direction (parallel to the transverse field) is difficult to precisely determine since the diagnostic is not time resolved. Clearly, there was some central heating of the quartz tube, and this was where the gaussian fit was attempted. The heating of the wings of the tube right up to the wall of the chamber represent heating due to secondary plasma flow along the transverse field. The right side (+ x) of the signal is the same side of the chamber (East) where the pressure probe signals were recorded due to both the scrape off layer plasma and the FRC plasma reflection off the bask wall.

At the first set of cross-hairs at z = -33cm in the transverse field chamber the horizontal (x direction) thermocouples record that the FRC has shifted left (- x direction) ~ 2 to 3 cm. Again, deflection of the FRC at the highest field magnitude was less than expected. At the second set of cross-hairs at z=0 the thermocouples were not as successful in determining the deflection of the FRC. Shot # 2434 with the field energized to 5 kV showed that the plasma came through the center of the transverse field chamber extremely high. The FRC probably missed the horizontal thermocouple probe on the first pass, and the signal recorded is most likely due to secondary plasma reflecting off the back of the chamber. Shot # 2438 with the field energized to 10 kV completely missed both thermocouple probes as it went off high and left. The results from the other shots where the plasma was fairly well vertically centered show that the FRC was deflected up to 8 cm to the left when the transverse field was energized to 7.5 kV.

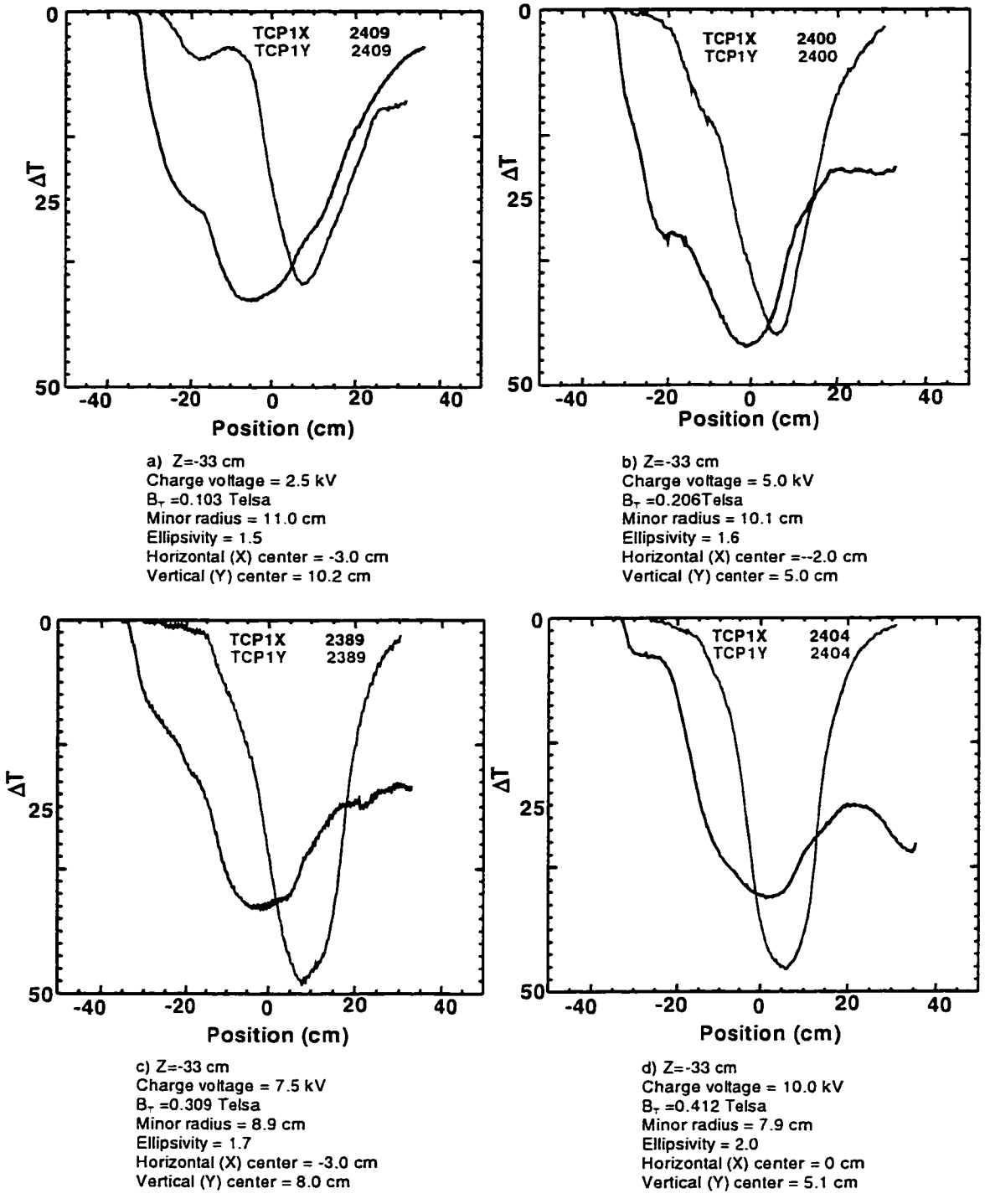

Figure 39. Theromcouple results at entrance to the transverse field chamber. (z=-33cm)

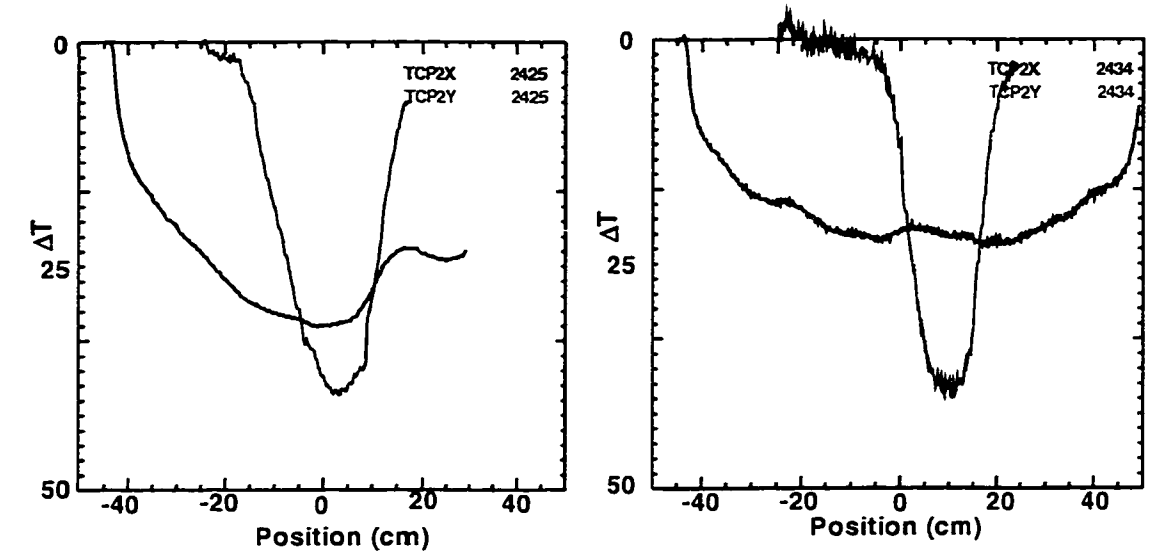

a) Z=0 cm
Charge voltage = 2.5 kV
B_T =0.145 Telsa
Minor radius = 13.0 cm
Ellipsivity = 2.3
Horizontal (X) center = -2.0 cm
Vertical (Y) center = 2.0 cm

b) Z=0 cm
Charge voltage = 5.0 kV
B_T =0.29 Telsa
Minor radius = 9.0 cm
Ellipsivity = 4.5
Horizontal (X) center =+2.0 cm
Vertical (Y) center = 10.0 cm

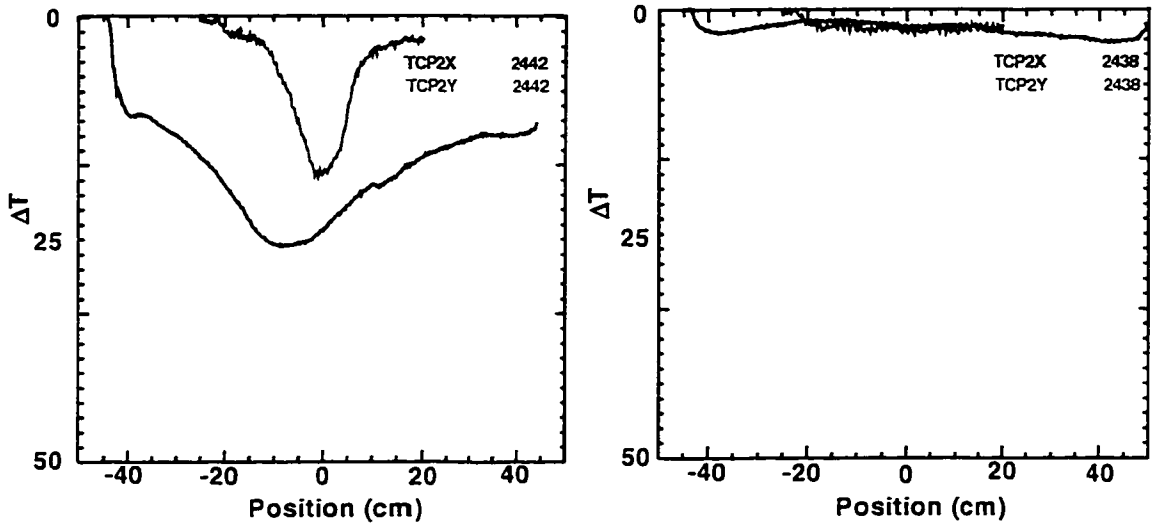

c) Z=0 cm
Charge voltage = 7.5 kV
B_T =0.435 Telsa
Minor radius = 8.0 cm
Ellipsivity = 3.0
Horizontal (X) center = -8.0 cm
Vertical (Y) center = 0.0 cm

d) Z=0 cm
Charge voltage = 10.0 kV
B_T =0.58 Telsa
Minor radius = Unknown
Ellipsivity = Unknown
Horizontal (X) center = Unknown
Vertical (Y) center = Unknown

Figure 40. Theromcouple results at center of transverse field chamber. (z=0 cm)

The results from the numeric calculation of the sideways force were used to estimate the deflection of the FRC as it penetrated into the transverse field. The off-axis deflection data from the tomographic imaging for several experimental shots as well as the predicted off-axis deflection is shown below in figure 41.

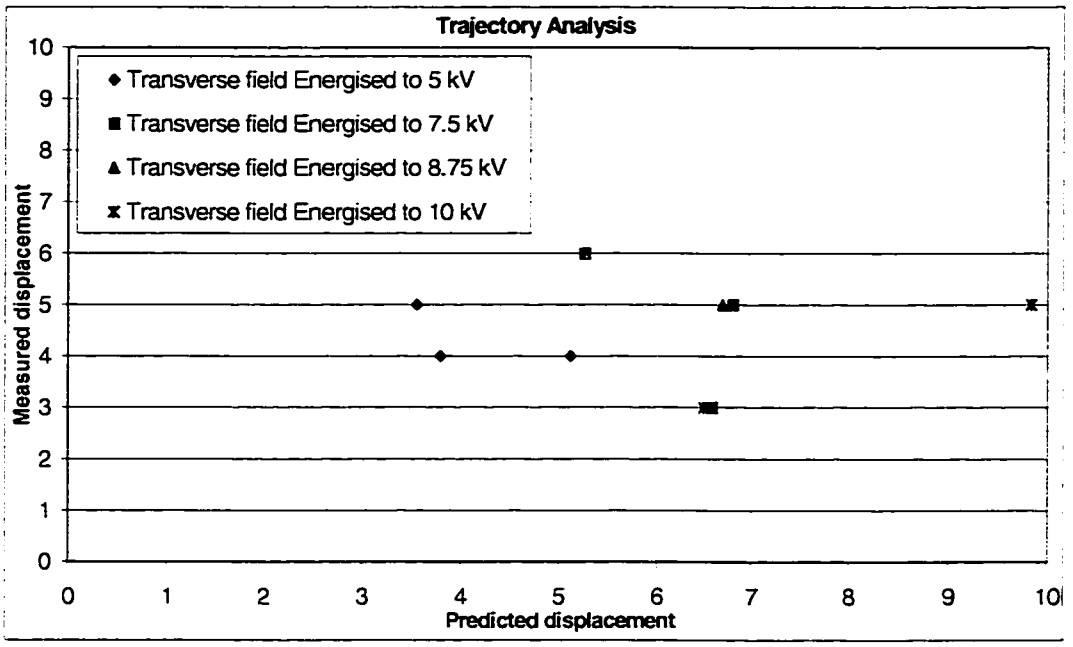

Figure 41. Horizontal deflection analysis of penetrating FRC

The measured deflection matched fairly well with that calculated from the simple analysis for the low and moderate fields. At higher fields, the measured deflection was less than predicted, with the difference between experimental and analytical results increasing as the transverse field increased. This was due to the FRC hitting the stainless steel tube wall at the throat of the transverse field chamber as seen in the imacon pictures taken from the source end of the

experiment. As the FRC was pushed or deflected sideways into the tube wall, screening currents formed in the wall to push it away, which altered the trajectory and decreased the sideways deflection seen in the experiment.

7.2 FRC deformation

The deformation of the FRC again was first observed by the imaging cameras and then later quantified by other diagnostics. Several frames (t = 50,55,60 μsec) of the Imacon picture shown in figure 20 show the FRC as it impacted the quartz tube cross-hairs. The light-up on the horizontal (x) tube was clearly longer than the light-up on the vertical (y) tube indicating that the FRC had deformed out of a circular cross-section and flattened into a more elliptical cross section. This deformation was consistently observed in all plasma shots when the transverse field was energized to any level and was not observed when no transverse field was present.

The deformation of the FRC from the thermocouples was difficult to precisely determine, since the diagnostic is not time resolved and may have been subject to plasma reflection from the back wall. However, from the thermocouples it was observed that the FRC was well confined in the Y direction perpendicular to the transverse magnetic field as would be expected. The higher the field into which the FRC penetrated, the smaller the FRC cross section became in this dimension. The thermocouple probes (shown in figure 39) positioned to intercept the plasma in the throat entrance region (z=-33 cm) of the transverse field chamber show the initial deformation of the FRC during injection. The gaussian fits of the thermocouple data for the horizontal (x) probes were only approximate, so the estimated value of ellipsivity was only approximate. Still, the FRC was seen to rapidly deform to an ellipsivity of approximately 1.5 to 2.0 by this point. The thermocouple probes (shown in figure 40) positioned to intercept the plasma at the center of the transverse field chamber evaluated the

plasma deformation approximately 2 μsec later and showed greater deformation as expected. The FRC deformed to an ellipsivity of ~2.3 for the lowest field case and an ellipsivity of ~3 when the transverse field was energized to 7.5 kV. Again, the data from shot # 2434 with the field energized to 5 kV was extremely questionable and shot # 2438 with the field energized to 10 kV completely missed both thermocouple probes.

The results of the tomographic imaging of the emission array data (shown in figure 38 for various transverse field strengths) provided good information on the deformation of the FRC at the interaction chamber center. The tomographic fitting of the emission array data calculated that the FRC had deformed to an ellipsivity of ~2 to 3, with the FRC deformation from circular to elliptical cross-section increasing with higher transverse field magnitudes. The Lagrangian calculation (figure 4) of deformation and equations [3.12 b,c] predicted that the FRC would have ample time to deform to an expected ellipsivity of approx. 3 to 4.

7.3 FRC penetration and disassembly

Except for when the plasma deflection in the x direction was extreme, the penetration of the FRC in the transverse field was best observed by a visible light emission array (similar to the tomography) positioned along the axial direction ($\int \varepsilon (z_i, x=0) dy$) to monitor the FRC in the transverse field. Data from this array is shown in figure 42 for weak and strong transverse fields with results being extremely sensitive to the transverse field magnitude. For virtually all of the experimental operating conditions, the FRC penetrated into the center of the transverse field chamber approximately 50 μs – 55 μs after the experiment was fired. For the low transverse fields, it was seen that the FRC reflects off the back wall of the stainless steel vacuum chamber. This axial emission array data in figure 42a. shows the plasma emission peaking initially at the array position

furthest axially from the entrance (closest to the back wall) of the transverse field chamber, with the emission peaks progressing forward in time. The density pile up occurred because the magnetic flux inside the FRC could not penetrate the conducting wall boundary, and the FRC was reflected. The reflection was elastic enough to send the FRC mass back toward the entrance.

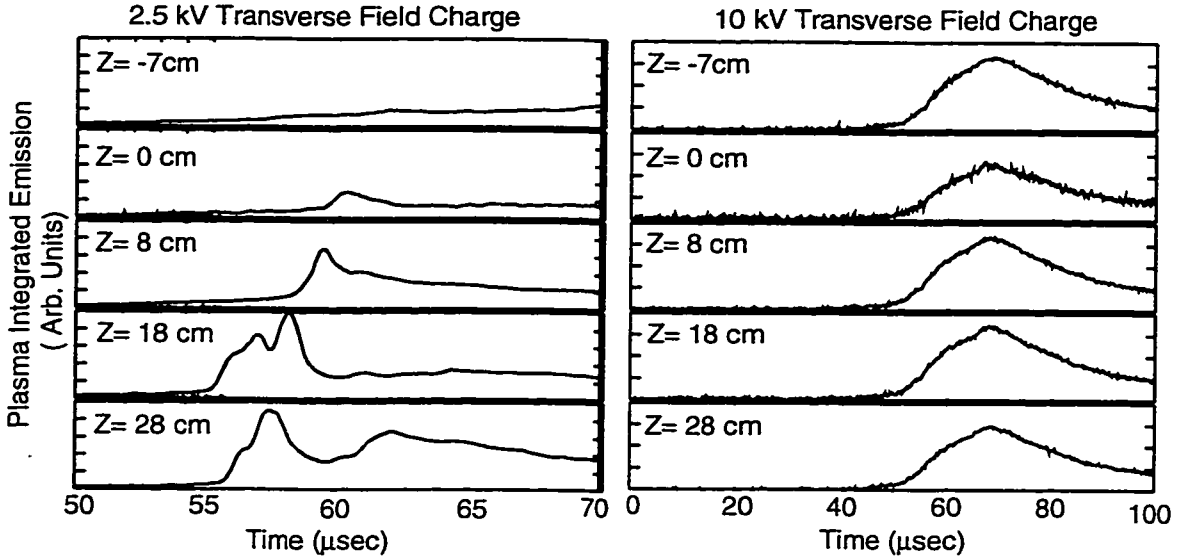

Figure 42. Integrated plasma emission in y at various axial positions (X=0).

At the highest transverse fields, there was enough compression and slowing down of the FRC by the transverse field that the reflected density wave did not occur. The emission data for the maximum transverse field produced at 10 kV in figure 42b indicates that the FRC arrived at the back half of the interaction chamber at a higher density initially (at ~ 55μsec) than that of the lower transverse field shots. The FRC rapidly piled up at the back and in the middle of the chamber as indicated by nearly simultaneous signals on all emission channels. The signals at all axial stations are of comparable magnitude and indicate that the FRC completely penetrated to the back of the transverse field chamber.

The emission signals peaked at approximately 67 μsec and decayed away in ~ 40 – 50 μsec, indicating that the plasma remained coherent and dense

enough to register a signal on the emission array for that length of time. The timing of the peak signal is consistent with the Imacon pictures of the plasma taken from above shown in figure 29. The last frame at t=63 μsec shows plasma light-up everywhere indicating that the enough of the plasma had reflected and spread to the point where it was making wall contact throughout the chamber. This helps to explain the signals seen by the pressure probes in figure 35. The second pressure pulse which is attributed to impact from the FRC plasma as opposed to the scrape off layer plasma, started at about 60 μsec and persisted for approximately 15 μsec. It is during this period after the reflection off the back wall that the FRC is presumed to be expanding, disassembling, and impacting the sides of the transverse field chamber, causing the pressure pulses and light-up seen in the Imacon pictures. This spreading and disassembly also accounts for the heating of the wings of the horizontal (x axis) quartz tubes (used to house the thermocouples) right up to the wall of the chamber as seen in figures 39 and 40.

7.4 FRC flux exclusion

The external magnetic probes recorded the perturbations of the transverse field caused by the penetrating plasma, and were used to examine the flux excluding nature of the FRC. The transverse field was aligned in the x direction so, due to the positioning of the probe, only the loops recording ΔB_x recorded any significant signals. The results of the magnetic probe array are shown in figure 43 for the various transverse field charge voltages used during TRAP.

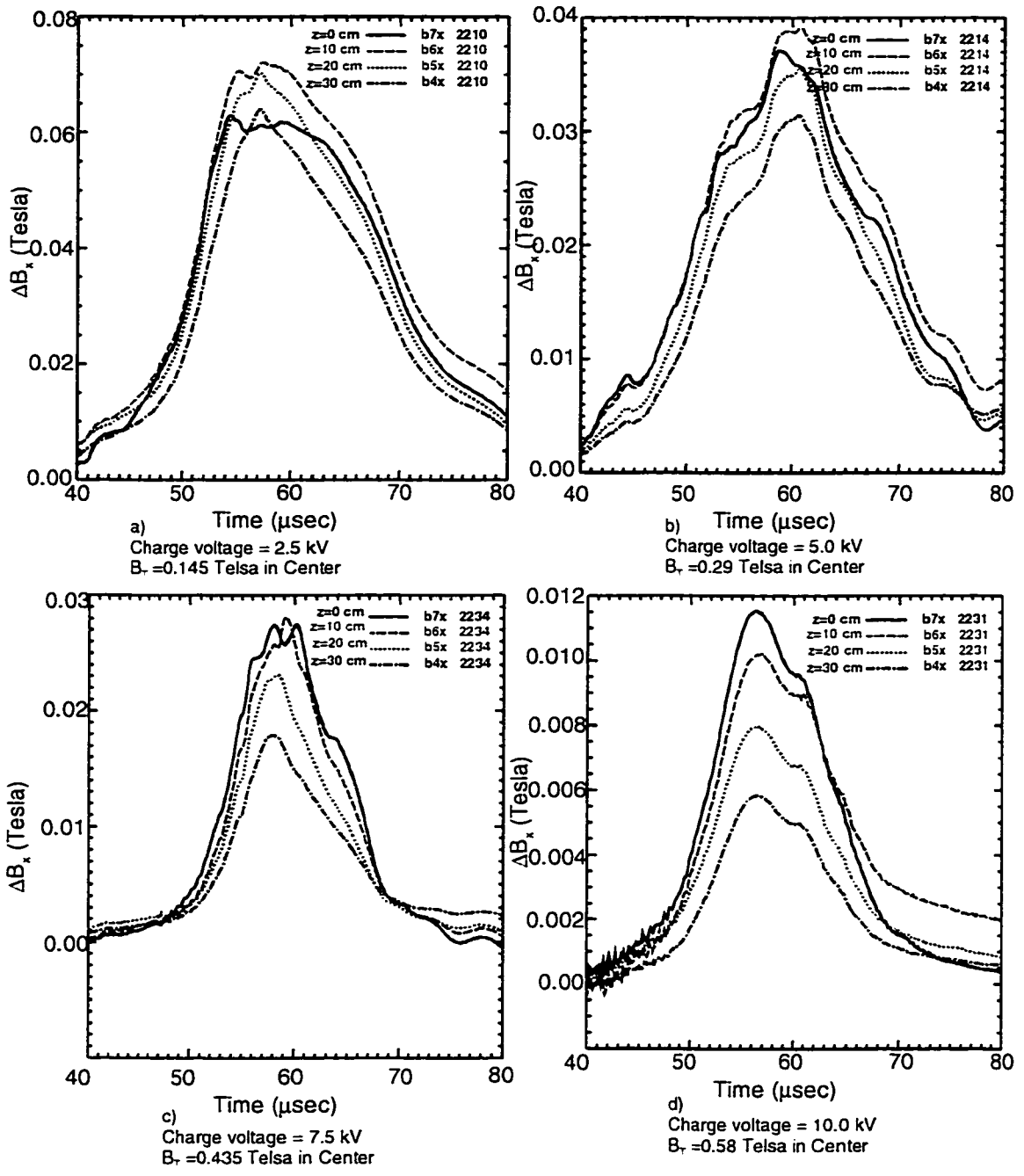

Figure 43. ΔB signals from external probes measuring flux exclusion by the penetrating FRC

The magnitude of the ΔB_x signal from the B probes was extremely sensitive to the minor radius of the FRC, much more so than to the magnitude of the transverse field. When the FRC penetrated into higher fields, the minor radius decreased and produced a smaller field perturbation at the probe location even though the magnitude of the transverse field was higher.

The external B probe signals began approximately simultaneously at the different probe locations. This was not unexpected due to the fact that the external B probes span a range of only 30 cm, and the FRC, when injected into a low transverse field, is accelerated to speeds on the order of 25 cm/μsec, allowing it to cover the 30 cm distance in little more than 1 μsec. Even at the more moderate transverse fields, the FRC would still traverse the probe distance in 1.5 to 2 μsec. When the FRC was injected into the highest transverse fields, it was observed to rapidly pile up as seen by the emission array results of figure 42b, which also accounts for the near simultaneous signals seen by the B probes.

The external B probe signals peak at 56-60 μsec, several μsec after the time at which the tomographically imaged data was analyzed. This time was 4-5 μsec after the plasma has passed the midpoint of the transverse field chamber and corresponded approximately to either when the reflected density wave (seen in figure 42a at low fields) passed by the probes on the return bounce, or when the FRC piled up at high fields (seen in figure 42b) and then horizontally spread out as seen by the Imacon pictures in figure 29 and the pressure probes in figure 35.

The minor radius of the FRC was inferred from the peak ΔB_x signals by comparisons to the numeric simulations of a flux excluding elliptical FRC in a transverse magnetic field bounded by a flux conserving channel. The location of the center of the FRC and the ellipsivity of the plasma at the varying transverse field strengths was estimated based upon results from other diagnostics. The

values of ellipsivity ranged from e ~ 1.5 at B=0.15 Tesla to e~3.5 at B=0.44 Tesla.

The predicted area ratios are very sensitive to the axial contraction model used to evaluate the FRC transition into the transverse field chamber. A simple model assuming zero axial compression would underestimate the expected area ratio. The axial compression model outlined in section 3.6 (equation [3.35]) equates the change in cross sectional are of the FRC in the transverse field chamber to what it would be if it penetrated into a larger flux conserving axial field chamber with the same equivalent magnetic pressure. Although this is a gross approximation, as seen by the MOQUI calculation of figure 10, it is still the best available simple model for comparison with the measured area ratios. We will assume a value of A_{tube2}/A_{tube1} = 7.6 and ε = 0.25 in equation [3.35] to calculate the expected area in the interaction chamber at a given ratio of B_g/B_t.

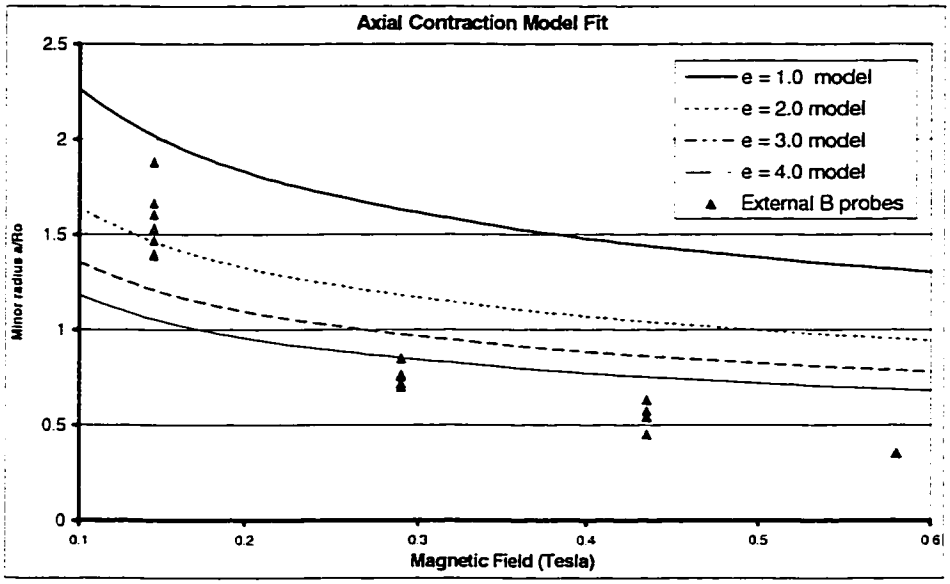

Figure 44. Examination of Flux excluding nature of FRC. B probes located at z=0 showing peak signal recorded at ~ 56-60 μs.

The minor radius of the FRC as inferred by the signals from the external B probes was compared to that predicted by the axial contraction model (equation

[3.35]) for a range of elliptical cross-sections. Within the expected experimental uncertainty due to the trajectory of the FRC and the crudeness of the model, the B probe data supports the assumption about the flux excluding nature of the FRC in the transverse field and the validity of the transverse field perturbation model.

7.5 Area Measurements

The model for an FRC penetrating into a transverse field in a flux-conserving channel focused on the change in cross-sectional area of the FRC. The expected change in area ratio of the FRC was numerically determined (equation [3.35]), as a function of B_T for several values of ellipsivity. The quantitative information from several diagnostics was then compared to the numerical model. The results are shown below in figures 45 and 46. The lines represent the numerical solutions to the axial contraction penetration model for the ellipsivity ranging from 1 to 3.

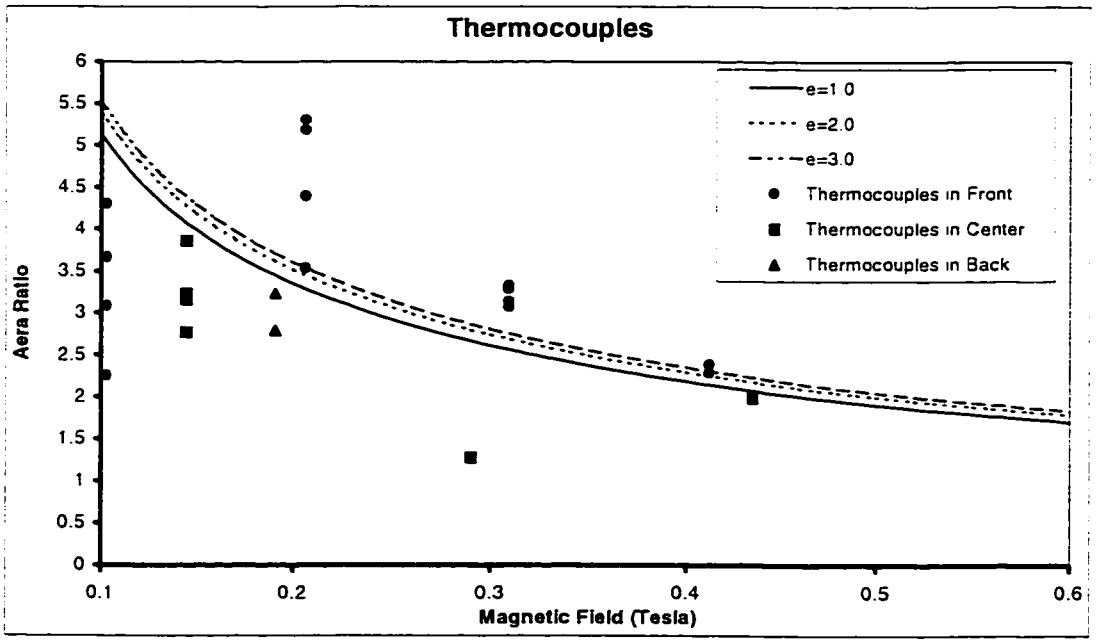

Figure 45. Thermocouple data fit to numerical predictions

At low fields (B_T<0.2 Tesla) the thermocouple data of the penetrating FRC does not match well with the isentropic model predictions. There are several explanations for the differences, primarily the crudity of the model. The model for the change in FRC cross-sectional area is based on the assumption that the expansion/compression of the FRC injected into the transverse field is similar to the expansion/compression of an FRC injected into an axial field with an assumed size flux conserver and that the FRC will reach some new state of equilibrium. Clearly, this is highly approximate as the severe bending of the transverse field as it is excluded from the FRC may affect the compression of the FRC in unpredictable ways, and the FRC shape is largely governed by dynamic effects, as calculated by MOQUI and shown in figure 10. Secondly, at low fields the FRC was further accelerated into the transverse field chamber as it essentially expanded into a near vacuum, and did not have enough time to expand to the predicted cross-sectional area before encountering the thermocouple probes.

At moderate fields (B_T>0.2 Tesla) the collected thermocouple data matches reasonably well and follows the trends of the model curves. The FRC deforms to an ellipsivity of ~ 2-3 as the FRC expands into the transverse field chamber. At even higher transverse fields, the FRC severely deformed to an ellipsivity of >3, as the FRC expanded into the transverse field chamber.

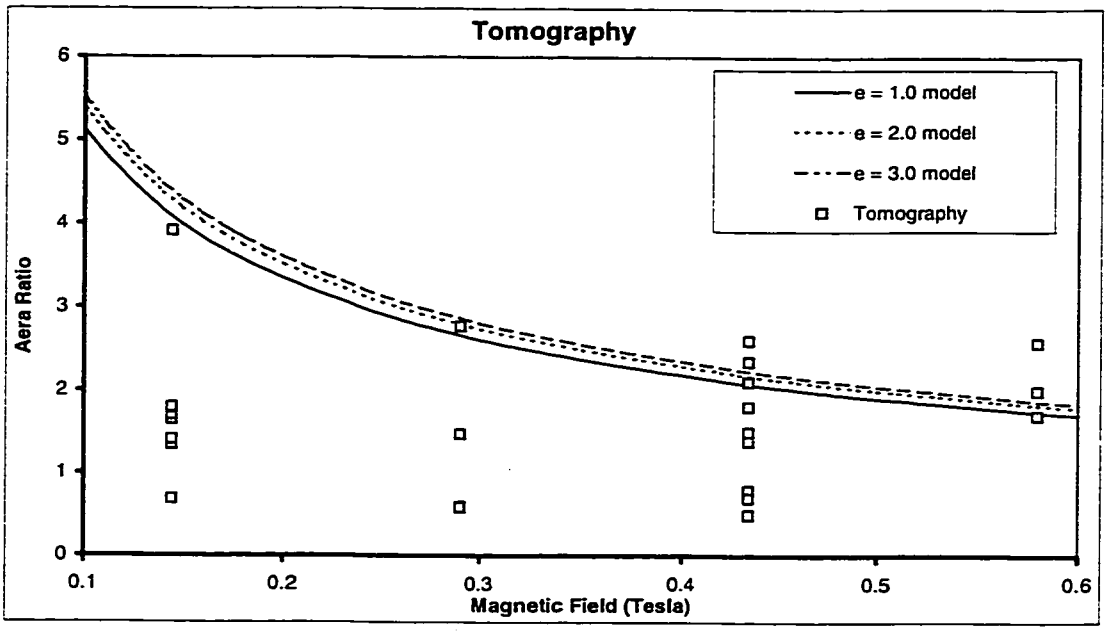

Figure 46. Tomographic data fit to numerical predictions

The tomographic data was extremely scattered and did not match well with the model predictions (or even the thermocouple data) except at the highest experimental fields. This was probably due to the poor spatial resolution of the diagnostic resulting in errors in the tomographic fitting. Emission array signals after the FRC reflection off the back wall of the chamber rapidly went off-scale for the digitizers. This was due to massive plasma contact with the walls and quartz cross hairs resulting in excessive light-up. Tomographic imaging of the emission array data after the reflection, therefore, was not possible .

Chapter 8

Summary, Conclusions, and Suggestions for future work

The feasibility of using an accelerated FRC's as a deep penetration refueling system for a large scale Tokamak Reactor has been investigated. A model has been presented that explains the experimental measurements from the TRAP Experiment at the University of Washington. The FRC is seen to exclude the flux of the transverse field during injection. The interaction of the axial field of the transport section and the transverse field cause field gradients in the throat region of the transverse field chamber. These field gradients cause an observed trajectory that initiates the tilting of the FRC, and pushes the FRC off the injector axis. While traversing the transverse field the FRC is observed to deform from a circular to elliptical cross-section on the time-scale of a few μsec. The FRC compresses as it penetrates into a region of higher field. Results from isentropic penetration models predict better penetration than the conventional $\frac{1}{2}mn_1u_1^2 = \frac{B_t^2}{2\mu_o}$ assumption for an elliptically deformed FRC due to the plasma compression. However, this relationship is inappropriate as it ignores the significance of the internal enthalpy of the FRC. Injection efficiencies were thus evaluated using the scaling relationship. $\frac{1}{2}mn_1u_1^2+\frac{5}{2}p_1 = \mathrm{K}\frac{B_t^2}{2\mu_o}$.

It was found that K could be significantly reduced to less than 5/2 for large ratios of B_t/B_e if the compression of the FRC during penetration was isentropic. However, dynamic code (MOQUI) calculations showed that this isentropic penetration model was inappropriate, and that K values were not reduced as much as predicted. Since the experiment never had transverse fields that were strong enough to stop the FRC's, we could not present an experimental

determination of K, and the code calculations should be used as a conservative worst case model.

For refueling purposes, it is best to have as high value of $M_1^2 = \frac{\rho_1 u_1^2}{p_1}$ as possible to take advantage of the lowering of K due to compression. Detailed 3-D calculations should be preformed to calculate K more accurately than our 2-D code allowed. It is, of course, also beneficial to operate at as high a density as possible to minimize the energy per unit ion required for injection. The maximum density will be determined by the method of formation of the FRC.

Further investigations should be conducted with an FRC injector on a working Tokamak test reactor to further investigate the penetration of FRCs at extremely high velocity into high fields, and to quantify and optimize the operational parameters of an FRC injector.

References

1. L.J. Perkins, S.K. Ho, J. H. Hammer, Nucl. Fusion **28**, 1365 (1988).
2. J. H. Hammer and C.W. Hartman, Mirror Theory Monthly, LLNL, Livermore, CA (1981).
3. J.H. Hammer et al, Phys. Rev. Lett. **61**, 2843 (1988).
4. M.R. Brown and P.M. Bellan, Phys. Rev. Lett. **64**, 2144 (1990).
5. D.J. Rej, et al, Phys. Fluids **29**, 852 (1986).
6. M. Tanjyo, et al, in Plasma Physics and CNFR 1984 (Proceedings 10^{th} Int. Conf. London, 1984), Vol. 2, IAEA, Vienna 523 (1985).
7. A.L. Hoffman, et al, Fusion Technology **9**, 48 (1986).
8. P.B. Parks, Phys. Rev. Lett. **61**, 1364 (1988).
9. A.M. Kuethe and J.D. Schetzer, Foundations of Aerodynamics, 2^{nd} ed., 63.
10. M. Tuszewski, Nucl. Fusion **28**, 2033 (1988).
11. J.A. Grossnickle, Masters Thesis, U. of Washington (1997).
12. G.C. Spanjers, Masters Thesis, U. of Washington (1990).
13. R. Raman, et al, Fusion Technology **24**, 239 (1993).
14. J.C. Thomas, Doctoral Dissertation, U. of California, Davis, (1994).
15. P.K. Loewenhardt, et al, Rev. Sci. Instrum. **66**,1050 (1995)
16. P. Gierszewski, R. Raman, D. Hwang, Fusion Technology **28**, 619 (1995)
17. C.W. Hartman and J.H. Hammer, Phys. Rev. Lett. **48**, 929 (1982).

18. L.C. Steinhauer, Phys. Fluids **26**, 254 (1983).

19. M.R. Brown and P.M. Bellan, Phys. Fluids B. **2**, 1306 (1990).

20. M.R. Brown and P.M. Bellan, Nucl. Fusion **32**, 1125 (1992).

21. R. Raman, et al, Phys. Rev. Lett. **73**, 3101 (1994).

22. M. Tuszewski and B.L. Wright, Phys. Rev. Lett. **63**, 2236 (1989).

23. K.E. Miller, Drawing contribution

24. J.A. Grossnickle, Drawing contribution

25. A.L. Hoffman, Private communication

26. J.T.Slough, Private communication

27. L.C. Steinhauer, Private communication

VITA

Peter Gurevich was born October 29, 1968 in Wiesbaden, Germany to Albert and Susan Gurevich. He graduated from the Mercer Island High School on Mercer Island, Washington, in 1986. He attended the University of Washington where he received his Bachelors of Science degree in Aeronautics and Astronautics in 1990 and his Masters of Science degree in Aeronautics and Astronautics in 1992.

IMAGE EVALUATION
TEST TARGET (QA-3)

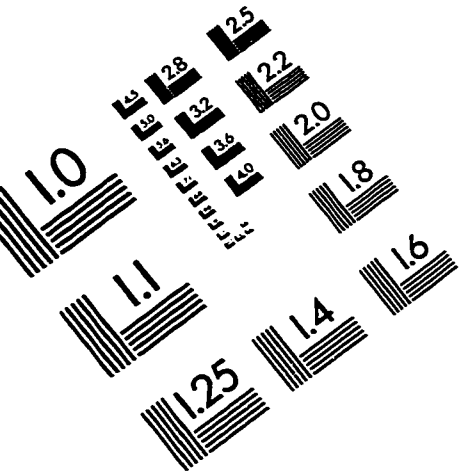

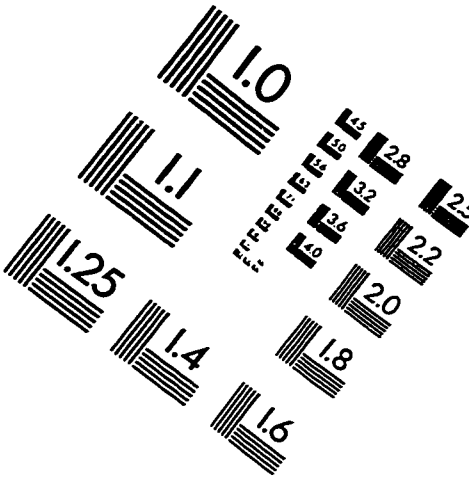

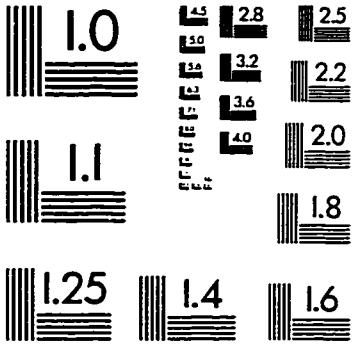

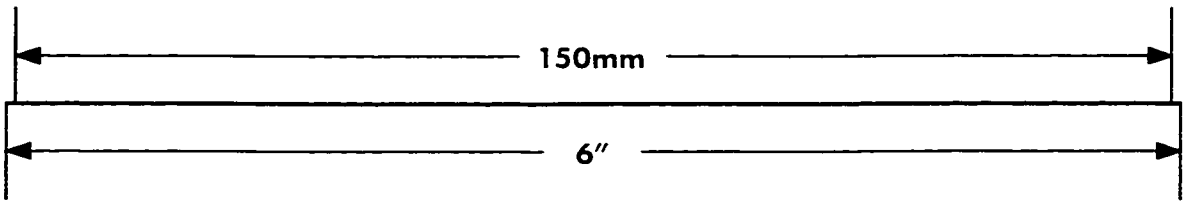

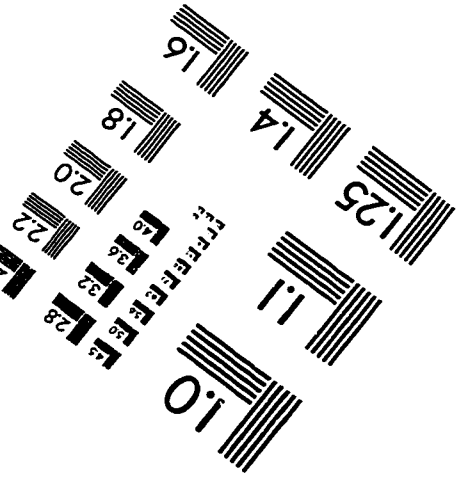

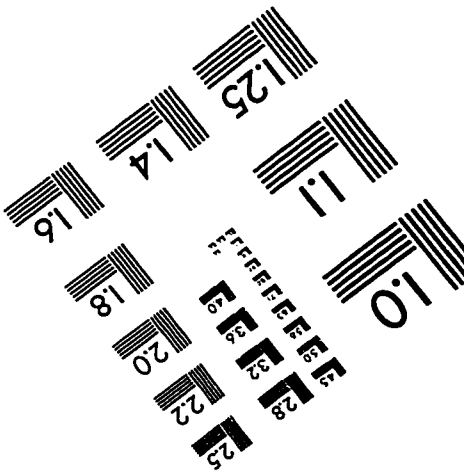

APPLIED IMAGE, Inc
1653 East Main Street
Rochester, NY 14609 USA
Phone: 716/482-0300
Fax: 716/288-5989